Setup of a Molecular Beam Apparatus to study the reactivity of single crystal surfaces and its application to CO oxidation on Au(332)

Inaugural – Dissertation

To obtain the academic degree

Doctor rerum naturalium

(Dr. rer. nat.)

Submitted to the Department of Biology, Chemistry and Pharmacy

of Freie Universität Berlin

by

Raphaell Moreira

Minas Gerais, Brazil.

Berlin, 2017

1st Reviewer: Prof. Dr. Thomas Risse

2nd Reviewer: Prof. Dr. Marcus Bäumer

Date of defense: 26.01.2018

“Try to make sense of what you see and wonder about what makes the universe exist. Be curious, and however difficult life may seem, there is always something you can do, and succeed at. It matters that you don’t just give up.”

Stephen Hawking

Acknowledgment

First, I want to thank my advisor, Professor Thomas Risse, who has been an immense support and guide in all matters toward becoming an independent scientist. His depth of knowledge and insight has been an invaluable resource. It has been a privilege to work with him and with the AG Risse as a whole.

Thank you to my second advisor Professor Marcus Bäumer for your support, feedback, and for taking the time to read this thesis and evaluate my defense.

I would like to thank the AG Risse, particularly those with whom I collaborated – Dr. Eric Mayer, Dr. Peter Clawin, Mr. Rudolph Cames and Dr. Wiebke Riedel. Another special thank also goes to the Machine and Electronic workshops.

I could not have made this journey without the support of my family and friends. Thanks to my siblings: Paulo, Marilia, Mirian, and Carlos, for their support and encouragement. Thanks to the non-chemist Berliner friends, especially to Jan, what to say – Thank you so much! Another special thank goes to Sr. Paulo for sending always positive vibration during this battle.

I also gratefully acknowledge the financial support from the *Deutscher Akademischer Austauschdients* and CNPq Fellowship Program (DAAD/CNPq) under contract no. 290149/2014-2. It was a fantastic program that significantly enriched my graduate and professional experience.

Finally, I would like to thank and dedicate this Dissertation to my parents: Jose Moreira and Ivanilda Moreira.

Abstract

Nanoporous gold (np-Au) has emerged as a very promising catalyst for a variety of catalytic processes. In recent years' significant efforts have been made to elucidate the role of structural aspects as well as admixtures of a second metal, oftentimes silver, which remains in the nanoporous material produced by corrosion of an appropriate alloy such as AuAg. Investigations on well-defined single crystalline model systems provide evidence that the reactivity of np-Au can be rationalized by the properties of low index Au surfaces. However, various open questions still remain such as the role of steps or the importance of water for the understanding of the catalytic properties. In order to investigate reaction kinetics of catalytic reaction on well-defined single crystal surfaces, an ultra-high vacuum molecular beam chamber was setup. The oxidation reactions were performed under isothermal conditions using pulsed molecular beam techniques combined with mass spectrometric measurements to monitor the kinetics of products in the gas-phase. In addition, the apparatus allows for an IR spectroscopic characterization of the surface under reactions conditions to elucidate the nature of surface species during the reaction. As Au surfaces do not dissociate molecular oxygen under UHV conditions the experiment utilizes an effusive beam of atomic oxygen as created by a thermal cracker. In this thesis CO oxidation was studied on the Au(332) surface. Initially, IRAS studies were performed to obtain a detailed assignment of IR vibration modes of ^{13}CO on the pristine and O pre-covered Au(332) surface. In agreement with the literature results, IRAS studies showed a ^{13}CO band on pristine Au(332) with a maxima at about 2075 cm^{-1} at low coverages, which shifts to lower wavenumber as the coverage rises. The O pre-covered Au(332) surface shows initially two distinguishable vibrational bands which suggest that different adsorption sites were created after exposure the surface to O atoms and additionally the results show that CO is more strongly bound on the oxygen pre-covered surface than on the pristine Au(332). Transient kinetics of CO oxidation reaction on Au(332) provide clear evidence for a much more complex reaction scenario than anticipated by simple oxidation of CO by oxygen atoms. Moreover, the results showed the beneficial effect of water being known to be in fast exchange with adsorbed oxygen, which hence can compete with CO oxidation. The transient kinetic shows clear evidence for fast and slow processes as a function of water pressure. At high water partial pressure, the system adopts steady state kinetics, while it does deactivate at lower pressures due to the formation of Au-O phases being less reactive towards CO oxidation. Due to the quantitative nature of the molecular beam experiments it is possible to show that the system exhibits a significant transient oxygen concentration on the surface while being in steady state.

The latter oxygen does, however, react with CO in case the oxygen atom supply is switched off. The ability of water to utilize oxygen present in Au-O phases for CO oxidation being otherwise not reactive under the chosen experimental conditions can be directly correlated to observation for np-Au. For these systems water was found to be beneficial not only for the steady state reactivity of the system, but perhaps even more interesting for a reactivation of a deactivated catalyst, which can be explained by the utilization of otherwise unreactive oxygen species poisoning the surface.

Zusammenfassung

Nanoporöses Gold (np-Au) hat sich als vielversprechender Katalysator für eine Vielzahl katalytischer Prozesse erwiesen. In den letzten Jahren wurden erhebliche Anstrengungen unternommen, um die Rolle der strukturellen Aspekte sowie von Beimischungen eines zweiten Metalls, oft Silber, aufzuklären. Letzteres verbleibt in den durch Korrosion einer geeigneten Legierung wie AuAg hergestellten Systemen. Untersuchungen an wohl-definierten einkristallinen Modellsystemen haben gezeigt, dass die Reaktivität von np-Au qualitativ durch die chemischen Eigenschaften von Au-Oberflächen mit niedrigem Index erklärt werden kann. Verschiedene Fragen wie die Rolle von Stufen oder die Bedeutung von Wasser für das Verständnis der katalytischen Eigenschaften bleiben jedoch offen. Um die Reaktionskinetik von katalytischen Reaktionen auf wohl-definierten Einkristalloberflächen zu untersuchen, wurde eine Ultrahochvakuum-Molekularstrahlkammer aufgebaut. Die Oxidationsreaktionen wurden unter isothermen Bedingungen unter Verwendung gepulster Molekularstrahltechniken durchgeführt, wobei die Reaktivität durch massenspektrometrische Messungen von Spezies in der Gasphase charakterisiert wurde. Daneben erlaubt die Apparatur die Aufnahme von IR-Spektren von der Oberfläche unter Reaktionsbedingungen, um gleichzeitig die Entwicklung der Oberflächenspezies zu überwachen. Da Au-Oberflächen molekularen Sauerstoff unter UHV-Bedingungen nicht dissoziieren, verwendet das Experiment einen effusiven Strahl atomaren Sauerstoffs, der von einem thermischen Cracker erzeugt wurde. Als Testreaktion wurde die CO-Oxidation auf der Au(332) Oberfläche betrachtet. Zunächst wurden IRAS-Studien durchgeführt, um eine detaillierte Zuordnung der IR-Schwingungsmodi von ^{13}CO auf der reinen und der O-bedeckten Au(332)-Oberfläche zu erhalten.

In Übereinstimmung mit Literaturergebnissen zeigten IRAS-Studien auf der sauberen Au(332)-Oberfläche bei niedrigen Bedeckungen eine ^{13}CO-Bande mit einem Maximum bei etwa 2075 cm^{-1}, die sich mit zunehmender Bedeckung zu kleineren Wellenzahlen verschiebt. Die sauerstoffbedeckte Au(332)-Oberfläche weist bei mittlerer Bedeckung zwei Schwingungsbanden auf, die sich durch eine höhere Bindungsenergie des CO und eine Rotverschiebung der Linienlage im Vergleich zur sauberen Au(332)-Oberfläche auszeichnen. Kern dieser Arbeit ist die Untersuchung der CO Oxidation auf der Au(332) Oberfläche. Die transiente Kinetik dieser Experimente liefert eindeutige Beweise für ein komplexes Reaktionsszenario, das über eine einfache Oxidation von CO mit Sauerstoffatomen hinausgeht. Darüber hinaus zeigten die Ergebnisse die günstige Wirkung von Wasser, von dem bekannt ist, dass es sich im schnellen

Austausch mit adsorbierten Sauerstoffatomen befindet, die wiederum mit dem direkten Pfad für die CO-Oxidation konkurrieren können. Die transiente Kinetik zeigt eindeutige Indizien für Reaktionskanäle, die auf verschiedenen Zeitskalen ablaufen und durch die Wahl des Wasserpartialdrucks beeinflusst werden können. So konnte im speziellen gezeigt werden, dass bei hohem Wasserpartialdruck das System eine stationäre Reaktivität annimmt. Aufgrund der verwandten Molekularstrahltechniken ist es möglich, aus der beobachteten transienten Kinetik zu schließen, dass die Oberfläche unter stationären Reaktionsbedingungen eine signifikante transiente Sauerstoffkonzentration aufweist, die beim Ausschalten der Sauerstoffatomquelle abreagieren kann. Die letztere Beobachtung hat direkte Implikationen für die Reaktivität von np-Au, für das eine Erhöhung der Reaktivität, vor allem aber eine Reaktivierung des Systems durch Wasser gefunden wurde.

Contents

List of Figures

1 Introduction

Heterogeneous oxidation reactions catalysed by metals have long been of academic and industrial interest[6]. Catalytic partial oxidation of hydrocarbons and alcohols, in particular, is of immense importance because it is the basis for various large-scale processes of both commodity chemicals and valuable precursors for many specialty processes[6]. The coinage metals have demonstrated unique characteristics for selective oxidation catalysis. For example, transformation of methanol to formaldehyde is achieved by silver catalysts; epoxidation of ethylene with supported silver and copper particles has become a mature industrial process applied worldwide[7].

Catalytic partial oxidation reactions have a great economic importance; however, the corresponding processes face a number of challenges. A significant problem is to find an active but still selective catalyst, as increasing activity oftentimes reduces selectivity, which may lead to an enhanced total combustion to CO_2 and H_2O. Another intriguing difficulty is that currently the rational design of catalytic systems is rather the exception than the rule. To date progress in heterogeneous catalysis mainly relies on “trial and error” studies. Recently, there has been tremendous interest in developing new reaction processes to realize the goal of “green chemistry” which aims at maximizing product yield, reducing energy consumption, and minimizing pollution. To this end, heterogeneous catalysis has the potential to play a central role in such processing.

Thirty years ago Haruta[8] showed that well-prepared gold nanoparticles (NPs) are capable of interesting catalytic reactions and since then, there has been a growing effort at exploiting some of the unique properties of gold for fundamental and industrial applications. Several reactions have been reported including propylene epoxidation[9,10], coupling reactions of methanol[11,12], water-gas shift reaction[13–15], NO reduction[16], and of course low temperature CO oxidation[17–20]. Among these reactions, low temperature CO oxidation is one of the most unique regarding gold catalysts and it has gained much interest in the catalysis community.

It is generally accepted that gold clusters of 2-5 nm supported on metal oxides exhibit the highest activity for CO oxidation[21], however many other details about this reaction are far from being completely understood. In particular, the reaction mechanism, details about the oxidation state of active gold, the effect of the metal oxide support, whether atomic or molecular oxygen is the reactive species and, the last but not least the role of moisture, which has drawn attention from both fundamental and technological application[22].

The reports on the catalytic activity of gold presented above, dealt with gold nanoparticles dispersed on oxide supports. Irrespective of the uncertainty with respect to many details it was, however, common understanding that catalytic activity requires Au nanoparticles of a few nanometers in diameter. To this end it came as a surprise that nanoporous gold (np-Au), a purely metallic material prepared by de-alloying of an appropriate alloy e.g. AgAu, can have significant chemical activity and has emerged as very promising catalyst for a variety of catalytic processes[23–25].

Np-Au consists of an interpenetrating network of gold ligaments and voids. Due to the de-alloying processes used to prepare the structure, a small residual amount of the less noble metal – in case of AgAu alloys Ag- remains in the material. Depending on the preparation conditions this leads to at least 1% residual silver[26,27]. Np-Au provides a relatively high specific surface area (typically in the range of 10 m^2/g), electrical and thermal conductivity, facile recyclability, e.g., if dispersed in liquid reaction media, and a finely tuneable porous structure without the need of a support[24].

Np-Au has been demonstrated to be a versatile catalyst for various oxidation reactions such as low-temperature oxidation of CO[17,28,29], highly selective oxidation of alcohols[11], and for cross-coupling of dissimilar alcohols[12]. However, various open questions still remain such as the role of steps or the importance of water for the understanding of the catalytic properties.

TEM tomography studies have shown that the internal surface of np-Au involves a complex arrangement of low- and high-index surfaces and a high density of atomic steps[30,31]. The corresponding presence of a high concentration of low-coordinated surface atoms has been predicted to be one of the origins for the high catalytic activity of small gold nanoparticles[19,32–34]. This is because low-coordination atoms are expected to interact more strongly with

molecules owing to their modified local electronic structure (in particular, a local up-shift and narrowing of the d-band[19]), leading to reduced reaction barriers relative to close-packed gold surfaces[34]. However, simply comparing specific surface areas to assess the relative activity of np-Au and gold nanoparticles can be misleading, as it does not describe differences in the concentration of various active surface sites[35].

Water is a particularly important molecule for oxidation catalysis and its influence on the reactivity of Au catalysts was elucidated. Haruta and Daté[36] have reported that water promotes CO oxidation on Au/TiO_2 by almost two orders of magnitude. They proposed that water plays two possible roles during CO oxidation. The first role is related to the activation of molecular oxygen at the interface between the Au nano-particles and the support, allowing subsequent CO oxidation. The second role is associated with the decomposition of carbonates formed during the reaction. Both possibilities point to the fact that water can be involved in the mechanism of CO oxidation. In the case of np-Au and a stoichiometric supply of reactants, the conversion of CO increases by about 100% just by adding 0.01 vol% water to the gas stream[25]. By adding water to the gas feed, the catalytic conversion can be enhanced by more than 100%. However, when no oxygen was present, the reaction immediately ceased. The results from these two different systems gold nanoparticles as well as np-Au have suggested that water is capable to stabilize the catalyst for CO oxidation at near-ambient temperatures. Moreover, recent studies have emerged confirming that water enhances CO oxidation on gold single crystals[37,38].

The initial experiments on single crystalline surfaces, namely well annealed and sputtered Au(111) surfaces, have demonstrated that investigations on model surfaces are able to provide mechanistic insights to understand the catalytic properties of the np-Au[39,40]. While these studies have provided important insights, they also lack important ingredients of the catalytic system. To this end it is important to recall that the experiments on model systems described thus far rely on Au surfaces pre-covered with activated oxygen species. This strategy hampers the determination of reaction kinetics as all experiments are transient in nature. Furthermore, the model systems used

so far were mostly low index surfaces of Au, which lacks important properties of np-Au namely the high density of step sites present in ligaments of the structure.

Within this thesis a project will be described, which tries to address some of the open questions not being tackled by model studies up until now. In particular, an ultrahigh vacuum chamber was setup, which combines molecular beam techniques and *in situ* infrared spectroscopy. This apparatus has been specifically designed to study the reaction kinetics on single crystal surfaces in a well-defined manner and combine the information on the reaction kinetics with spectroscopy information on the surface species present during the reaction. This strategy was shown to be capable to accomplish these goals[41,42].

In this dissertation, Au(332) surface is investigated and serves as a model surface to elucidate the role of low-coordinated sites present at the steps and kinks of np-Au. The atomic arrangement of the 332 face of Au is discussed in detailed in **Chapter 5**. With respect to elucidate the steady state reactivity of the system the molecular beam apparatus was extended with a thermal oxygen cracker, which is an effusive source with a well-defined flux of oxygen atoms for a given set of experimental conditions namely the oxygen flux and the temperature of the Ir tube.

The present thesis is organised as follows: **Chapter 2** provides an overview over dynamic and kinetic processes, which may take place on catalyst surface as well as the principles of the techniques employed in this work. **Chapter 3** describes the molecular beam apparatus, which has been set up during this thesis and was used to acquire the data presented in the subsequent chapters. **Chapter 4** describe experimental details in particular the alignment and characterization of the effusive sources as well as an initial calibration of the atomic oxygen source using Auger spectroscopy. The preparation and characterization of the Au(332) surface is described in **Chapter 5**. The results concerning the adsorption of ^{13}CO on the bare and O pre-covered Au(332) surface obtained by IR spectroscopy will be presented in **Chapter 6**. **Chapter 7** discusses isothermal molecular beam experiments of CO oxidation using atomic oxygen on Au(332) surface. Apart from the time-evolution of gas phase products monitored by time-resolved mass spectrometry the chapter also

discussed the nature of surface species present during the reaction as characterized by IRAS. Finally, a systematic study of the influence of water on CO oxidation over the Au(332) surface is presented in **Chapter 8**.

2 Theoretical Background

2.1 Dynamics and Kinetics Processes at Surfaces

A comprehensive understanding of chemical reactions and energy transfer at gas–solid interface requires an atomistic insight into the kinetics and the dynamics of the underlying surface processes. This is an intricate task as most reactions involve several elementary reaction steps which result in a complex reaction network. The detailed nature of the latter determines the activity and selectivity of the surface as well as the observed apparent kinetics.

To gain atomistic understanding of a catalytic reaction, it is important to obtain information on the elementary steps as shown schematically in **Figure 2.1**. In a simplifying model proposed by Kisliuk and others in the mid of the last century, a gas phase molecule or atom approaching a surface will collide with the surface[43]. The result of the collision depends on the dynamics of momentum and energy transfer with the surface. If these processes are slow, the molecule will be scattered back into the vacuum.

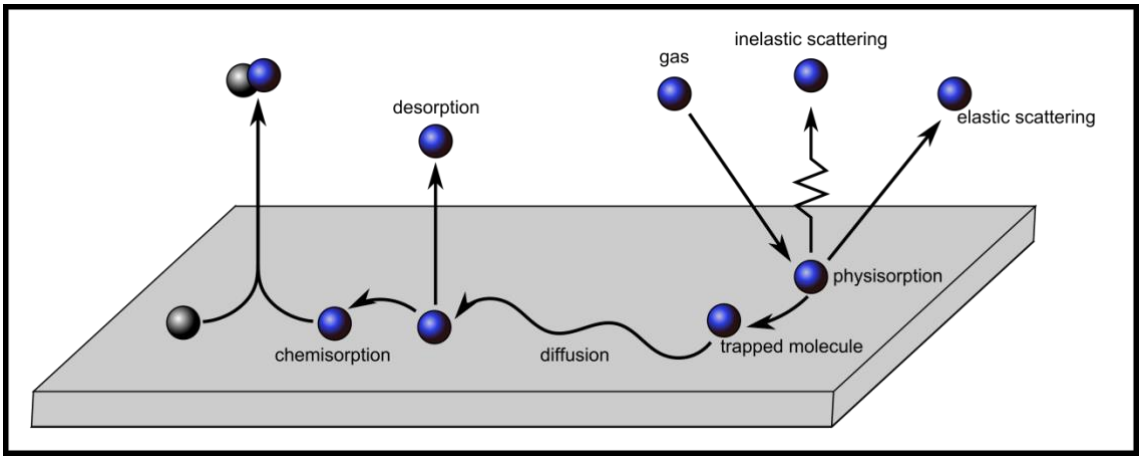

***Figure 2.1**: Schematic representation of basic processes in gas–surface interactions.*

Alternatively, impinging moieties can become trapped on the surface in a so-called precursor state. Upon additional loss of energy and momentum, the

species will be adsorbed on the surface or alternatively desorb back into the gas phase. While being in the precursor state, the molecules can diffuse across the surface and may react with another species present on the surface. In the following, the different processes involved in such a simplified scheme will be described in more detail:

Scattering – Molecules or atoms may be scattered off the surface after collision. Two situations called elastic and inelastic scattering should be discriminated. In case energy and momentum of the molecule or atom are conserved, the process is called elastic, whereas both quantities are typically altered for inelastically scattered molecules[44].

Chemisorption and Physisorption– In principle there is not a sharp distinction between the two cases. Both describe the adsorption of a species on the surface and are distinguished by the strength of the interaction. The term physisorption is used to describe a weak interaction between adsorbate and surface e.g. via van der Waals attractions. The adsorption of a noble gas on a metal surface with typical binding energies between about 2 kJ mol^{-1} for H_2 on W(111)[45] and 29 kJ mol^{-1} for Xe on Ru(1010) may serve as typical examples for physisorption[46]. Please note that van der Waals interaction is always present and is always attractive. While the individual contribution may be small the overall effect may lead to sizeable adsorption energies as e.g. observed for long chain alkenes. Even though, their adsorption energy can be in the range typically associated with chemisorption (see below) the interaction is predominately of dispersive nature. On the other hand, the term chemisorption is used to indicate a strong interaction between the adsorbate and the surface. Typical binding energies are found ≥ 100 kJ mol^{-1}, e.g. the binding energy of an oxygen atom on Au is about 220 kJ mol^{-1} [47]. The strong interaction is often associated with the formation of a chemical bond between the adsorbate and the surface. While it is rather save to assume the formation of a bond in case of strong interaction between surface and adsorbate, the latter might still hold for weakly bonded systems as well. To this end it has e.g. been shown that significant hybridization of molecular orbitals have been observed for water on graphene, which is, however, only weakly bound[48]. The latter effect is found in

case repulsive interactions contribute significantly to the overall binding of the adsorbate.

Trapping – This term describes the adsorption of a molecule into a surface potential well[49,50]. In doing so, the trapped molecule must lose momentum perpendicular to the surface. Hence, the trapping probability is determined by the efficiency of energy transfer processes, which involves the kinetic but also the rotational and vibrational energy of the molecules. The dynamics of this dissipation process depends on the coupling of the incoming atom or molecule to the bath of low energy loss channels such as phonons or electron hole pairs[51].

Precursor state – For a description of the adsorption process the concept of a precursor state has been developed. The precursor state is thought to be the state into which an atom or molecule is trapped in case it has lost sufficient energy upon collision with the surface. Within the precursor state molecules are only weakly bound and typically exhibit low diffusion barriers. Hence, they are mobile on the surface and may either find an adsorption site, react with another adsorbate or desorb back into the vacuum. Due to the low barriers for the various processes the lifetime of a precursor state is short (microsecond rage)[52]. The surface potential is usually affected by the presence of adsorbates, hence, is the precursor state. To distinguish between the two situations one may distinguish between a so-called intrinsic state, associated with the clean surface, and an extrinsic state, being modified by the presence of adsorbates[43,53]. This scenario is illustrated in **Figure 2.2**.

Sticking – The sticking probability *S* is the fraction between the gas molecules residing on the surface for a long time and those impinging on the surface. The sticking probability is generally a function of surface coverage (Θ). Within the terminology introduced above an atom or molecule is considered to stick to a surface in case it has successfully transferred its energy to the surface and adopt a long-lived adsorption site.

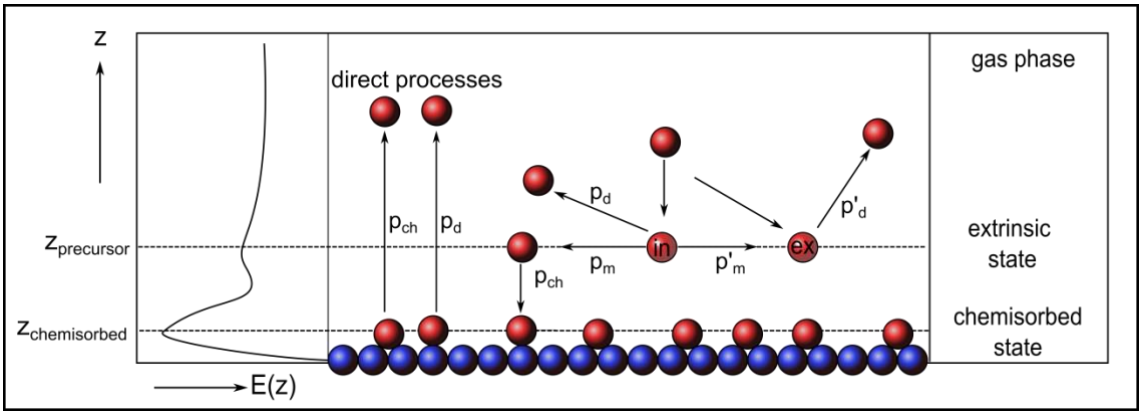

***Figure 2.2**: Schematic representation of the possible kinetic processes occurring at a metal surface (blue spheres) as a function of the distance z perpendicular to the surface. Direct processes are indicated by the probabilities p_{ch} for chemisorption and p_d for desorption. In addition to that, precursor, migration, and adsorption are considered by their respective probabilities: p'_d desorption from extrinsic state, p_d desorption from the intrinsic state, and p_m (p'_m) for migration in the intrinsic and extrinsic state, respectively. In the left side the potential energy pertinent to these processes.*

Diffusion and desorption – In case the barriers for lateral motion or desorption into the vacuum can be overcome at an appreciable rate, the dynamics of the atoms or molecules can no longer be described by vibrations (see below). In the simplest approximation, the lateral mobility can be described as an isotropic 2-dimensional lateral diffusion, which can be thought of as a thermally activated hopping between adsorption sites being separated by potential barriers. In case the diffusion is laterally isotropic it can be described by a simple Brownian diffusion model, in which the square root of the mean square distance is given by

$$\langle r^2 \rangle^{1/2} = \sqrt{4Dt} \qquad \mathbf{1}$$

where D is the isotropic self-diffusion coefficient. If describing diffusion as a thermally activated hopping process in a uniform potential, the diffusion coefficient can be described in a simple Arrhenius model using a pre-exponential factor D_0 and activation energy for diffusion E_{diff}:

$$D = D_0 exp\left(-\frac{E_{diff}}{kT}\right) \qquad \mathbf{2}$$

The description of desorption follows the same Arrhenius model for the probability to overcome the barrier for desorption characterized by an activation energy E_{act}^{des}. A quantitative description of the desorption kinetics requires a proper rate equation, which has to take into account the dependence of the rate on the activation energy as well as the surface coverage (Θ). A possible solution is the so-called Polayni-Wigner equation, which describes the rate of desorption as

$$r_{des} = -\frac{\partial \Theta}{\partial t} = \Theta^n k_0^{des} exp\left(-\frac{E_{act}^{des}}{k_B T}\right) \qquad \mathbf{3}$$

where *n* is the order of the reaction, k_0^{des} is the pre-exponential factor, *T* is the surface temperature and E_{act}^{des} is the activation energy for desorption.

2.2 Surface Reactions

Surface reactions are typically classified into two generic types, the so-called Langmuir–Hinshelwood (LH) or Eley–Rideal (ER) reactions. The LH mechanism assumes a reaction between two adsorbates, e.g. A and B or between an adsorbed species and a vacant site which is to say that both reactants are equilibrated with the surface. On the other hand, the ER mechanism describes the direct interaction of a gas–phase species with an adsorbate species to form a product which either remain adsorbed or desorb into the gas phase. **Figure 2.3** shows schematics of both types of bimolecular reactions on surfaces.

In UHV most of surface reactions follow a LH mechanism. Initially, the species A and B adsorb, then the adsorbed A and B react to the product AB through an adsorbed transition state complex A–B. Finally, the resulting product AB may desorb from the surface. In a simple Arrhenius picture the rate of the elementary reaction is dependent on the surface coverages of both species Θ_A and Θ_B and the activation energy E_{act} and can be written as:

$$\frac{d\Theta_{AB}}{dt} = k_0 exp\left(-\frac{E_{act}}{k_B T}\right)\Theta_A\Theta_B \qquad \textbf{4}$$

where k_0 is the so-called pre-exponential factor.

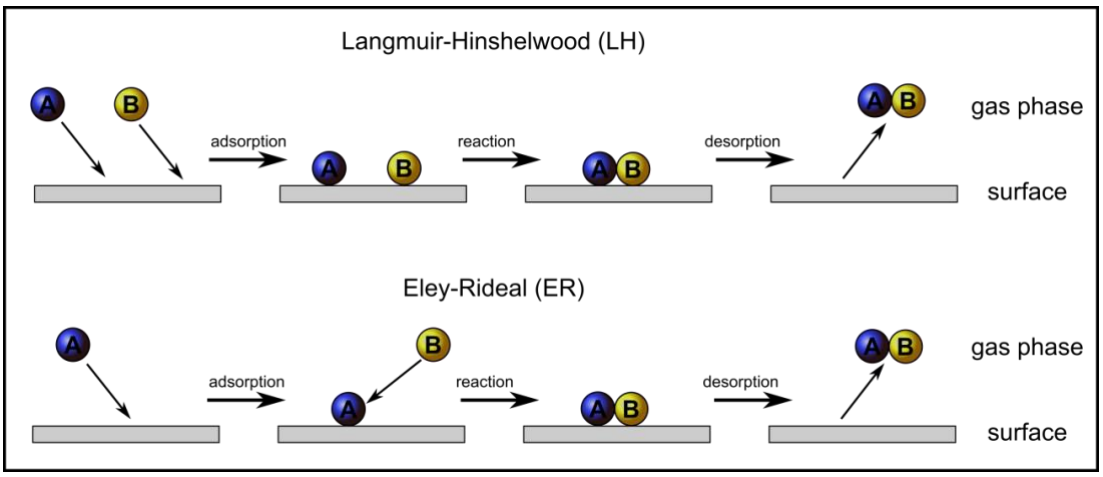

***Figure 2.3**: Schematic illustration of the LH and ER reaction mechanism.*

2.3 Molecular Beams

Molecular beam (MB) techniques are well-established experimental strategies, which may allow controlling the flux, the direction as well as the energy of molecules in a well-defined manner. In contrast with flow reactor studies, the MB approach allows to design the experiment such that each molecule hits the sample surface only once. Thus, a molecule impinging on the surface can either be scattered back into the gas phase or be adsorbed and subsequently may react with other molecules. In case reactions on planar surfaces are studied under the condition of single collision, it is possible to formulate the following conditions:

(i) Determination of absolute reaction probabilities is possible due to the single molecule–surface interaction.

(ii) The low background pressure resulting from the directional molecular beam, allows a detection of the scattered and desorbing molecules and the desorbing reaction products.

(iii) Fast/flexible beam flux modulation and the lack of transport limitations allow for an evaluation of steady–state and transient kinetics.

(iv) Collision–free detection of scattered and desorbing molecules allows to measure angular distributions and internal excitation states of molecules upon collision with a surface without disturbances.

Several reviews are available, which describe various aspects of molecular beams to study the dynamics of atoms or molecules as well as reaction kinetics (e.g.[41,42,51,54,55]). The following sections will be restricted to some aspects being of particular importance for the forthcoming discussion namely, the generation and properties of effusive molecular beams and their use in catalysis.

Two classes of molecular beam sources can be distinguished: effusive and supersonic beams. The two can be differentiated by the expansion conditions and are classified by the Knudsen number K_n, which is the ratio of the mean free path λ of the gas in the source to the source orifice diameter $d (K_n = \lambda/d)$.Under conditions of molecular flow,$K_n \gg 1$ characterizing an effusive beam whereas, $K_n \ll 1$ results in a supersonic expansion in case the pressure on the low-pressure side of the source is sufficiently low[1]. In the apparatus used in this thesis, only effusive sources are used. Therefore, the following description will be limited to these beams.

2.3.1 Effusive Beams

Low energy or effusive beams operate at large Knudsen numbers $(K_n \gg 1)$. The molecules are in thermal equilibrium with the apparatus, hence, the velocity distribution of molecules follows a Maxwell-Boltzmann distribution and all degrees of freedom are characterized by the source temperature T_{source}.

A thin-walled orifice is the simplest design of an effusive source, see **Figure 2.4A**. Molecules that leave the thin-walled small orifice are distributed according to a cosine law[49,55]. In order to ensure the single scattering condition

described above, the effusive beams should provide a constant pressure of molecules over the entire surface area and should minimize the number of molecules entering the UHV apparatus but not hitting the surface. To this end, it has been found that using tubes with a large aspect ratio of length (L) over radius (r) instead of a thin-walled orifice result in a forward focussing of the effusive gas beam[1].

The collimation is described in terms of a so-called *peaking factor* κ, which is defined as the ratio of the total centreline flux $I(0)$ relative to the centreline intensity of a cosine distribution at total flux $\dot{N}$. At low pressure, the peaking factor can be approximated as[1]

$$\kappa = \frac{\pi}{\dot{N}} I(0) = \frac{3L}{8r} \qquad \textbf{5}$$

The typical value of the peaking factor for a single cylindrical channel is approximately 15, corresponding to a L/r ratio of about 40. With respect to the design of the effusive beams two aspects need to be considered: First, one's commitment to fulfil a high Knudsen number. Secondly, the flux impinging on the surface should be as high as possible while the single scattering conditions are preserved i.e. one needs a high peaking factor. From an experimental point of view, it is also important to control the pressure on the source side of the channel and make sure that the gas flowing through the channel is clean. In particular, the latter is much easier to fulfil in case of higher pressures (typically $p>10^{-3}$ mbar) on the source side. Typically, effusive beams operate with pressures between 10^{-3} and a few mbar, which in turn requires narrow channels (< 100 μm) to be able to fulfil the single scattering conditions. The homogeneity of the flux profile can be increased further if not a single channel but an array of channels is used. To this end, glass capillary arrays (GCA) with a small diameter of the individual channel can be used. The main advantages of using a GCA in effusive beams are: (i) relatively high pressure on the source, (ii) improved homogeneity of the flux as compared to a single channel, (iii) a low consumption of gas due to the improved directionality of the beam (compared to a single channel) and therefore also a reduction in required pumping speed. A

schematic illustration of the focusing effect of a GCA and the corresponding angular distribution as a function of the length and radius ratio of the channels is displayed in **Figure 2.4B**.

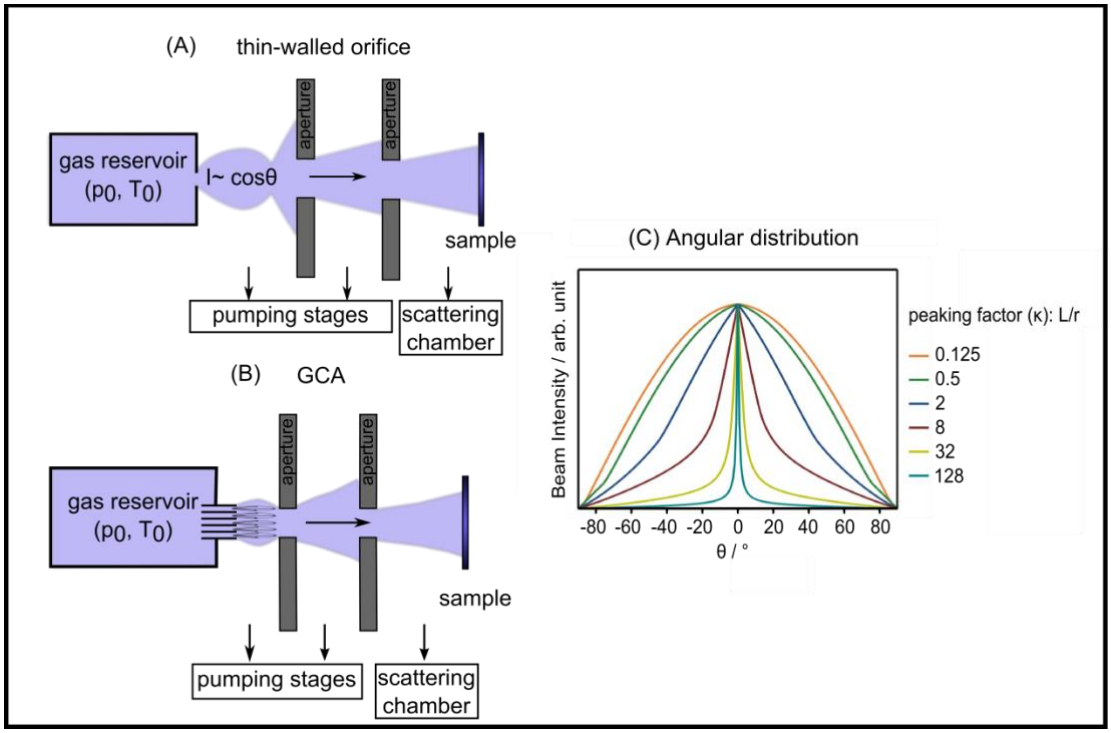

***Figure 2.4**: Schematic representation of the different types of effusive source (**A**) thin-walled orifice and (**B**) glass-capillary array (GCA). **(C)** calculated angular distributions for the gas flux through a GCA adapted*[1,2].

2.3.2 Effusive Beam Generation

The setup of an effusive MB is schematically illustrated in **Figure 2.5**. A glass capillary array is used as the effusive structure. The flux of molecules is further shaped by two apertures separating two pumping stages, which help to separate the part of the beam directed onto the sample from the rest contributing to the background. The beam can be modulated by a motor driven shutter, which permits to obtain the desired temporal structure of the incoming beam.

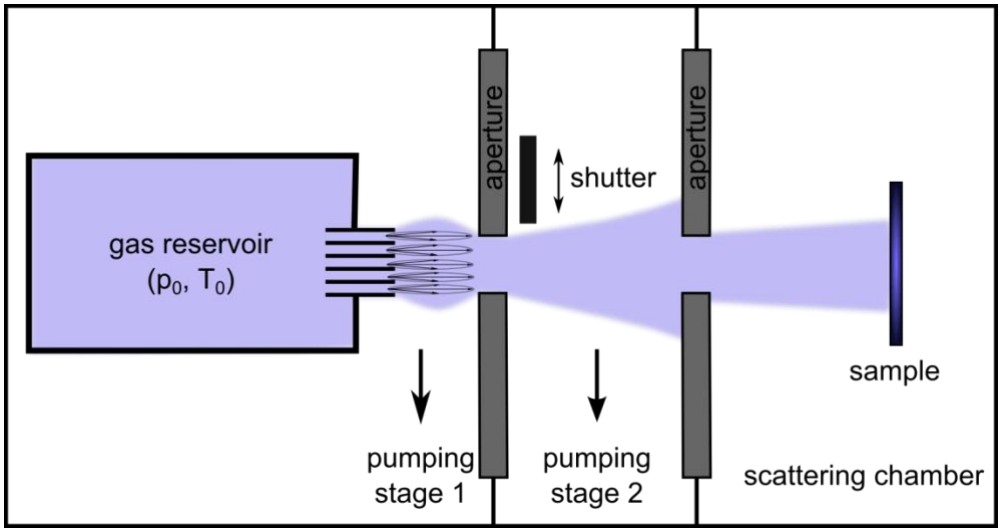

***Figure 2.5**: Schematic illustration of an effusive molecular beam source with GCA.*

2.4 Infrared Spectroscopy

Infrared spectroscopy is a common technique in catalysis to characterize adsorbed molecules on solid surfaces[56,57].In particular, IR radiation excites vibrational modes of adsorbed molecules, which can be used to gain insight into the chemical nature, the bonding or the chemical environment of the species. Several experimental geometries are used depending on the sample to be investigated[58]. On metal surfaces IR spectroscopy is typically done in grazing incidence reflection geometry called infrared reflection absorption spectroscopy (IRAS).

2.4.1 Molecular Vibrations

The IR spectrum results from transitions between quantized vibrational states. For a typical IR spectrometer, the interaction of the radiation with the vibrational modes can be described within the dipole approximation. For low intensity radiation absorption can be described within time-dependent perturbation theory using the electric dipole Hamiltonian as the perturbation operator:

$$H^{(1)}(t) = -\vec{\mu} \cdot \vec{E} \qquad \mu = \mu_0 + \sum_k (\partial\mu/\partial Q_k)_0 Q_k \qquad \textbf{6}$$

where μ is the electric dipole operator and E the electric field of the radiation. Within the perturbative treatment the intensity of the absorption is proportional to the square of the matrix elements between the two vibrational states and the dipole moment. The latter is the expectation value of the dipole operator over the wave function describing the electronic state of the molecule. The evaluation of the matrix element is intricate as the dipole moment is a function of the vibrational state. This can be taken into account by expanding the dipole moment into a Taylor series around the equilibrium geometry. This expansion has to be done with respect to all normal coordinates Q_k (3N-6 for non-linear molecules) of the molecules as indicated above. Truncating the Taylor series after the first order term and using the fact that any two eigenvalues of a normal mode are orthogonal, the transition matrix element can be written as,

$$\langle \psi(v)'_k | \mu | \psi(v)_k \rangle = \left(\frac{\partial \vec{\mu}}{\partial Q_k} \right)_0 \langle \psi(v)'_k | Q_k | \psi(v)_k \rangle \qquad \textbf{7}$$

where $\psi(v)_k$ and $\psi(v)'_k$ are vibrational eigenfunctions of a normal mode k in the initial and final states, respectively[59]. The term $(\partial\vec{\mu}/\partial Q_k)_0$is the so-called dynamic dipole moment. Thus, an infrared mode is IR active if the dynamic dipole moment is nonzero. Furthermore, a non-vanishing matrix element on the right-hand side of **Equation 7** is found if $\Delta v = \pm 1$.

2.4.1 Fourier Transform Spectrometry

Nowadays, modern infrared instruments are Fourier transform spectrometers. In dispersive spectrometers, the frequency decomposition of the polychromatic light is obtained using gratings or prisms. Thus, spectra are taken by a serial scanning of different wavelengths. Instead, Fourier transform IR spectrometers utilize a Michelson interferometer to encode the spectral

information of a white light source in terms of an interference pattern[3,60]. A Michelson interferometer is shown schematically in **Figure 2.6**.

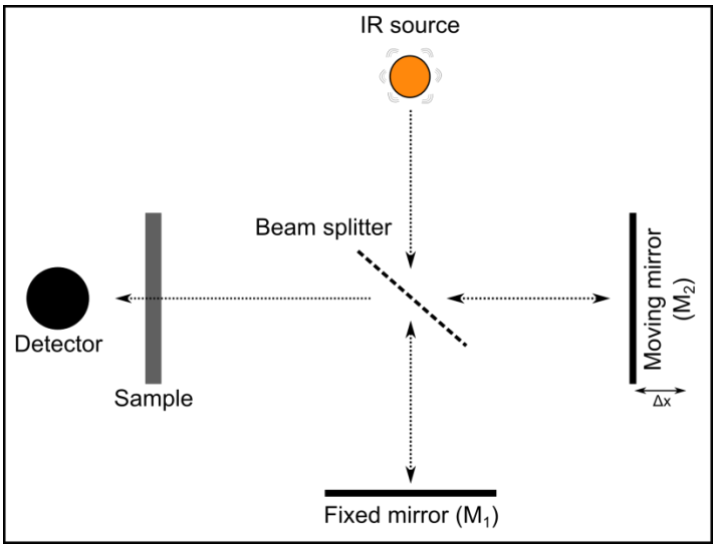

***Figure 2.6**: The schematic diagram of a Michelson interferometer.*

The operation principal of a Michelson interferometer is to divide the beam in two paths using a beam splitter. One beam moves towards a fixed mirror *M1*, while the reflected part travels to a moving mirror *M2*. The two reflected beams interfere at the beam splitter and the reflected (M_1) and transmitted (M_2) part of the beam will be directed to the sample and later be focussed onto the detector. The signal intensity $I(x)$ at the detector is measured as a function of the position$x$ of mirror 2, which results in the so-called interferogram (see **Figure 2.7A**). It is readily clear that the highest intensity is found for zero path difference between both mirrors, because all frequencies will interfere constructively. It can be shown that the observed interferogram $I(x)$ can be converted into a spectrum $S(\tilde{\nu})$ by means of a Fourier transformation resulting in the so-called single channel spectrum (see **Figure 2.7B**). The Fourier transformation transforms the path difference, which is a length, into a reciprocal length also known as wavenumber $\tilde{\nu}$ ($\tilde{\nu} = \lambda^{-1}$):

$$S(\tilde{\nu}) = \frac{1}{2\pi} \int_{-\infty}^{\infty} I(x) \exp(-2\pi i \tilde{\nu} x)\, dx \qquad \mathbf{8}$$

Unfortunately, the single channel spectrum includes the characteristics of the spectrometer (intensity profile of the source, the frequency dependence of the sensitivity of the detector, absorption on various optical elements etc.) and presumably the signal of interest. In order to eliminate the contributions from the spectrometer, two spectra are taken: First a so-called background spectrum is acquired, which is taken for the sample without the species whose spectrum is to be measured and subsequently an acquired spectrum of the sample with the substance of interest. After proper subtraction of the background from the sample spectrum one arrives at the spectrum of the substance only, which is typically displayed as a transmittance spectrum as displayed in **Figure 2.7C**.

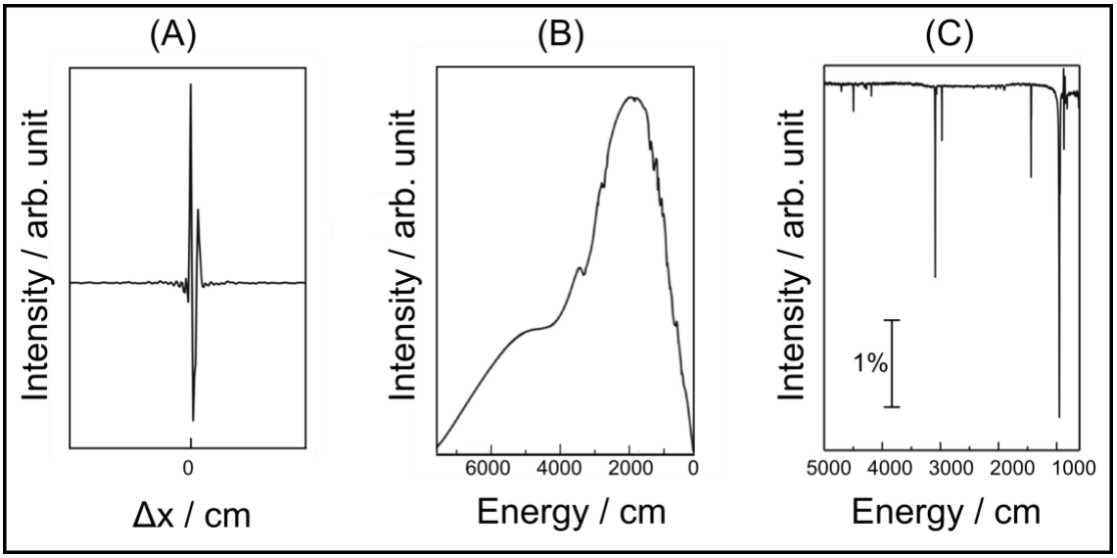

***Figure 2.7**: Fourier transformation path of a IR spectrum: (**A**) interferogram, (**B**) single channel spectrum after FT of (**A**) and (**C**) transmission spectrum obtained by proper subtraction of the single channel spectra with and without the substance of interest, adapted from*[3].

2.4.2 Reflection Absorption Infrared Spectroscopy on Metal Surfaces

Infrared reflection–absorption spectroscopy (IRAS) is widely used in surface science to study the absorption of molecules on metallic surfaces. The infrared (IR) beam is reflected under grazing incidence from a flat reflective surface to optimize sensitivity. The reflection condition is determined by Fresnel equations. A quantitative evaluation of this process can be found

elsewhere[61].The reflection of electromagnetic radiation at a metal surface depends on the polarization of the radiation. Qualitatively, the electric field component of the incoming IR radiation can be described as an electric dipole, which induces an image dipole in the metal. The orientation of the image dipole depends on the polarization of the radiation. For the s-polarized light, for which the electric field is parallel to the surface, the two dipoles cancel out while the component of the electric field normal to the surface is enhanced by the image dipole (see **Figure 2.8**). In turn, vibrations with a transition moment oriented parallel to the surface cannot be excited on metal surface, which is known as the metal surface selection rule.

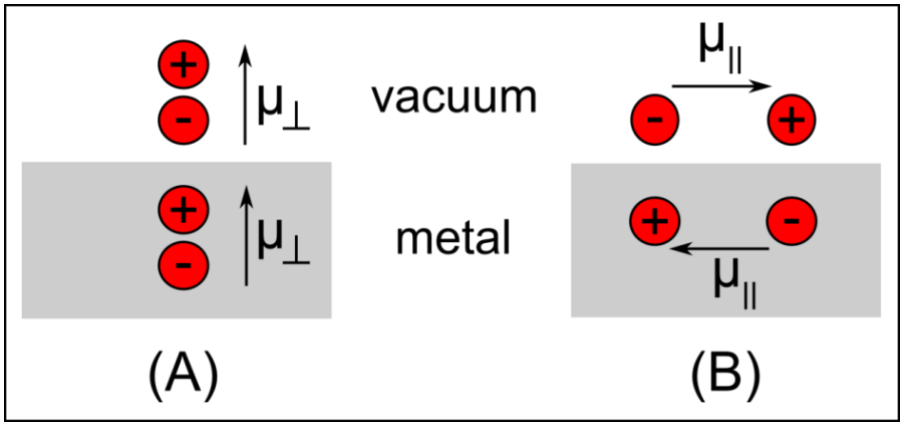

***Figure 2.8**: (**A**) A perpendicular dipole leads to an increase response to the excitation and (**B**) the dynamic dipole of the radiation parallel to the surface is cancelled by the image dipole and no exciting electric field remains.*

Molecules adsorbed on the metal surfaces exhibit frequency shifts with respect to the gas phase due to interactions between adsorbate and the metal as well as inter-adsorbate interactions. Different effects influencing the vibrational frequencies are usually considered, which will be described briefly using carbon monoxide as prototype example, which has been investigated in great detail over the last decades.

(A) Adsorbate-metal interactions

Mechanical renormalization – Attaching a molecule to a surface of much higher mass will influence the vibrational frequencies of the adsorbed molecules

depending on the details of the adsorption geometry and the vibrational mode under consideration. For diatomic molecules adsorbed perpendicular to a surface the mechanical renormalization is expected to lead to a blue shift. For adsorbed CO molecules a shift of about 50 $cm^{-1}$with respect to the gas phase C–O stretch is expected[62].

Chemical shifts – The bonding of molecules to surfaces will change their vibrational properties. It will depend on the details of the adsorption such as coordination number of the adsorption site. For CO molecules, the Blyholder model established to describe metal carbonyl complexes, can be used to gain a qualitative understanding of the adsorption properties[63,64]. This model assumes two contributions to the chemical bond between CO and a metal surface. On the one hand, the 5σ orbital of the molecule overlaps with unoccupied states of the metal, which is called σ donation. On the other hand, occupied d-bands of the metal overlap with the unoccupied 2π* orbitals of CO, which is known as π back-donation. While the interaction of the metal with the 5σ orbital, which is of non-bonding character, does not change the stretching frequency of the molecule much, transfer of electrons into the 2π* orbital will weaken the C–O bond and hence reduce the vibrational frequency of the CO stretch (see **Figure 2.9**).

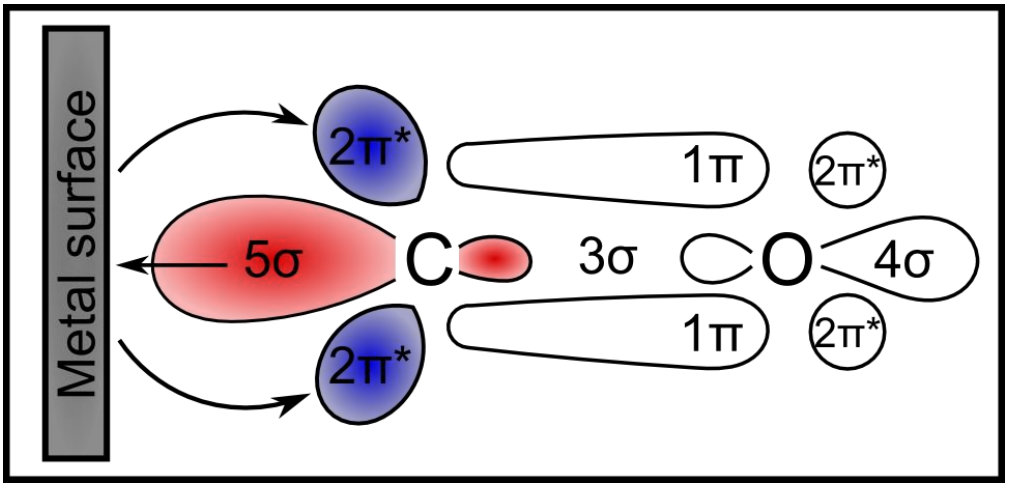

***Figure 2.9**: Schematic representation of the binding of a CO molecule on a metal surface including the contribution of σ donation and π back-donation.*

Dipole self–image shifts – The interaction of an adsorbed dipole with its own image dipole in the metal surface leads to a decrease of the vibration frequency for a CO molecule adsorbed perpendicular to the surface. The effect has been described theoretically by Mahan and Lucas[65] and by Scheffler[66] taking the distance d between an adsorbate and its own image into account (see **Figure 2.10**). They found out that the calculated shifts depend sensitively on the dipole image distance, a quantity which cannot be determined precisely. Moreover, the position of the image plane in the metal is uncertain due to tailing of the metal electron density into the vacuum. However, this model has been proven valuable in giving a semi-quantitative description of experimentally observed image-induced frequency shifts.

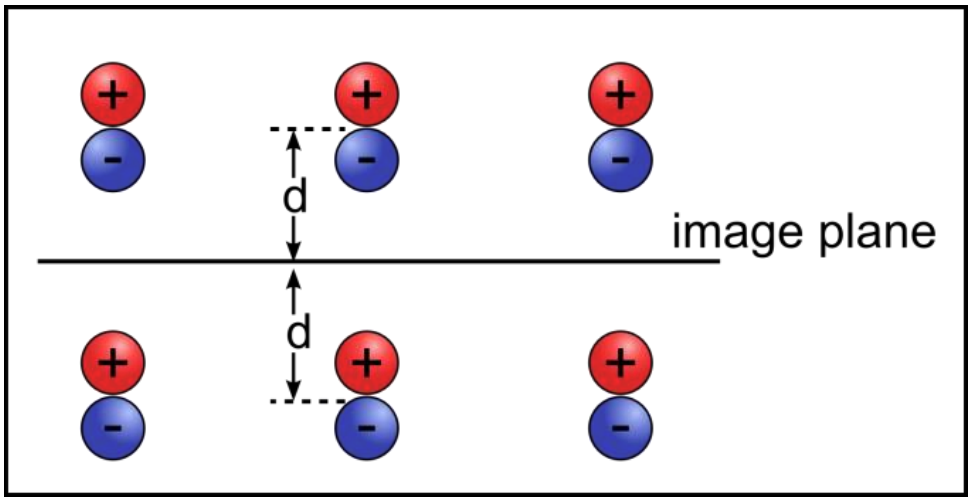

***Figure 2.10**: Induction of image dipoles by real dipoles above a metal surface.*

(B) Lateral interactions

In addition to the effects on the vibrational frequencies of individual molecules adsorbed on metal surfaces, the IR response is strongly altered by inter-adsorbate interactions within the adsorbed layer, which will be described in detail below:

Dipole-dipole coupling – Dipolar coupling of vibrational modes within an adsorbate layer can originate from interactions through space between neighbouring dipoles[66]. The interaction is strongly coverage dependent and was

shown to result in a blue shift of the observed frequency with respect to the singleton frequency of the individual molecule. It is important to note that the coupling of two or more oscillators will result in the equivalent amount of vibrations. For coupled molecules with identical frequencies the in-phase vibration, which has the highest stretching frequency, is the only one with an appreciable intensity[67].

Chemical shift - Apart from the chemical interaction of a single molecule with the metal surface discussed above there is also an influence on the binding properties of a molecule on an adjacent adsorption site. The corresponding effect is usually called chemical shift in literature [30]. The direction of the chemical shift differs from system to system. For coinage metals (Cu and Au) a negative chemical shift was observed, which explains the monotonous red-shift with increasing coverage observed for different single crystal surfaces of Cu and Au[69,70].

In order to experimentally discriminate the two phenomena, it is possible to use isotopic mixtures of adsorbates (e.g. ^{12}CO and ^{13}CO) as the dipolar coupling depends strongly on the frequency difference between the species This effect is observed in the coverage dependence IRAS experiment for ^{13}CO on Au(332) and it will be discussed in **Chapter 6**.

(C) Redistribution of intensity – The frequency of a band in the vibrational spectrum of an adlayer often varies with coverage. In the low coverage limit the intensity of an infrared absorption band is proportional to coverage, i.e. the total change of the dynamic dipole moment:

$$I \propto \left(\frac{\partial \vec{\mu}}{\partial Q_k}\right)^2 \qquad \textbf{9}$$

Moreover, the value of the dynamic dipole is subjected to the impact of changes in chemical bonding between the surface and the adsorbed molecule, and several different contributions to this chemical shift as described above. If the adsorbate layer consists of isotopically identical molecules, the total dipolar

coupling results not only in different eigenmodes of the coupled system, but also in a redistribution of their intensity. For identical isotopomers it was already mentioned above that the highest energy vibration (total symmetric combination mode) is the only mode with a sizable intensity. The effect of the coupling on the frequency shift drops with the inverse of the difference between the square of the frequencies. While the effect on the frequency drops rather fast, there might still be a sizable intensity transfer from the low frequency species towards the high frequency one. This intensity borrowing can significantly obscure interpretation of the spectra.

2.5 Mass Spectrometry

Mass spectrometers are analytic tools to separate ions by their mass to charge (**m/*z***) ratios. The corresponding spectra show the intensity of ions as a function of their m/z ratio. Many different types of mass spectrometers have been designed, which can be classified by their main functional elements: **the source** used to generate ions; **the analyser** used to separate them according to their m/z ratio, and **the detector** used to determine the amount of the ions leaving the analyser[71–73]. Each functional element mentioned above is described in the following.

2.5.1 Ion Source

Depending on the nature of the sample different methods for ion production are used. The simplest and still widely used ionisation method is electron impact. This method is based on a collision between neutral molecules and electrons, e.g. emitted from a hot filament. At electron energies above the first ionization potential of the target molecule, ionization occurs according to the following reaction:

$$M + e^- \rightarrow M^{+\cdot} + 2e^- \qquad \textbf{10}$$

The likelihood of subsequent fragmentation reactions depends strongly on the amount of energy deposited in the molecules upon electron impact. In general, electrons close to the first ionization potential of the molecules will induce little fragmentation, while the fragmentation probability increases with higher electron energies. However, ionization cross sections depend also critically on the electron energy, hence, the ionization energy is a critical parameter, which determines the sensitivity of the experiment. A typical electron energy used in many quadrupole mass spectrometers employed as residual gas analysers is 70 eV. However, the value might be changed if aiming at an optimal sensitivity for a certain molecular ion as the ionization cross section and the fragmentation probability are functions of the electron energy.

2.5.2 Mass Analyzer

The central idea of a mass spectrometer is to measure the mass-charge ratios of ions, thus providing means to identify them. With this in mind, the mass analyzer is responsible to separate the ions according to their **m/*z*** ratios. Many different types of mass analyzer can be chosen, employing e.g. magnetic, electrostatic fields, or quadrupole mass filters. As the mass spectrometer used in this setup is based on a quadrupole filter its principal function will be presented in the following.

As shown in **Figure 2.11**, a quadrupole analyzer consists of four long parallel cylinders. A potential field (Φ) is established by applying a combined DC (U) and RF ($V_0 \cos\omega t$) voltages to these rods. By choosing an appropriate DC/RF ratio, ions of the desired ***m/z*** ratio will pass through the quadrupole and subsequently detected, while unwanted ***m/z*** will be deflected away from the central axis of the rod bundle.

The main advantages to use a quadrupole mass analyzer are: (1) a high transmission, (2) low ion acceleration voltages, (3) capability to tolerate relatively high pressures (up to 10^{-4} mbar), and (4) the opportunity for fast scanning by simply sweeping electric potentials[74].

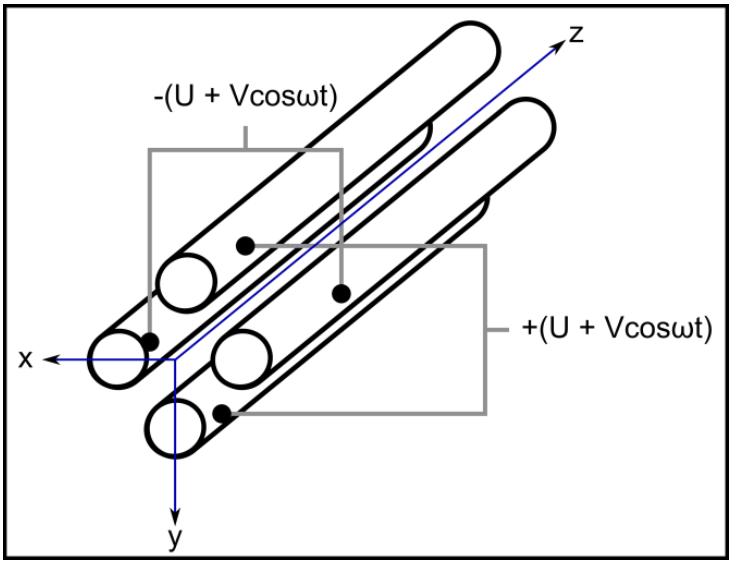

***Figure 2.11**: Schematic of a linear quadrupole mass analyzer.*

It shall be noted that the sensitivity of the analyzer can be increased by adding two shorter quadrupole sections at the beginning and the end of the analyzer, which help to increase the number of ions entering the analyzer on an appropriate path and help to focus those leaving the analyzer to enter the detector. Such a design is known as a triple-filter configuration and is realized in the mass spectrometer used in this setup.

2.5.3 Detector

Instead of the ions, electrons are typically detected in mass spectrometers using electron multipliers (EM). Two types of EM can be distinguished: a discrete dynode type and continuous. Both types of device utilized the phenomenon of secondary electron emission, as depicted in **Figure 2.12**.

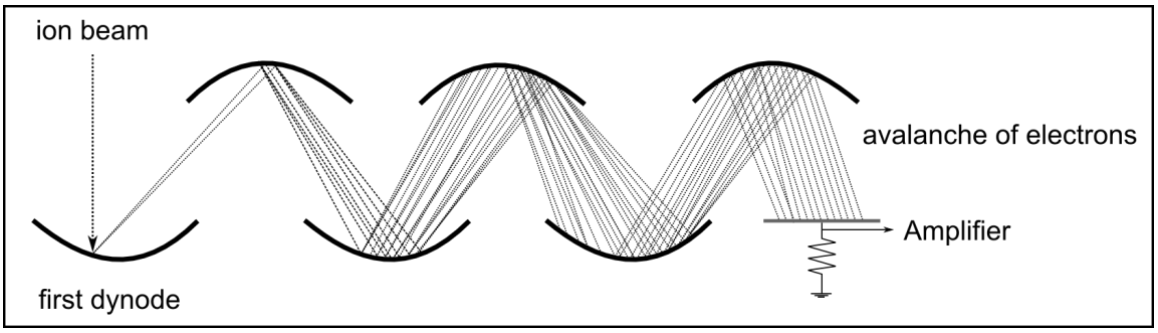

***Figure 2.12**: Schematic illustration of an electron multiplier.*

The ions impinging on the first electrode (conversion dynode) create secondary electrons, which are further amplified by accelerating them onto electron multiplying surfaces downstream the primary electrode. The latter is either accomplished by a set of discrete dynodes as illustrated in **Figure 2.12** or a continuous electron multiplier. The mass spectrometer used in this setup employs the latter.

3. Setup of the Molecular Beam Apparatus

This chapter describes the molecular beam (MB) apparatus, which has been set up within this thesis and has been used to acquire the data presented in the subsequent chapters. **Figure 3.1** shows a photograph of the MB apparatus, which is divided into a preparation chamber (top A) and scattering chamber (bottom B) being separated by a gate valve (DN100CF, VAT).

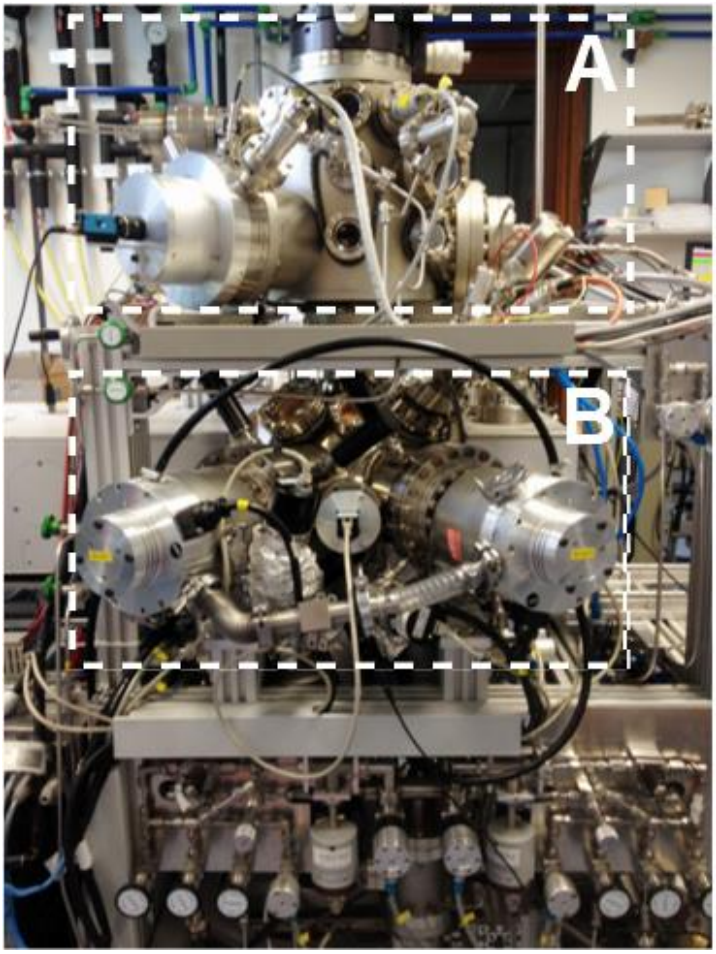

***Figure 3.1**: The molecular beam apparatus. (**A**) Sample preparation chamber and (**B**) scattering chamber.*

A layout of the vacuum system including the gas supply system is schematically shown in **Figure 3.2**. The ultrahigh vacuum (UHV) required for the experiments is produced by means of turbomolecular pumps, which are in turn pumped by two-stage rotary pumps (DUO 5 M, Pfeiffer). The same holds for the molecular beams. The pressure in the two UHV chambers is measured

by Bayard Alpert gauges (350, Granville-Phillips). The typical base pressure of the preparation chamber is $4 \cdot 10^{-11}$mbar (lower limit of the gauge), while the base pressure in the scattering chamber is $1 \cdot 10^{-10}$mbar. Wide range gauges (PTR90, Oerlikon-Leybold) are used to monitor the pressure in the two pumping stages of the molecular beams as well as in the detector chamber of the IR spectrometer. The latter is pumped by a stack of a turbomolecular pump (TMP 50, Oerlikon-Leybold) and a rotary pump (DUO 5 M, Pfeiffer). The vacuum of the rotary pumps is measured using Pirani gauges (TTR91, Oerlikon-Leybold). The pressures of all gauges as well as the various electro-pneumatic valves are controlled by home written Labview software.

In case of a power failure, the electromagnetic valves, separating the pre-vacuum line (rotary vane pumps) and the turbomolecular pumps are closed, which secures the vacuum system from oil contamination. In this case, the ultrahigh vacuum side is vented through flooding valves attached to the turbomolecular pumps mounted on both the preparation as well as the scattering chamber.

In the next sections, a detailed description of the various components mounted on both chambers will be given.

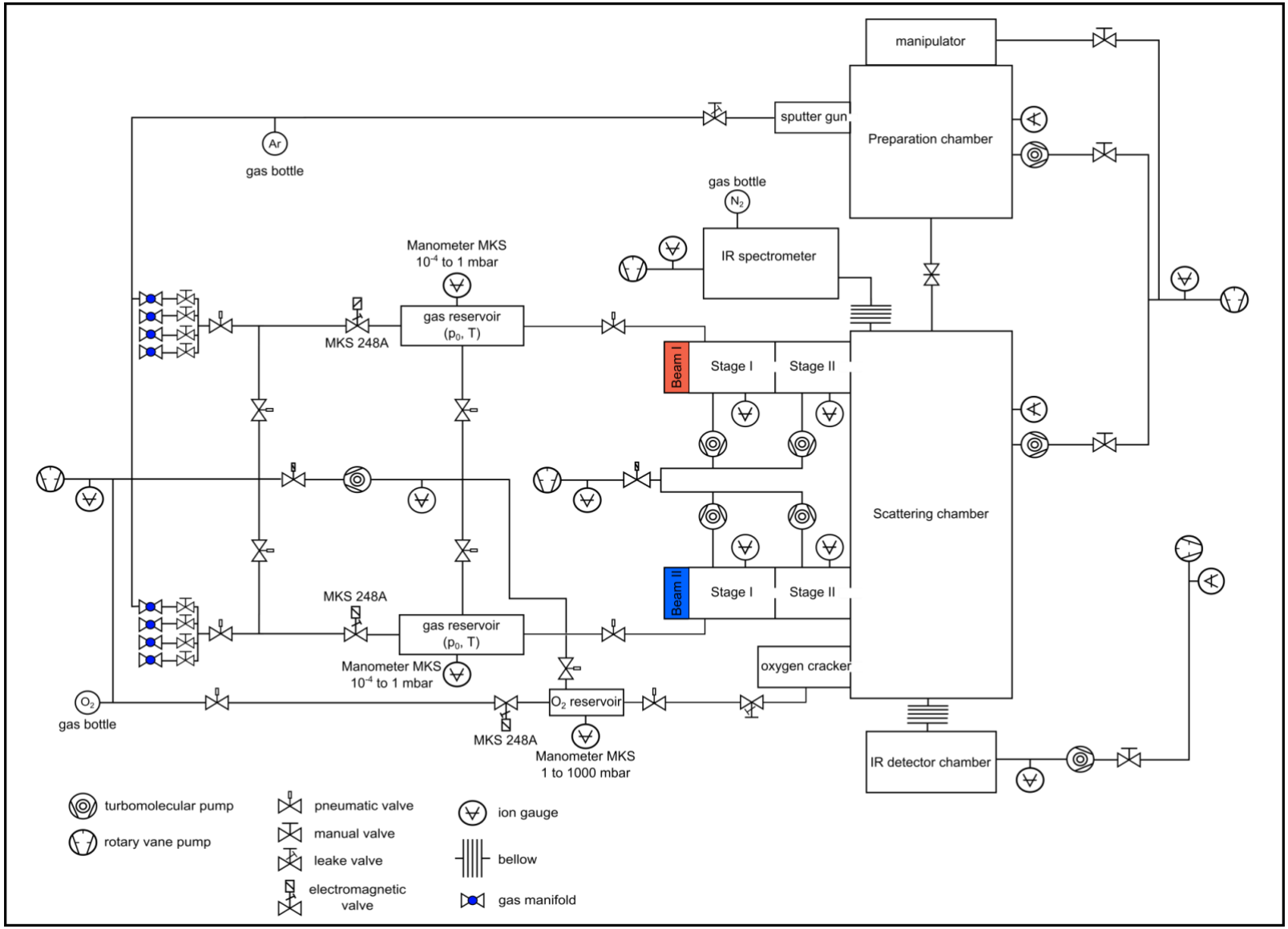

Figure 3.2: *Schematic of the vacuum, pumping and gas inlet system for the molecular beam apparatus.*

3.1 Sample Preparation Chamber

The preparation chamber is pumped by a turbomolecular pump (400 L, Oerlikon-Leybold) and equipped with standard surface characterization and preparation tools: (**a**) sputter gun for cleaning the sample, (**b**) electron beam evaporator and quartz-micro balance for deposition of metals and calibration of their amount, (**c**) low–energy electron diffraction (LEED) and (**d**) Auger electron spectrometerfor the characterization of the long-range order and the chemical composition, respectively. The sample is mounted on a long travel manipulator of 600 mm (HPLTC 60, Vacuum Generators) with a differentially pumped rotary feedthrough to rotate the sample around the long axis of the manipulator.

(A) Sputter gun

The sputter gun is used for sample cleaning. In this apparatus, a sputter gun (IQE 11/35, Specs) is used, which produces a homogeneous ion beam over the entire sample area. The sputter gun is connected to the high-pressure argon cylinder and gas is introduced into the chamber by means of an all-metal leaking valve. Experimental details will be presented in **Chapter 5**.

(B) Electron beam evaporator and quartz crystal microbalance

A commercial electron beam evaporator from Omicron (Focus, EFM3) is used. The evaporator operates at electron beam energies up to 1000 eV, filament currents of 1.6–2.2 A and generates a beam of metal atoms by bombarding a metal wire or a crucible with electrons. In case of Ag evaporated onto the Au samples for some of the experiments, Ag metal was loaded into a Mo-crucible. The electron beam heating produces a certain fraction of metal ions, which are acceleratedaway from the source. To avoid sputtering the sample with these ions, the latter is put on the same potential as the evaporant.

The evaporation rate of an evaporant is calibrated by means of a quartz crystal microbalance. An AT-cut quartz with a nominal diameter of 14 mm and a resonance frequency of about 6MHz is used. The temperature of the crystal is

controlled by an external water cooling (Haake FS). The change in resonance frequency is measured using an Intellemetrix (IL 150) controller, which allows determining changes of the film thickness smaller than1Å depending on the density of the evaporated metal.

(C) Low–energy electron diffraction

Figure 3.3 shows the schematic of a single MPC–LEED (Omicron SER1206) optics mounted in this apparatus. The LEED optics are controlled by two units: a Spectaleed (Omicron Vakuumphysik GmbH) unit controlling all necessary voltages except those needed for the channel plate, which is provided by an additional controller (CPL 534, Omicron NanoTechnology).

An electron beam is generated in the electron gun using an Ir/Th filament and is incident on the sample. The electrons are then backscattered from the sample surface onto a system of grids. The backscattered electrons reach the first grid, G1, which is connected to the ground to ensure that electrons leaving the sample can travel in a field free space. The electrons are then to pass grid G2, which is held at a negative potential to separate the elastically scattered from the inelastically scattered electrons. The elastic electrons will pass grid G3, which is again grounded, and are accelerated towards the microchannel plate (MCP). The MCP acts as an electron amplifier in front of the phosphor screen. The electrons leaving the MCP are further accelerated towards the phosphor screen, which carries a high positive potential (of about 6 kV) to allow for luminescence at the position where electrons impinge on the screen.

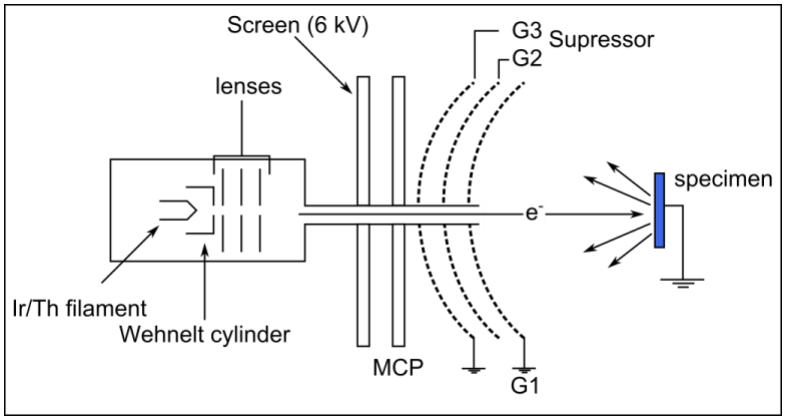

***Figure 3.3**: Schematic diagram of microchannel plate LEED optics.*

(D) Auger Electron Spectrometer

The Auger electron spectrometer (PHI 11–010, Perkin Elmer) is used to determine the chemical composition of the surface. AES experiments were typically performed with electron primary energy of 1.5 kV and an emission current $I_e \approx 1$ mA. The beam diameter of the electrons was found to be about 3 mm. The electrons are created by an electron gun, which is aligned with the center axis of the cylindrical mirror analyser (CMA). The emitted Auger electrons are detected by the CMA according to their kinetic energy using a lock–in detection scheme. The signal is plotted as the second derivative of the pass filtered current, which is proportional to the change of detected electrons, resulting from Auger electrons of kinetic energy E_k.

The analog signal from the lock-in amplifier is fed into an analog-to-digital converter to be recorded and stored using a home written LabView program. The program also controls the kinetic energy of the electrons by means of a 0-10 V ramp, which is mapped by the electronics onto the accessible energy range of the spectrometer. The spectra are typically taken in the center of the crystal, even though test measurements were performed on other spots and did not show differences in the spectra. In order to avoid fluctuation on recorded spectra due to the voltage applied on the pyrolytic boron nitride heater used for temperature control, the measurements were either performed at the lowest temperature (around 100 K) or at room temperature.

3.2 Scattering Chamber

The scattering chamber contains molecular beam sources. Besides that, the scattering chamber is pumped by a 500 L TMP (TMU 521 P, Pfeiffer) and the sample can be transferred from the preparation chamber by the long travel manipulator (HPLTC 60, Vacuum Generators). Gas phase products and residual gases are detected with a quadrupole mass spectrometer (MAX–500HT, Extrel). Simultaneously, surface species are detected using a commercial infrared spectrometer (Bruker IFS 66v/s) with an MCT detector.

3.2.1 Effusive Beam

The scattering chamber contains two effusive sources based on a glass capillary array (GCA), which follow a design introduced by the Libuda and co-workers shown schematically in **Figure 3.4**[4]. As an effusive source a 1mm thick glass capillary array with 25μm wide channels (diameter of 14 mm) (Collimated Holes, Inc.) is used, which is sealed by Teflon gaskets against the primary pumping stage (S1). The CGA is mounted in line of a 12 mm aperture, which serves as the entrance to the second pumping stage (S2). The housing of the primary pumping stage (S1) to which the CGA is mounted is connected to the chamber wall by a bellow, which allows to move this part by means of two orthogonally arranged linear motion feedthroughs. The latter are necessary to allow for a proper alignment of the primary with the secondary, spatially fixed aperture (**Figure 3.4**). The latter limits the secondary pumping stage (S2). A UHV compatible stepper motor (VSS 32.200, MCC2 control electronics, Phytron) is mounted in the secondary pumping stage of the beam to operate a shutter used for its temporal modulation. Typical opening times of the shutter between 50 and 100 ms can be achieved. The two pumping stages, **S1** and **S2**, are each pumped with a 400 L TMP (Oerlicon-Leybold). The pressure measurements for the two pumping stages are carried out by means of two cold cathodes (PTR 90, Oerlikon-Leybold), which allow to measure the pressure in a range between $5 \cdot 10^{-9}$ mbar and 1000 mbar.

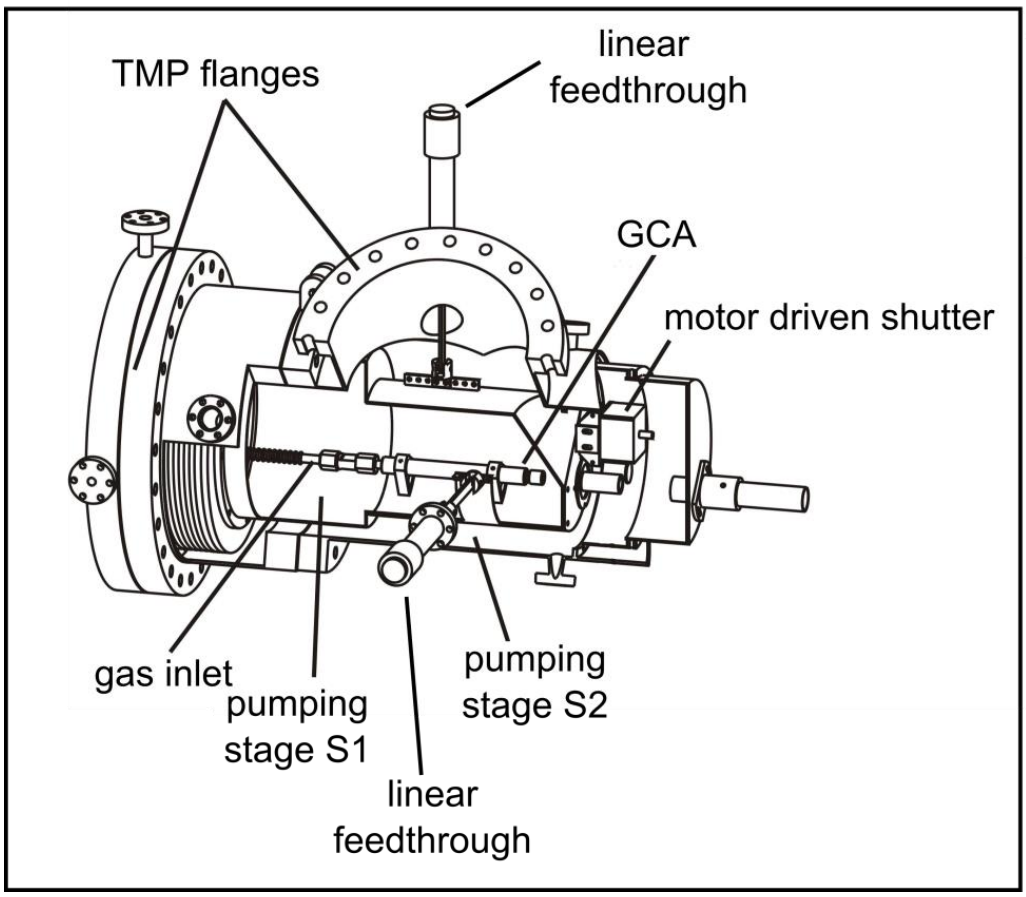

***Figure 3.4**: Schematic cross sectional drawing of the effusive molecular beam source as adapted from Ref.* [4].

A temporally stable flux of educts requires a stable pressure on the high-pressure side of the GCA. The schematics of the gas lines used to supply the molecular beams are shown in **Figure 3.5**. Each molecular beam is connected to a dedicated gas manifold, which can be evacuated by means of a rotary pump. A gas reservoir, whose pressure is measured by capacitance monometers (MKS Baratron 626B, pressure range of 10^{-4} to 1 mbar) is fed by a regulated flow control valves (MKS 248A). APID controller (Type 250, MKS) is used to stabilize the pressure in the gas reservoir by operating the flow control valves. The gas reservoir as well as the high-pressure side of the GCA are pumped using a turbo molecular pump (Turbovac TMP 50, Oerlikon-Leybold).

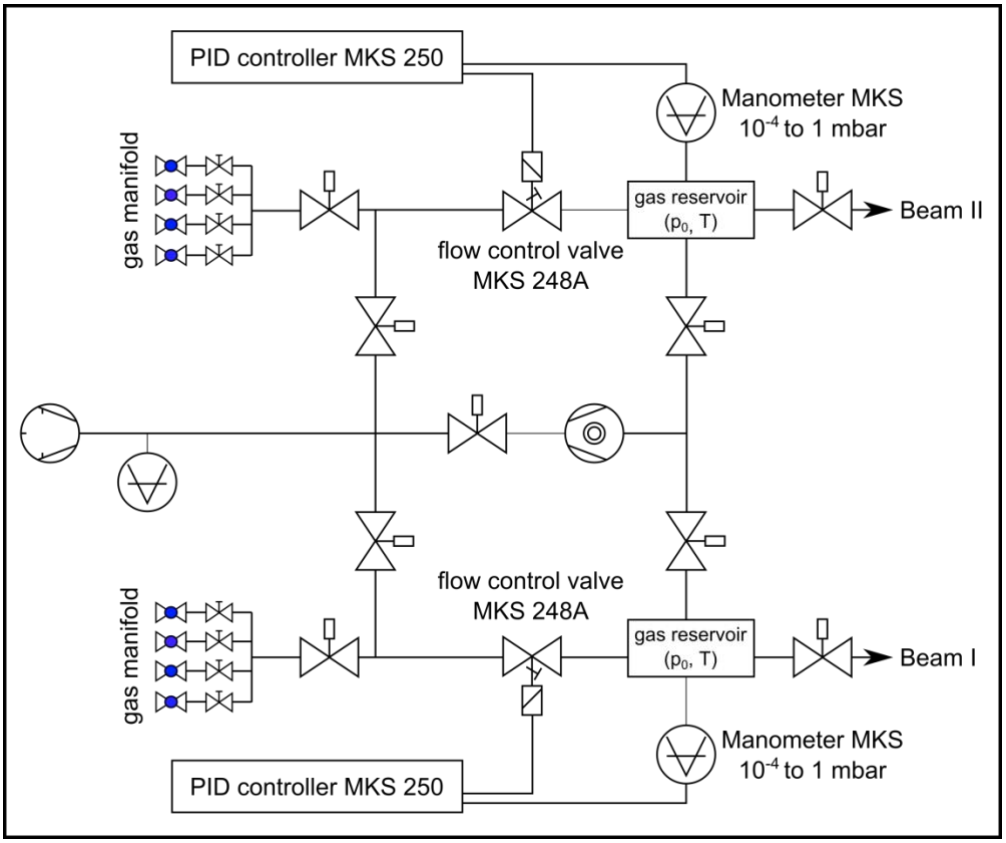

***Figure 3.5**: Gas inlet system of the effusive beams.*

Except for the valves on the gas manifold, all other valves, the set points of the PID controllers as well as all pressures are monitored and operated by a home written Labview program.

3.2.2 Stagnation Flow Monitor

For a characterization of the effusive beams, it is important to determine a spatially resolved map of the flux. To this end a so-called stagnation flow monitor is used. The monitor consists of a tube (16 mm outer diameter), which exhibits a 1 mm wide aperture at the upper end as schematically shown in **Figure 3.6A**. The position of the aperture can be controlled by means of a manipulator in the plane where the sample is located. The atoms coming from effusive beams impinge on the aperture hole and molecules will flow into the tube until the pressure in the tube is equal the local pressure in front of the aperture. Hence, a high precision ion gauge (360 Stabil-Ion, Granville-Phillips) mounted on a DN40CF flange at the end the stagnation flow monitor allows to

determine the local pressure in front of the aperture. **Figure 3.6B** shows the stagnation monitor inside the scattering chamber.

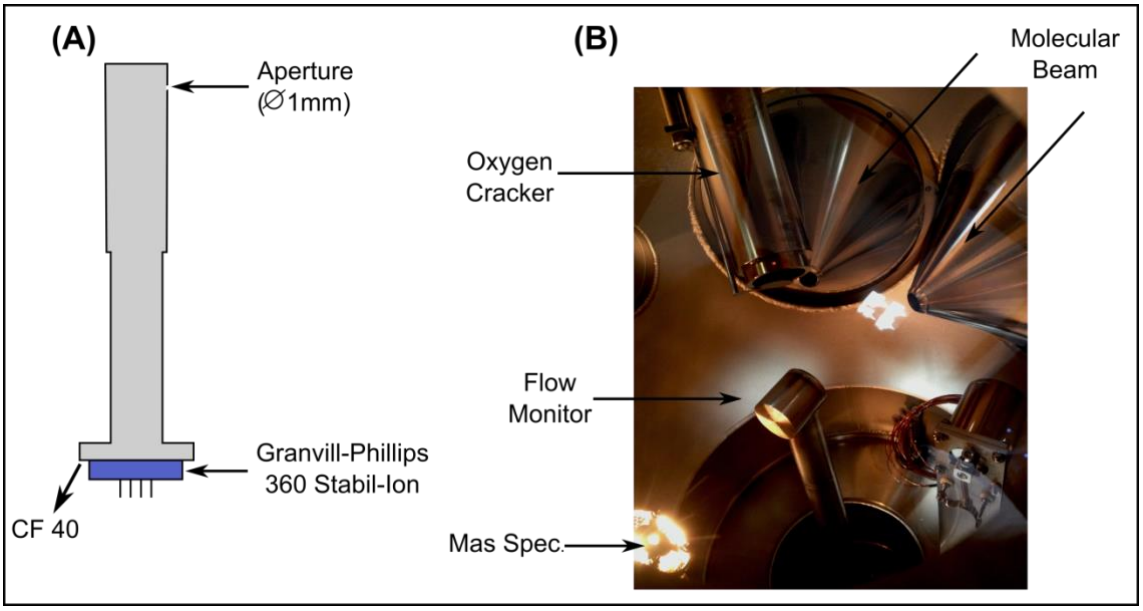

***Figure 3.6**: (**A**) Schematic of the stagnation flow monitor and (**B**) internal part of the scattering chamber.*

According to kinetic gas theory, the flux of molecules *F* at the position of the aperture hole can be determined from the pressure p_0 in front of the aperture using:

$$F = \frac{p_0}{\sqrt{2\pi m k_B T}} \qquad \textbf{10}$$

Where ***m*** is the mass, ***T*** the temperature of the gas and k_B denotes the Boltzmann constant. To ensure a fast equilibrium between the chamber and the tube of the stagnation flow monitor argon (Ar) was used to determine the flux profiles.

3.2.3 Mass Spectrometer – Gas Phase Detection

Gas-phase fragments of reaction educts and products are detected with a quadrupole mass spectrometer (MAX-500HT, Extrel) capable to detect an m/z range of 1–500 amu/e. The spectrometer is equipped with an axial ionizer, a

quadrupole filter with 19 mm Mo rods, and a pulse counting electron multiplier. The spectrometer is mounted out of the line-of-sight of the molecular beams as well as the sample, which ensures that both educts as well as products desorbing from the sample have to scatter with the chamber walls. The latter ensures that the measured intensity is not artificially altered by directional scattering effects.

3.2.4 FT-IR Spectrometer

Infrared reflection-absorption spectroscopy (IRRAS) measurements are performed using a commercial vacuum FT-IR spectrometer (Bruker IFS 66 v/s). The evacuated optics allows to record IR spectra free from interferences with the gas phase. The setup of the optics uses an external detector chamber as indicated in **Figure 3.7**. The scattering chamber is sealed against the IR spectrometer as well as the detector chamber by means of two, Viton-sealed KBr windows (∅ 55 mmx6 mm, Korth Kristalle). The IR spectrometer has been aligned such as to reflect the IR beam at the sample surface being positioned in the scattering chamber such as to optimize the overlap of the two effusive beams. While the IR spectrometer including the mirror chamber responsible for the adaptation to the UHV apparatus is operating at fine vacuum (typically 1 mbar during operation because of gaseous N_2 used to lubricate the movable mirror in the Michelson interferometer), the detector chamber is pumped by a stack of rotary and turbo molecular pump leading to a typical pressure of $1.0 \cdot 10^{-6}$ mbar during operation.

The description of the infrared measurement set up is briefly as follows: The IR radiation from the SiC glowbar is focused on an aperture wheel of various sizes (typically a 1 mm diameter aperture is used) passing through the Michelson interferometer with automatic alignment using a helium-neon (HeNe) laser. A gold-plated parabolic mirror is used to focus the parallel IR beam from the Michelson interferometer onto the sample using a grazing incidence (85°) scattering condition. The size of the beam on the sample position is approximately 1.2 mm in diameter, which is elongated along the scattering direction. The sample is located in one of the focal points of a hyperbolic mirror, which focuses the light from the sample onto the liquid nitrogen cooled mercury-

cadmium-telluride (MCT) detector being located in the other focal point of the mirror. Spectra are typically taken with a spectral resolution of 4 cm^{-1}, 256 scans, 2 as a zero-filling factor. For Fourier transformation a Blackman Harris 3-term apodization function was used and the spectra were phase corrected by means of the power spectrum.

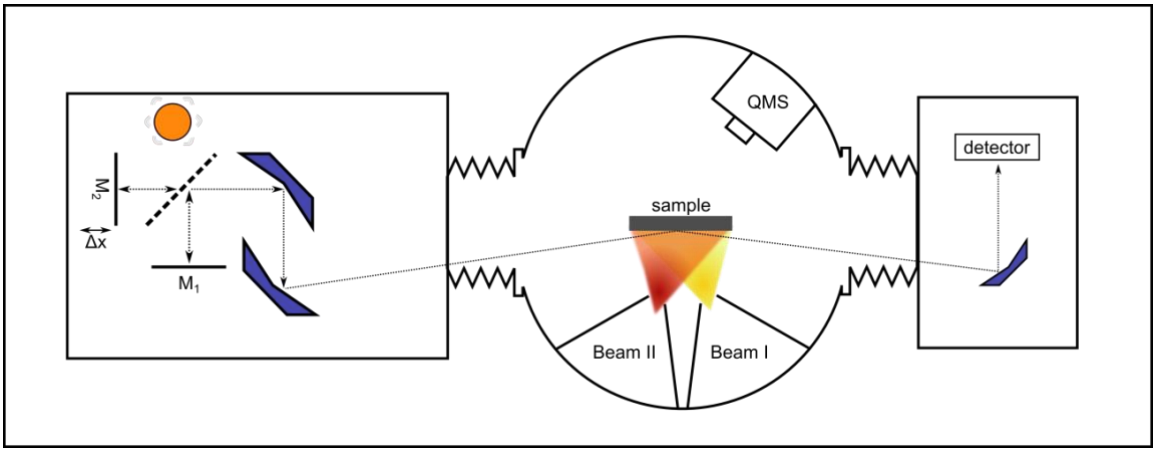

***Figure 3.7**: A schematic representation of the FT-IRAS assembled on the MB apparatus.*

3.2.5 Oxygen Cracker

Oxygen atoms are created by means of a commercial thermal oxygen cracker (Dr. Eberl MBE-Komponenten GmbH). Atomic oxygen is generated by contact of molecular oxygen flowing through a hot Ir tube, which is heated radiatively by a surrounding filament up to 1900 °C. The heater unit is shielded by tantalum foils and surrounded by a water cooled, Ni-plated copper housing in order to minimize a radiative heat transfer into the scattering chamber. **Figure 3.8** shows a sketch of the internal construction of the atomic oxygen source.

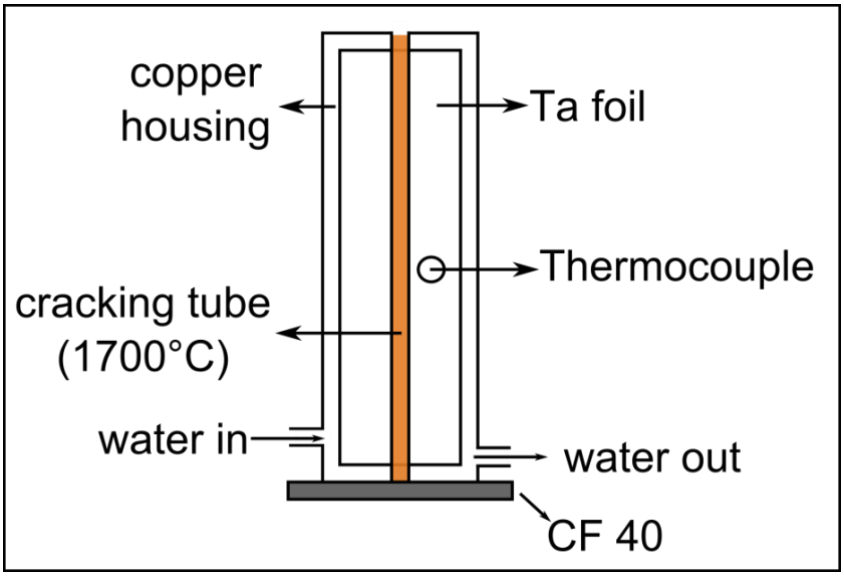

***Figure 3.8**: Illustration of the oxygen cracker cross section.*

3.2.6 The Sample Setup

A schematic of the sample setup is shown in **Figure 3.9**. A Au(332) single crystal (Mateck) of 10mm diameter and1.5 mm thickness was used. The single crystal had slits on the two opposing sides (0.3 mm wide and 1.5 mm deep), which were used to clamp the crystal onto a BN heater (HT–01, Momentive), with a nominal heating power of 80 W. The latter is mounted onto a Mo structure as indicated in **Figure 3.9**. The electrical insulation between the BN heater and Mo-holder is done by alumina bushings. The BN heater is connected at the two opposing sides by Cu wires which are connected to the top of the manipulator. The sample is mounted onto the BN heater by means of spring loaded Mo-clamps, which are connected to the Mo-holder. As the sample has to be electrically decoupled from the ground a sapphire disc is used in between the Mo-holder and Cu block of the ℓ-N_2 reservoir. The latter is a stainless-steel tube, which can be filled from the top of the vertically oriented manipulator, and ends in a Cu block as schematically depicted in **Figure 3.9**. The sample temperature is measured by a thermocouple type K (Omega) mounted in a small pinhole (diameter 0.5 mm, depth 2 mm) drilled into the side face of the single crystal orthogonal to the two slits used for mounting the crystal. The setup allows to heat the sample up to 1200 K and to cool it down to about 100 K. To perform isothermal experiments, the sample temperature is controlled by

a PID controller (3216, Eurotherm). The temperature stability of the isothermal experiments is better than 2 K over the typical length of an experiment (> 1 h).

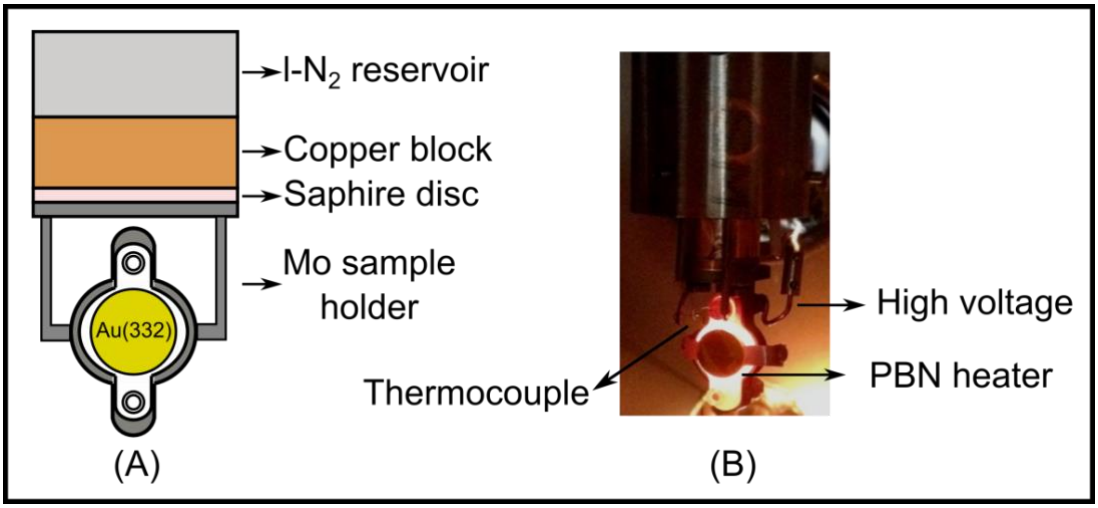

***Figure 3.9**: (**A**) Schematic representation of the sample holder and (**B**) the Au(332) surface at 1000 K during the annealing step.*

4. Calibration and Characterization of the MB Apparatus

4.1 Beam Alignment

The alignment and characterization of the effusive sources is performed using the stagnation flow monitor described in **Chapter 3**. Since pressures measured inside the stagnation flow monitor are a direct measure of the flow per unit area on pinhole no corrections are necessary for the different incidence angles. The scattering plane is chosen to be the xy-plane in the laboratory coordinate systems with x being perpendicular and y parallel to the sample surface (see **Figure 4.1**). To allow for a reproducible positioning of the sample or the stagnation flow monitor in the scattering chamber, two cameras (DMK 23G445, The Image Source) are stably mounted on CF35 flanges equipped with viewports. Camera 1 is oriented along the x-direction and allows adjusting the y- and z-position of the sample. Camera 2 is oriented in the yz plane and allows for a proper positioning in the x-direction (see **Figure 4.1**). The first important task is to find the position within the chamber, which maximizes the overlap between the two effusive beam sources.

To this end the stagnation flow monitor was positioned in the nominal centre of the chamber and flux profiles as shown in **Figure 4.2** were measured for both beams. As schematically shown on the right-hand side of Figure 4.1, the two beam profiles did not overlap initially. As the scattering geometry of the two beams is known it is possible to calculate the position in the scattering plane, which optimizes the overlap of the two beams. To this end the y-components of the beam profile centres indicated by the light blue areas in **Figure 4.1** were mapped onto the scattering plane, which allows determining the x-y coordinates of the position with optimal overlap between the two effusive beams. After that both beam profiles were measured again with the stagnation flow monitor positioned at the optimized x-component to ensure that the procedure resulted in the correct position.

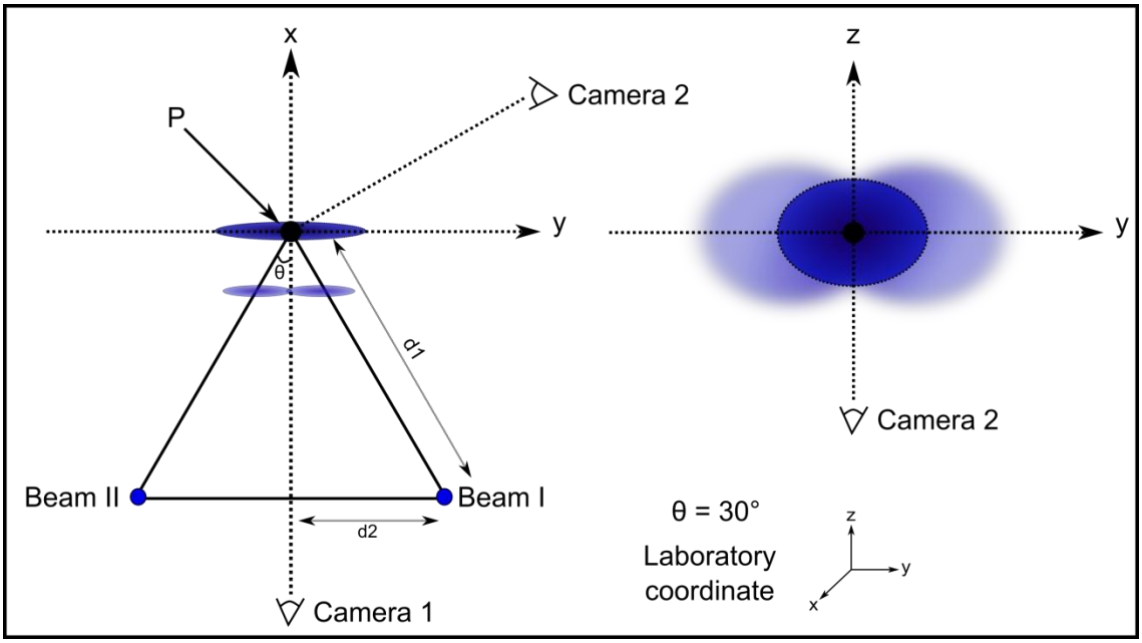

***Figure 4.1**: Schematic of the geometrical arrangement for determining the crossing point of the effusive beams along the xy plane (left) and the zy plane (right).*

An important ingredient for a proper alignment using the abovementioned procedure was the ability to determine the centre of the effusive beam profile. This requires a correct alignment of the glass capillary array (GCA) with respect to the two apertures. To this end the position of the GCA and the first aperture, which are mounted together was adjusted with respect to the second aperture mounted fixed inside the UHV chamber. The second aperture defines the size of the beam. By adjusting the linear feedthroughs, it is possible to position the maximum of the molecular flux in the centre of the ellipse defined by the second aperture. This interactive alignment is performed individually for each effusive beam. **Figure 4.2** shows a beam profile across the z- and y-axis of one of the effusive beams using an inlet pressure 0.05 mbar Ar. In addition to the pressures measured by the stagnation flow monitor the size of the sample is indicated by the black circle drawn (diameter of 10 mm) into the diagram. The pressure varies by about 20 % over the entire crystal surface, which shows a homogeneous flux over the entire surface. With respect to the single collision conditions to be achieved with this setup, it is important to note that the background pressure in the scattering chamber is $1.9 \cdot 10^{-8}$ mbar, which corresponds to a peaking factor of 23 for these beams.

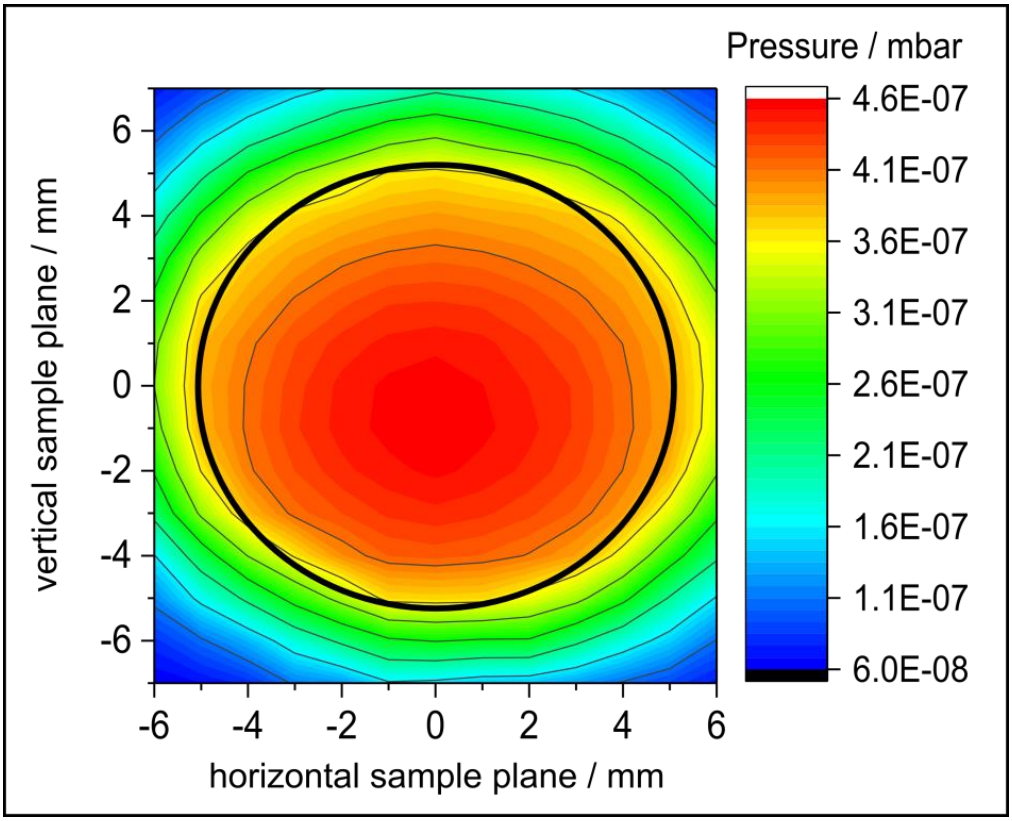

***Figure 4.2**: Beam profile for an inlet pressure of 0.05 mbar of Ar at the sample position (black circle).*

Finally, the IR spectrometer is adjusted for the sample position determined using the procedure described above by optimizing the orientation of the corresponding mirrors (see **Section 3.2.4**).

Figure 4.3 shows the dependency of the beam intensity on the backing pressure of argon. Two ranges can be distinguished:

(i) For inlet pressures below about 0.6 mbar – the flux of molecules emitted from the effusive beam is proportional to the inlet pressure. The calibration curve presented in **Figure 4.3** allows for a direct correlation between these quantities being of utmost importance for quantitative evaluation of kinetic experiment.

(ii) At pressures above 0.6 mbar marked deviations from the linear behavior are observed. The flattening of the curve at higher pressures is due to the fact that the Knudsen number is no longer much larger than one. This results in a complex flow behavior within the channels of the CGA, which leads to scattering losses.

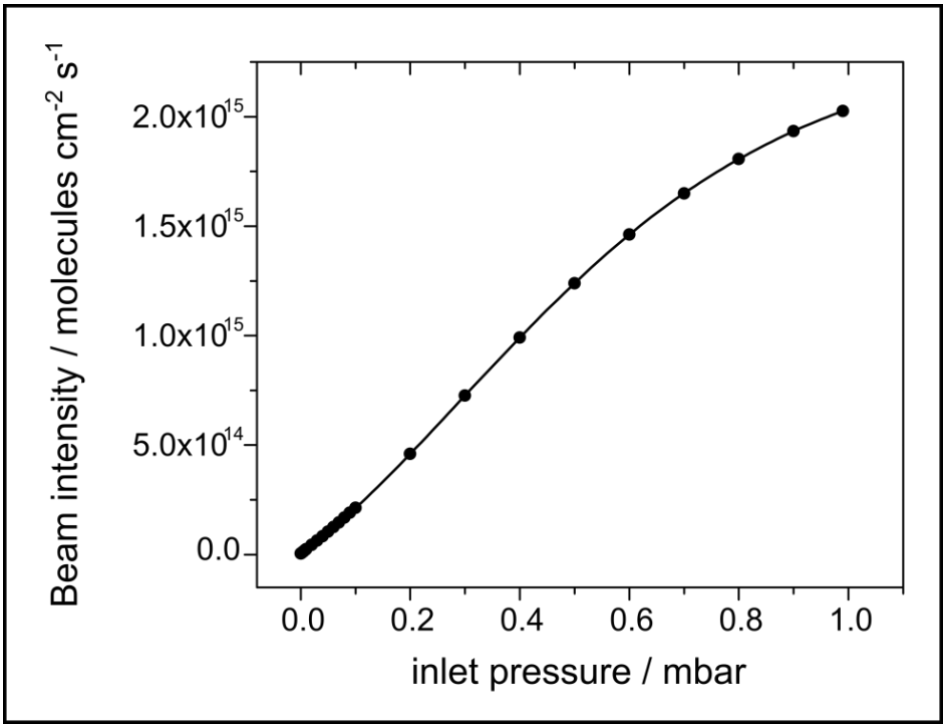

***Figure 4.3**: Beam intensity as a function of Ar backing pressure.*

4.2 Oxygen Beam Calibration

Dissociation of O_2 starts at temperatures of the Ir tube of about 1500°C.The cracking efficiency depends on both the temperature of the tube and the gas flux through the tube. As the atomic beam source (AOB), which is mounted at distance of 100 mm from the Au(332) surface, is supposed to be used as a well-defined source of oxygen atoms, it is important to control both the temperature of the tube as well as the gas flow. For an effusive flow the latter can be controlled by the inlet pressure of the Ir tube. To this end a feedback-controlled system along the lines used for the effusive beams (see **Chapter 3**) using a flow control valve (MKS 248 A, maximum flow of 10 sccm nitrogen), a capacitance manometer (MKS Baratron 626C), and pressure controller (Type 250, MKS) was installed. Before being admitted to the chamber, the gas line is thoroughly purged to remove any residual gas contamination. The oxygen is introduced through a leak valve and the operation temperature of the cracker is 1700°C while watching the chamber background pressure, which is chosen to be $1.0 \cdot 10^{-8}$ and $5.0 \cdot 10^{-8}$ mbar.

The flux density of O-atom is a function of both temperature and flow through the tube. However, according to the data sheet provided by the manufacturer, at low gas flow regime, which is used in this current thesis, the grade of dissociation demonstrated a linear dependency of the gas flow through the cracking tube for constant operational temperatures[75,76]. The oxygen pressures are chosen to be $3.2 \cdot 10^{-8}$ or $1.4 \cdot 10^{-7}$ mbar the corresponding flux can be estimated to be 0.0003 and 0.0016 sccm, respectively (for a detailed calculation please see in **Appendix A)**. For a temperature of the Ir tube of 1700 °C these fluxes correspond to cracking probability of about 13%. In turn, the O-atom flux corresponding to these oxygen pressures are $1.4 \cdot 10^{12}$ atoms $cm^{-2}s^{-1}$ (0.0003 sccm) and $7.3 \cdot 10^{12}$ atoms $cm^{-2}s^{-1}$ (0.0016 sccm).

The coverages of atomic oxygen on the Au(332) surface was estimated from Auger spectroscopy. Unfortunately no ordered atomic oxygen overlayer has been observed on Au(332) surface during this measurements, so coverages could not be correlated with LEED. Therefore, the coverage of oxygen is monitored the ratio of the dN(E)/dE peak heights of the Auger signal of O and Au. The Auger signal is expected around 500 eV and the Au signal at about 69 eV[77]. However, the oxygen signal was observed at about 469 eV. A possible reason for this energy difference can be due to linearity of the energy scale calibration. **Figure 4.2** shows the peak heights O/Au ratio as a function of oxygen exposure time in seconds and the corresponding nominal O-atom dose. The plot in **Figure 4.2** shows a noticeable reduction of the slope with increasing coverage for both curves. In a simple layer by layer growth mode such kinks in the curve are associated with the completion of one monolayer. Here, 1 ML of oxygen is defined as $1.39 \cdot 10^{15}$ atoms cm^{-2} and refers to a single atomic layer of close-packed ideal Au(111) surface. For the low oxygen pressure and the correspondence oxygen flux of $1.4 \cdot 10^{12}$ atoms $cm^{-2}s^{-1}$, the time necessary to complete 1 ML of oxygen by assuming layer by layer growth conditions is estimated to be at about 632 s; however, the saturation point is at about 140 ± 5 s, which is 86% less than the estimated time. Now, for the high oxygen pressure with oxygen flux of $7.3 \cdot 10^{12}$ atoms $cm^{-2}s^{-1}$, the estimated time for 1 ML of O is at about 200 s, however the O/Au ratio plot underestimates the saturation point at about 60 ± 5 s (see **Figure 4.2B**). Obvious uncertainties in the above calibration

procedure is expected, e.g. Auger line shape changes, co-adsorbates, different growth mode etc., probably force error bars for the estimated saturated times to complete 1 ML of O on Au(332) to be ± 5 s. The difference to the estimated time can be attributed to intensity changes (due to scattering) of either the oxygen or gold signals that results from the disordering of the Au(332) substrate, or subsurface oxygen layer to form an oxide phase.

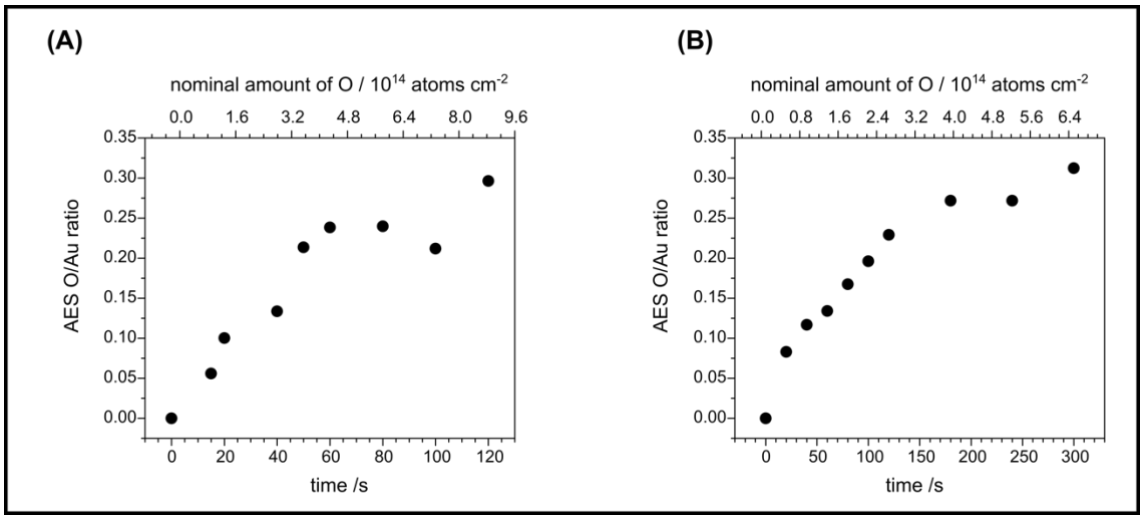

***Figure 4.2**: Peak-to-peak height ratio of O(469 eV)/Au(69eV) in AES as a function of oxygen exposure time. Oxygen pressure on Au(332) surface is (**A**) 1.4•10^{-7} mbar and (**B**) 3.2•10^{-8} mbar. The operation temperature of the cracker is 1700 °C. $T_{surface}$ = 100 K.*

5 The Sample

In the present work, a Au(332) surface is investigated and serves as a model to elucidate the role of low-coordinated sites for the reactivity of Au surfaces. The atomic arrangement of the 332 face of Au is schematically shown in **Figure 5.1** and consists of (111) oriented terraces separated by closed packed steps running along an [110] equivalent direction. Such an arrangement is typically denoted by [n($h_wk_wl_w$) x (hkl)] where n indicates the number of atoms that constitute the terrace with orientation ($h_wk_wl_w$) the step surface characterized by hkl. For the (332) surface this results in [6(111) x (111)].

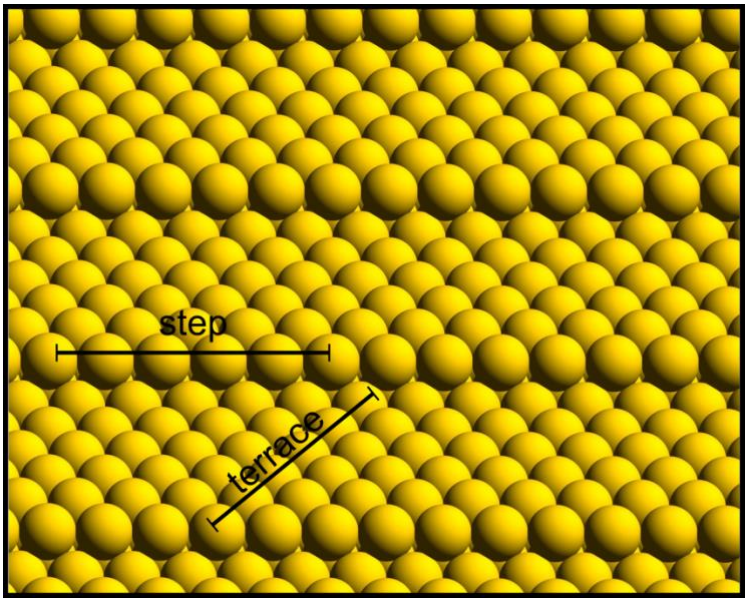

***Figure 5.1**: Front view of the clean Au(332) slab.*

As a first step prior to the investigation of chemical reactions on Au(332), it is important to clean and characterize the surface. The substrate is cleaned by repetitive cycles of sputtering with argon ions (P_{Ar+} = 2 x 10^{-5} mbar) at 1keV using a sputtering current of 7 µA for 15 minutes followed by annealing to1000 K in UHV for 10 minutes. The properties of the surface are determined by means of AES and LEED as shown in **Figure 5.2**.

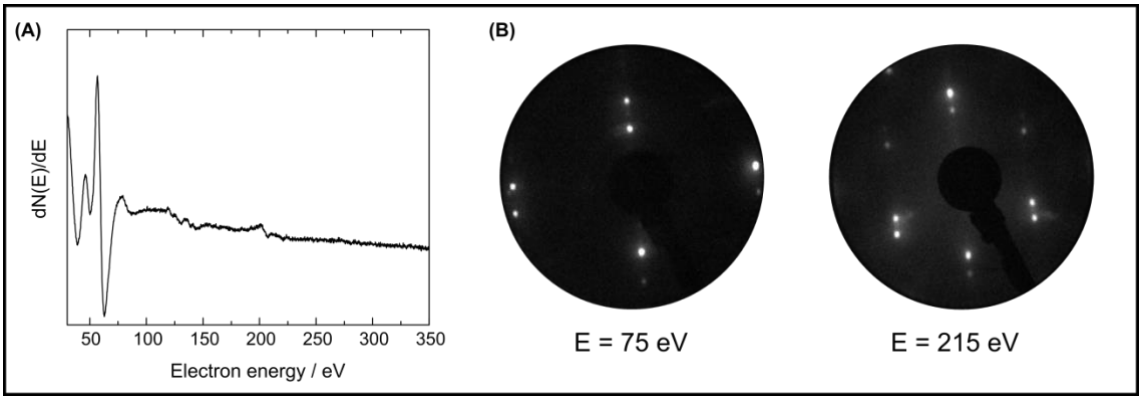

***Figure 5.2**: (**A**) Auger electron spectra and (**B**) LEED pattern of clean Au(332).*

The observed Auger signals in **Figure 5.2A** can be assigned to Au (69, 135, 211 eV). No other signals could be found within the sensitivity of Auger spectroscopy indicating a clean Au surface is successfully obtained. **Figure 5.2B** shows the LEED pattern of a clean Au(332) surface. The pattern reflects the three–fold symmetry of the (111) face, as indicated in the LEED pattern at 215 eV. In addition to that, secondary spots are also observed, which are regularly spaced from the main spots due to the steps all over the surface. Spot splitting characterize the periodic spacing of steps separating the vicinal surfaces[78–80]. The split diffraction spots collapse into singlet (data not shown) as the electron beam energy is varied due to the fact that the adjacent terraces exhibit destructive and constructive interference as the beam energy is varied. This is an indication of ordered arrangement of atomic steps[80]. Additionally, there is no sign of reconstruction and the background is rather small. These observations are in line with results reported in the literature[81].

6. IRAS of ^{13}CO on Au(332)

The vibrational properties of carbon monoxide have been investigated extensively on a variety of different single crystal surfaces[68,82–84]. Apart from vibrational spectroscopy many other techniques have been used to investigate the properties of CO on various metal surfaces, hence it can be considered the best understood adsorption system on metal surfaces. The C-O stretching frequency depends on the chemical environment, i.e. the coordination to the metal as well as the chemical nature of the adsorption site. The latter properties render it a frequently used probe molecule. The stretching frequency of ^{12}CO in condensed phase is found at 2143 cm^{-1}[85]. IR experiments were done on a variety of single and polycrystalline Au surfaces showing a ^{12}CO stretching frequency between 2124 and 2070 cm^{-1} depending on the surface orientation as well as surface coverage. ^{12}CO stretching frequencies are compared for different Au single crystal surfaces based on literature data[86–90] and summarized in **Figure 6.1**.

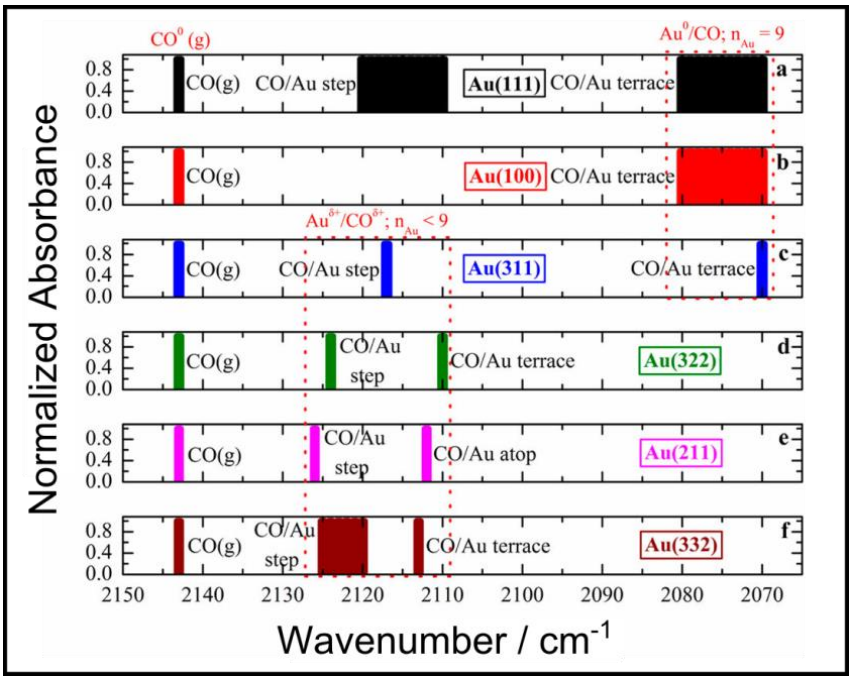

***Figure 6.1**: Stretching frequencies for CO adsorbed on different Au single crystal surface, which exhibit adsorption sites with different Au coordination number. Reprinted and adapted with permission from Wang et al.[5]. Copyright 2016. American Chemical Society.*

For a coverage series ^{12}CO on stepped Au(332) taken at low temperature, Hollins and co-workers[91] have observed a band starting to be seen at about 2125 cm^{-1}, which shifts to lower wavenumber with increasing coverage. Additionally, the IR spectra show evidence of more than one species as deduced from the presence of shoulders appearing on both the high and low wavenumber sides of the main band even at low CO coverages. A similar behaviour with slightly blue shifted ν_{CO} stretching frequencies was observed for the Au(211) surface investigated by Koel and co-workers[86].

The binding energy of CO on gold was probed by TPD on various Au surfaces exhibiting low coordinated sites, including Au(110)[92], Au(332)[91], Au(310)[93], Au(321)[93] as well as supported Au particles[33,94–96]. Furthermore, Bäumer and co-workers[97] also investigated the influence of low–coordinated Au atoms using a roughened Au(111) surface. In all these TPD experiments two desorption states were identified above 100 K, one at about 120-145 K and other 170-185 K, however, only one infrared peak at around 2120 cm^{-1} was observed. In contrast, TPD spectra of freshly prepared and annealed Au(111) surfaces do not show CO desorption within this temperature regime at all. Therefore, they conclude that both desorption peaks belong to CO on low–coordinated gold atoms at steps and kinks. Moreover, the adsorption of CO on np-Au was investigated by Röhe *et al*.[98]. The TPD spectra of CO obtained after exposing np-Au to 100 L CO at 113 K reveal a more complex behaviour in which CO desorption is observed in a broad temperature range of 130-220 K. So far CO desorption above 200 K has only been observed for sputtered Au(110)-(1 x 2)[92] and for Au(321)[93]. However, in both cases, the corresponding TPD signals are rather weak representing minority sites of the surface.

In this chapter, results from IR spectroscopy will be reported. In the first section, the adsorption of ^{13}CO on the bare Au(332) surface will be investigated at low temperature as well as at temperatures above a stable adsorption under UHV condition. The second section is followed by a discussion of CO adsorption on the oxygen pre-covered surface under isothermal and isobaric conditions.

6.1 ^{13}CO Adsorption on Au(332)

As a starting point of the discussion ^{13}CO is adsorbed on the Au(332) surface at 100 K using a constant CO pressure of $1.9 \cdot 10^{-8}$ mbar on the surface as provided by the molecular beam. **Figure 6.2** shows a series of spectra taken during ^{13}CO exposure. These spectra were referenced against a background spectrum taken prior to opening the CO beam.

At low coverage two lines can be discerned in the spectral region below 2080 cm^{-1}, which is related to vibrations of the ^{13}CO isotopomer. One is observed at 2075 cm^{-1} while a shoulder can be discerned at 2065 cm^{-1}. With increasing exposure, the peak at 2075 cm^{-1} increases in intensity and shifts towards lower wavenumbers. Concomitantly, the relative intensity of the low energy shoulder increases, however, above 9 L the two spectral components are no longer discernible. With increasing exposure, the high energy peak shifts to lower wavenumbers resulting in a decrease of the overall line width. Beyond about 15 L (1 L = 10^{-6} Torr s) no significant change in peak position (2065 cm^{-1}) and line width can be observed.

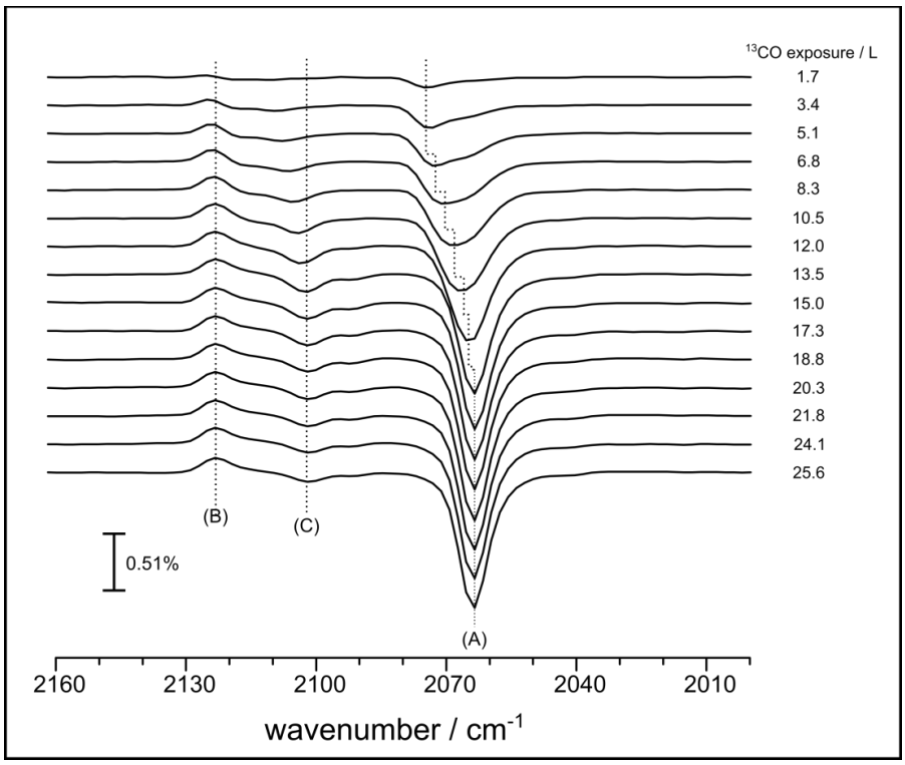

***Figure 6.2**: IR spectra of ^{13}CO adsorption on Au(332) measured at 100 K. Three spectral components can be identified at the final absorption position (**A**) 2065 cm^{-1}, (**B**) 2123 cm^{-1}. In addition an emissive peak is found at (**C**) 2127cm^{-1}. Each spectrum is labelled with the exposure in units of Langmuir (1 L = 10^{-6}Torr s).*

The presence of at least two IR components on Au(332) observed at low coverage, suggests that the structure of the surface may be more complicated than the idealised description of uniform terraces separated by monatomic steps discussed in **Chapter 5**. While the clean Au(111) shows a well-known herringbone reconstruction[99], this is not observed for the small (111) terraces of the Au(332) surface. However, Prieto *et al*.[100] have shown by STM that steps on Au(332) surface can exhibit a significant kink density. A surface containing a high proportion of kinks as well as the expected step sites might reasonably be expected to give rise to the two components that are observed. To this end, one could assign these two vibrational bands observed to CO adsorbed at step and kink sites, respectively.

The integrated IR intensity of the ^{13}CO related signal shows an almost perfectly linear increase with CO dose up to 8L (**Figure 6.3**). In between 8 and 15 L the slope of the intensity curve decreases slightly to level off for exposures above about 15 L. The result suggests that the sticking probability of CO is rather constant at low exposure range, however, dropping fast close to the saturation coverage under these conditions.

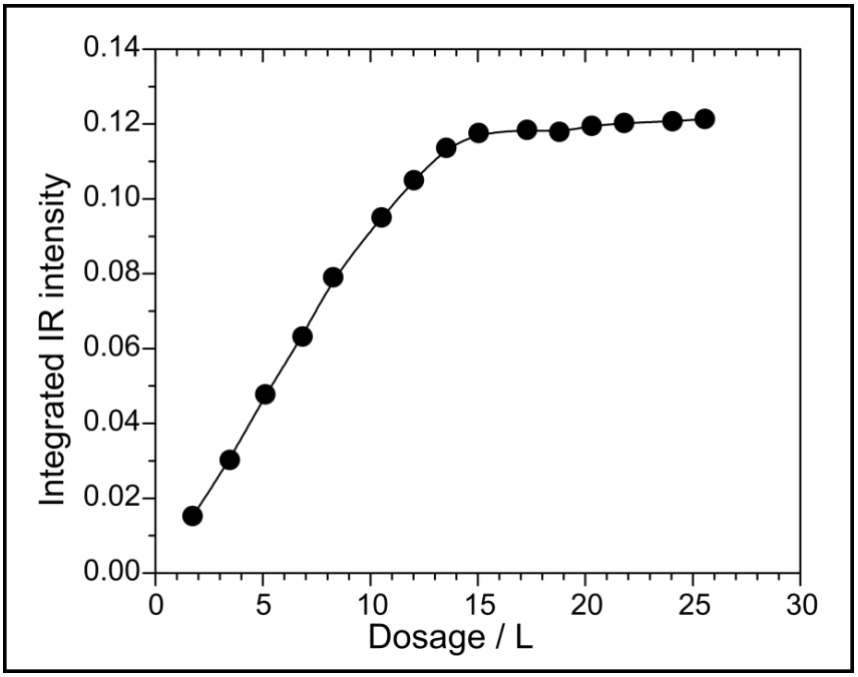

Figure 6.3: *Integrated IR intensity of ^{13}CO peak around2075 - 2065 cm^{-1} as a function of CO dosage.*

Comparing the two signals observed at low coverage, a clear difference in terms of spectral shift is observed. While the line initially observed at 2075 cm^{-1}

shift down by about 10 cm^{-1} with increasing coverage, the shift of the shoulder at 2065 cm^{-1} is very small. The origin of the different behaviour in the total shift can be gathered from isotope mixture experiments.

In this set of experiments, signals corresponding to adsorbed ^{12}CO are observed between 2125 and 2100 cm^{-1}, which originate from unintentionally adsorbed CO from the residual gas of the chamber onto the surface prior to adsorption of the ^{13}CO. A close up of this spectral range is shown in **Figure 6.4**. At high coverage (bold red line) the spectrum consists of four features. Two signals at 2102 and 2092 cm^{-1} are observed, which have the same sign as the IR lines of ^{13}CO discussed above. In addition, a signal at 2123 cm^{-1} together with a shoulder at about 2113 $cm^{-1}$are found, which have an opposite sign.

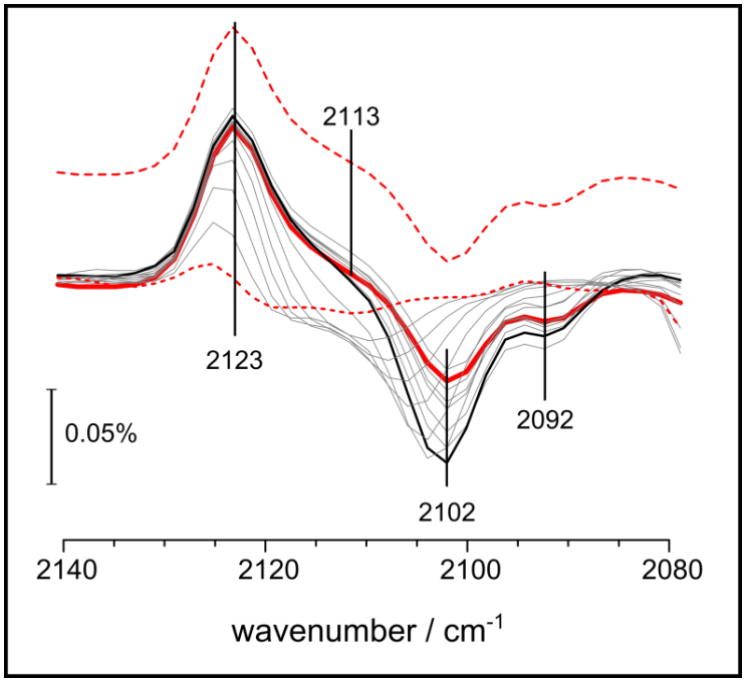

***Figure 6.4**: A close up of the ^{12}CO spectra range. At high coverage (bold- and dashed red line) the spectrum consists of four features at 2123, 2113, 2102 and 2092 cm^{-1} are observed. The dashed red spectrum at the top is the invert and scaled of the ^{13}CO coverage series presented in **Figure 6.2**.*

At first glance this result is unexpected as the “positive” peaks seem to indicate a loss of CO species. Such a result is the typical observation in case the background spectrum contains signals, which are changing in the course of the experiment. To indicate the spectral similarity between this small amount of ^{12}CO with results from the ^{13}CO results discussed above, the first signal of the ^{13}CO coverage series presented in **Figure 6.2** was taken and shifted to overlap with the ^{12}CO signal (dashed red spectrum at the top). The shift needed to be 1

cm^{-1} larger than calculated based on the frequency shift expected because of the change in reduced mass. In addition, the shoulder at the low energy side is more pronounced for the ^{13}CO spectrum than it is for the ^{12}CO signal at the highest coverage. The latter suggests that a larger fraction of the first ^{13}CO molecules adsorbed on the surface have a higher tendency to occupy sites with lower frequency than the pre-adsorbed ^{12}CO. This is in line with the coverage dependent spectra showing an increase of the intensity ratio of the low frequency component as compared to the high frequency one discussed above. The small shift of the resonance positions at slightly higher coverage indicates that the sum of chemical and dipolar shifts which may act on the ^{13}CO molecules is small at this coverage.

While the two positive peaks report on the properties of the ^{12}CO molecules in the absence of ^{13}CO, the lines at 2102 and 2092 cm^{-1} observed at maximal ^{13}CO coverage available under these conditions report on the stretching frequency of these ^{12}CO molecules in the presence of ^{13}CO. As seen from the coverage series presented above, the absolute amount of ^{12}CO is small as compared to the total coverage of CO. Quantification is, however, difficult based the IR data, because it would require assuming a linear correlation between IR intensity and CO coverage. The results discussed above show that at least at higher coverage this linear correlation might not hold. As shown in the past, the frequency difference of ^{12}CO and ^{13}CO is large enough to ensure that the shift of the resonance position due to coupling can be neglected[84]. Therefore, the shift observed between the two high energy vibrations with positive sign and the two signals with negative sign is due to the so-called chemical shift induced by ^{13}CO molecules adjacent to the ^{12}CO molecules and is found to be 21 cm^{-1} for both components.

The chemical shift can be compared to the frequency shift between the ^{12}CO and the corresponding ^{13}CO line. For the line observed at 2102 cm^{-1} a shift of 39 cm^{-1} is found, while this shift is 10 cm^{-1} smaller for the line at 2092 cm^{-1}. These differences are smaller than expected based on the differences in reduced mass. This is in line with expectations as the ^{13}CO molecules are not only shifted by the chemical shift, which acts on both isotopomers alike, but furthermore by dipolar coupling. This readily leads to a dipolar shift of the line at 2102 cm^{-1} by 8 cm^{-1}, while the one at 2092 cm^{-1} shows a dipolar shift of 18 cm^{-1}.

Looking at the coverage dependence in **Figure 6.2** of both the ^{12}CO as well as the ^{13}CO lines corresponding to the signal at 2123 cm^{-1} it is possible to deduce the chemical shift as well as the dipolar component as a function of coverage for the high frequency component. One should, however, bear in mind that the position of the ^{12}CO signal shifting to the red may be slightly obscured by the superposition with the underlying spectrum of the background. This may result in a slight shift to lower wavenumbers, however, no attempts were made to correct for this effect. **Figure 6.5** shows the contribution of the two effects on coverage using the spectrum of lowest ^{13}CO coverage as a reference. Even for low coverage both the chemical as well as the dipolar contribution are sizable. With increasing coverage, the chemical shift increases to -22 cm^{-1} at about 15 L, while the dipolar contribution remains almost constant (~11 cm^{-1}). This is in line with observations for supported Au particles, which have shown a rapid increase of the dipolar contribution already at very small coverage and a constant contribution for most of the coverage range[89]. As the dipolar coupling is already sizable at rather low coverage it suggests that the ^{12}CO molecules occupy adsorption sites that even at low coverage allow for dipolar coupling, which suggest a close spatial proximity.

The negative chemical shift observed above, would be qualitative explained in terms of bonding considerations. It is believed that back-donation of electrons into the $2\pi^*$ orbital of CO molecule is relatively unimportant for CO bound to Au, as deduced from the small red shift of CO stretching frequency compared to the gas phase value. Hence, bonding of CO is dominated by the 5σ orbital, which donates electrons to the metal and which is weakly antibonding with regard to the C–O bond[63]. As soon as the coverage raises the increased number of CO molecules donating charge tends to increase the amount of charge on the Au and consequently the C–O stretch frequency will decrease, leading to the negative chemical shift. A similar negative chemical shift has also been observed for CO on Cu(111)[101] and Cu(110)[69].

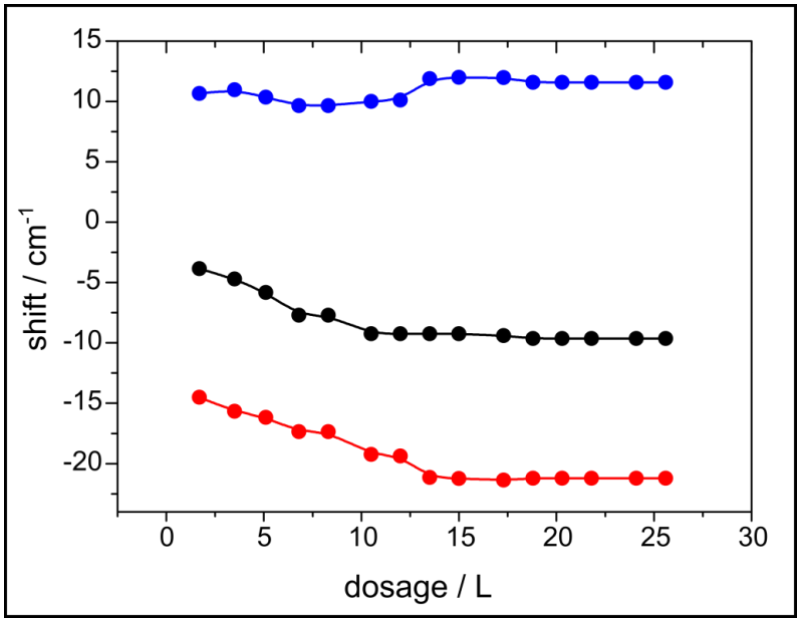

***Figure 6.5**: The separation of the experimentally observed total shift (black) into a chemical (red), dipole (blue) shifts contribution shown as a function of coverage.*

A typical temperature series of IR spectra of ^{13}CO taken under isobaric conditions (p(CO) = $2.4 \cdot 10^{-6}$ mbar) is shown in **Figure 6.6**. The isothermal IR spectra are acquired in steps of 5 K, starting at 235K, and each spectrum is measured using the same experimental conditions as described in **Chapter 3, Section 3.2.4**.

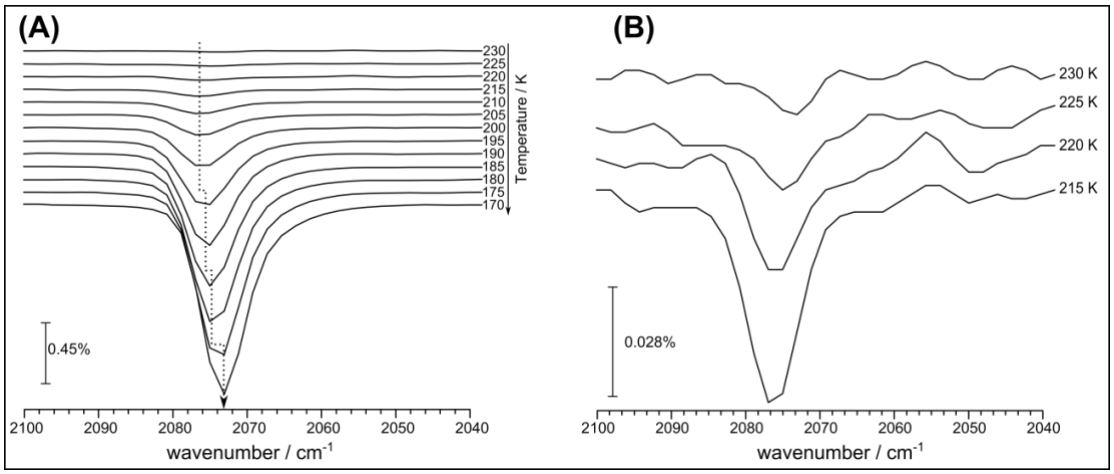

***Figure 6.6**: (**A**) ^{13}CO adsorption as a function of temperature and (**B**) temperature threshold of ^{13}CO adsorption on Au(332) under the experimental conditions presented above.*

These results reveal a single adsorption band of ^{13}CO on Au(332). With decreasing temperature, the line first shifts slightly to the blue from 225 K to 215

K and subsequently to the red reaching a value of 2075 cm^{-1} at 170 K. At the latter temperature the IR intensity is found to be very similar (94 %) to the one observed for saturation coverage at 100 K. While the red-shift is in-line with the low-temperature series and also with the observations made by Ruggiero and Hollins[102] concerning the peak shift with increasing, it is important to mention that the signal position under the isobaric conditions at 170 K is shifted by 10 cm^{-1} to the blue as compared to the low temperature experiment. As the intensity is almost the same one can exclude large changes of the total number of adsorbed molecules. To this end it is interesting to note that the signal of the temperature series shifts significantly to lower wavenumbers when cooling below 180 K. The latter temperature is the one above which no stable CO adsorption was observed under UHV conditions. While the IR result obtained at low temperature was explained by a stable CO adsorption at steps and kinks of the surface, at temperatures above 180 K there is no stable adsorption of CO on the surface. Hence the CO molecules observed by IR above 180 K are only transiently bound to the Au(332) surface and the CO phase on the surface is in dynamic equilibrium with the gas phase provided by the molecular beams. From the difference in the stretching frequency it is concluded that the molecules in this dynamic CO phase occupy on average different adsorption sites than at low temperature.

6.2 ^{13}CO Adsorption on O/Au(332)

To elucidate the nature of CO IR bands observed *in-situ* during CO oxidation, infrared spectra of ^{13}CO were taken on an oxygen pre-covered Au(332) surface and displayed in **Figure 6.7**. The Au(332) surface is first pre-covered with atomic oxygen at 200 K for 120 s, which corresponds to a nominal O-atom dose of $1.7 \cdot 10^{14}$ atoms• cm^{-2} ($p(O_2) = 3.2 \cdot 10^{-8}$ mbar and $T_{cracker}$ = 1973 K), followed by annealing the O/Au(332) surface at 250 K before opening the CO beam. The IR spectra were taken at different surface temperatures under isobaric conditions, $p(^{13}CO) = 2.4 \cdot 10^{-6}$ mbar.

On the oxidised Au(332) surface the first lines are observed at 240 K. The spectrum exhibits a doubled band with components at about 2100 and

2092 cm^{-1}. Initially the intensity of the band at 2100 cm^{-1} is larger than at 2092 cm^{-1}. With lowering the temperature, the low energy vibration gains relative intensity to give an almost symmetric doublet at about 215 K. Finally, an intensity inversion is observed in which the band at 2092 $cm^{-1}$is larger than the one at 2100 cm^{-1}. Moreover, as a function of temperature, the stretching frequency at 2092 cm^{-1} shifts towards lower wavenumber and is found at 2086 cm^{-1} ($\Delta\tilde{\nu} \approx 6\ cm^{-1}$) at 175 K. As the total coverage increases with decreasing temperature, the presence of a shift indicates some interactions between the CO molecules on the surface (see **Figure 6.7B**). A third feature centred at about 2073 cm^{-1} appears at 220 K. Although invariably present at saturation, this feature is always extremely weak (< 4% of the intensity of the main band).

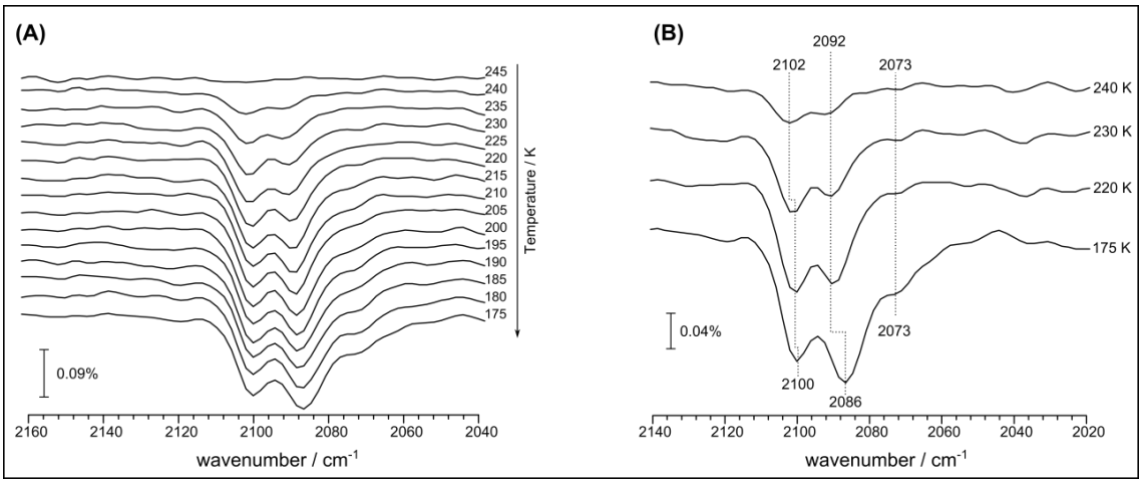

***Figure 6.7**: (**A**) ^{13}CO adsorption on O/Au(332) as a function of temperature and (**B**) temperature evolution of different adsorption of ^{13}CO species on O/Au(332).All spectra are references to a spectrum of the O/Au(332) surface at 250 K.*

Differences in the IR spectrum are observed as compared to CO on the bare surface presented previously. The total coverage at 175 K on the O/Au(332) surface is about 15% of the saturation coverage observed on the clean Au(332) surface. While the two lines at 2100 and 2092 cm^{-1} were not observed on the bare Au surface, the small line at about 2073 cm^{-1}observed below 220 K is in the range of the^{13}CO signal observed on the clean Au(332). The latter observation suggests that a small fraction of the surface steps was not modified by the oxygen atoms (see **Figure 6.7B**). It should, however, be mentioned here, that the CO signal on the bare surface shifts with decreasing

temperature, while the position of the one observed on the oxygen covered surface is almost constant with temperature. In addition, its position is shifted to the blue as compared to the bare surface, which indicates that the corresponding sites are not identical to those populated on the bare surface.

As mentioned previously, CO is observed on the oxygen pre-covered surface below 240 K, as shown in **Figure 6.7**, which is ~20K higher as compared to the clean surface presented above and clearly suggests that CO binds more strongly to these sites on the O/Au(332) surface than to any site on the clean one. An increase of the CO binding energy upon “oxidation” of the metal is not typically observed for late transition metals. More regularly, the CO binding energy decreases for oxygen covered surfaces such as Pd, Co or Fe[103,104]. On the other hand a blue shift of the CO stretching frequency is well in line with observations on other transition metal surfaces[105,106]. This is in line with chemical intuition rendering oxygen an electron withdrawing ligand. In turn CO binds to a metal cation with surrounding oxygen anions. The reduction of charge density on the metal together with the “hard-wall” effect induced by the Pauli repulsion of the oxygen anions allows to understand this blue shift[107]. In case of oxygen atoms adsorbed at kink sites of a Au(321) surface Moskaleva and co-workers have found CO adsorption sites with a binding energy higher than that of the CO on the clean Au surface[108]. CO adsorbed to these sites were calculated to show a blue shift with respect to the CO stretching frequency of CO on the bare Au surface. While these aspects are well in line with the experimental observations, theory also predicts that the barrier for the oxidation of CO by these oxygen sites are rather low, which renders them unstable under the conditions used here. It is, however, clear that the oxygen coverage present under these conditions is significant, which renders the possibility to have individual oxygen atom adsorbed at the step edges small. The latter is corroborated by the thermodynamic stability of extended oxygen chain structures as compared to oxygen atoms[109]. The experimental result unequivocally shows the presence of two different CO species on the surface. The one at low-frequency has the lower binding energy, since its relative intensity increases with temperature. It is also interesting to note that the intensity of the high-frequency component saturates within a very narrow temperature window as one would expect for an adsorption site with a well-

defined adsorption site. In contrast to that, the signal at lower frequency gains intensity over a wider temperature window, which indicates a rather broad distribution of binding energies. Most likely this is due to intermolecular interactions, which would also fit to the frequency shift observed with decreasing temperature.

7 CO Oxidation on Au(332)

In this chapter, CO oxidation on Au(332) is investigated as a reaction to test the new molecular beam apparatus.CO oxidation is a widely studied model reaction and has been studied on a large variety of transition metal-based catalysts[110–115]. In addition, it has also been intensively investigated on metal single crystal surfaces including Au[19,116–119]. However, gold itself is inactive towards CO oxidation, because of its inability to activate molecular oxygen, which is only weakly bound but has a high barrier for dissociation on Au surfaces.

Friend and co-workers have found that adsorption of ozone on Au(111) leads to surface reactivity for both total as well as selective oxidation reactions[120]. Apart from ozone also other methods were employed to produce active oxygen species on the Au surface such as: (i) deposition by a plasma source[121,122] or oxygen-ion sputtering[123], (ii) adsorption of NO_2[124], (iii) thermal dissociation of O_2[125,126] or by a microwave discharge[127]. The activity of O-covered Au single-crystal surfaces for CO oxidation under UHV conditions have been studied by several groups[128–132]. The investigations show that the reactivity of the oxygen species decreases with increasing oxygen coverage. To this end, scanning tunnelling microscopy (STM) studies revealed differences in the surface morphology depending on the temperature used for oxidation as well as on the coverage of atomic oxygen[133,134]. With respect to the electronic structure X-ray photoelectron spectroscopy (XPS)[130] showed that the local bonding of oxygen depends on oxygen coverage as well as the oxidation temperature as well. This qualitative result is preserved for all the preparation methods of oxygen atoms mention previously.

CO oxidation on gold has also been studied theoretically[135,136,34,137–141]. DFT calculations showed different activation energy for CO oxidation on Au surface ranging from 0.27 eV for MgO-supported Au clusters[34] to 0.6 eV for stepped and kinked Au(321) surface[142]. Recently Moskaleva and co-workers[109] have shown that when surface oxygen is present in excess at coverages greater than 0.2 ML on the Au(321) surface, the Au atoms at step edges are involved in the formation of Au–O chain-line structures, which are

thermodynamically more stable than individual oxygen atoms. In addition, a diffusion barrier of about 0.4–0.5 eV was found for such chain-line structures rendering them also kinetically more stable than the oxygen atoms with diffusion barrier of about 0.2 eV.

In this chapter, CO oxidation on a stepped Au(332) surface is investigated using pulsed isothermal molecular beam experiments following the time-dependent evolution of gas phase products by time-resolved mass spectrometry and the formation of surface species by IRAS. The first section will discuss the dependence of the transient and the overall CO_2 production rate on the oxygen atom flux under isothermal conditions. The next section presents results on CO oxidation at different temperatures to obtain qualitative information about the temperature dependence of the overall reaction rate. Finally, the last section focuses on in-situ infrared spectra in order to correlate the observed reaction kinetics with the nature of species on the surface.

7.1 Dependence on flux of atomic oxygen

Figure 7.1 shows a typical transient CO_2 production experiment where the sample is exposed to a continuous ^{13}CO beam and a modulated beam of oxygen atoms (11 pulses, 120 s on, 200 s off) while monitoring the oxidation product $^{13}CO_2$ (m/z = 45) by time-resolved mass spectrometry (MS). To investigate the influence of the atomic oxygen flux on the production rate of CO_2, two different O_2 pressures measured inside the scattering chamber were used: a smaller one ($p(O_2) = 3.2 \cdot 10^{-8}$ mbar), which corresponds to a O-atom flux of $1.4 \cdot 10^{12}$ atoms$\cdot$cm^{-2}s^{-1} and a higher one ($p(O_2) = 1.4 \cdot 10^{-7}$ mbar) corresponding to a flux of $7.3 \cdot 10^{12}$ atoms$\cdot$cm^{-2}s^{-1}. The flux of the ^{13}CO beam ($7.3 \cdot 10^{14}$ molecules$\cdot$cm^{-2}s^{-1}) and the sample temperature (200 K) were kept constant in both experiments. The ^{13}CO flux exceeds the flux of O-atoms by more than two orders of magnitude. While oxygen atoms (desorption temperature above 500 K) are stable adsorbates at 200 K, ^{13}CO is bound only transiently at this temperature. Above 180 K no stable CO adsorption is found on the Au(332) surface under UHV conditions. The IR investigations (**Chapter 6**) have shown that there is a measureable transient CO coverage under the

condition used here, which can be estimated to correspond to 25% of the maximal coverage observed at 100 K if one assumes a linear correlation between IR intensity and coverage.

The traces in **Figure 7.1** show a rapid increase of $^{13}CO_2$ formation after opening the O-atom beam. Upon closing the oxygen beam a rapid drop of $^{13}CO_2$ formation is observed. The corresponding MS signal goes back to background level within the delay time between the pulses. This general behaviour holds for both oxygen atom fluxes, however, significant differences are observed, too. Comparing the reactivity of the system as probed by the intensity of the m/z = 45 signal along the series of oxygen pulses, a slow decay of the reactivity is observed (see **Figure 7.1B**). While the reactivity remains constant for the first 3-4 pulses and it drops by 26% for the last pulse within this series. In contrast to that, for the higher O-flux the reactivity drops already after the first pulse and decreased by about 30% within the first 5 pulses. While the decrease within each pulse is not very large for the first 5 pulses, the pulse shape of the pulses 6 to 8 changes significantly revealing a rapid decrease of reactivity within the oxygen pulse. For the subsequent pulses the reactivity levels off at about 19% of the initial reactivity.

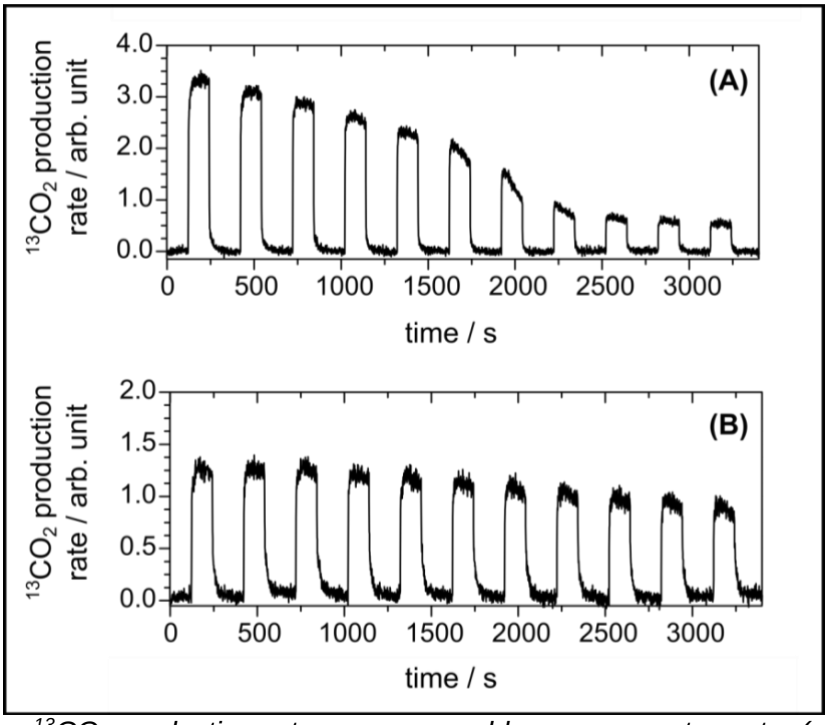

***Figure 7.1**: $^{13}CO_2$ production rate as measured by mass spectrometry (m/z = 45) for a continuous ^{13}CO beam (p = 2.4•10^{-6} mbar) and a modulated ^{16}Oatom beam impinging on the Au(332) surface (T_{sample} = 200 K). The background pressure of the molecular oxygen in the chamber was (**A**) P_{O2} = 1.4•10^{-7} mbar and (**B**) 3.2•10^{-8} mbar.*

The results in **Figure 7.1** clearly show the deactivation of the surface to be dependent on O-flux, which is significantly faster for higher O-flux. As shown inliterature[133,134] the reactivity of oxygen deposited on Au surfaces drops at higher oxygen coverage, which was explained by the formation of Au-O phases being less reactive towards CO oxidation. This interpretation implies that under the conditions used here CO oxidation cannot compete with the formation of Au-O phases, which means that the diffusion of O atoms impinging onto the Au surface is fast as compared to CO oxidation. This is well in line with the theoretical predictions as mentioned above.

The formation of Au-O phases should have consequences for both the chemical composition as well as the long-range order of the surface. Therefore, the surface was investigated by Auger spectroscopy and LEED after the reaction to elucidate these aspects (see **Figure 7.2**). **Figure 7.2A** shows the Auger spectrum of the Au(332) surface after reaction at low (red curve) and high (blue curve) oxygen pressure, respectively. For comparison, the spectrum of the clean surface (black curve) is also added. The spectrum of the clean Au(332) surface does not show signals associated to oxygen at 469 eV. However, at high O-flux oxygen is clearly detected on the surface. On the other hand, for low O-flux, a much smaller oxygen signal at 469 eV is observed, which is in agreement with the less pronounced deactivation of the surface. **Figure 7.2B** presents LEED images of the corresponding surfaces before and after the reaction cycle. The clean Au(332) surface shows the expected LEED pattern with sharp spots and little background, which is characteristic for a stepped surface with a long-range order of terraces as described in **Chapter 5**. At the end of the reaction cycle with low O-flux, the LEED spots are reduced in intensity, while the background intensity increases considerably. After CO oxidation at the high O-flux conditions the characteristic LEED pattern of the Au(332) surface has vanished. The lack of diffraction spots also implies that the Au-O phase created during the reaction does not exhibit a long-range order.

The long-term behaviour of the surface and the reactivity of the chamber walls under these conditions was investigated in another experiment, for which the number of oxygen pulses was increased keeping the other conditions (pulse duration, CO pressure, sample temperature etc.) constant (see **Figure 7.3**).

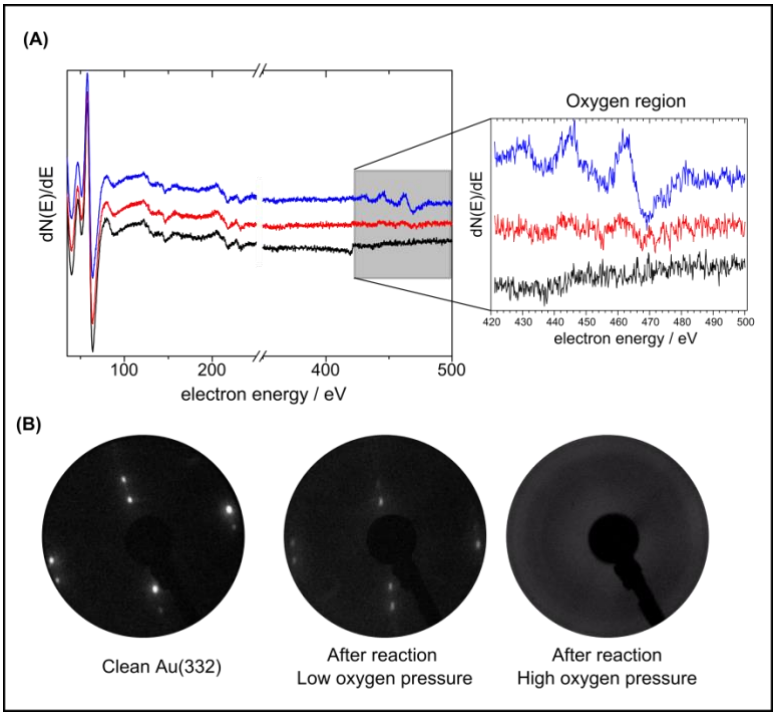

***Figure 7.2**: Analysis of the Au(332) surface after CO oxidation reaction at 200 K after 11 oxygen pulses. (**A**) Auger spectra of the Au and O regions of a clean surface (black curve), after reaction at low (red curve) and at high (blue) oxygen pressure – left, and a close up of the O energy range – right.(**B**) LEED pictures of the surface before and after the reaction.*

At the 25th oxygen pulse, the sample is removed from the scattering position to the preparation chamber to compare the remaining activity of the Au(332) surface with the activity of the chamber walls. In addition, the flow monitor was placed at the sample position for some of the pulses, to exclude a significant effect of the mass spectrometric signal induced by the change in the scattering condition of the educts.

As seen in **Figure 7.3**, at high oxygen pressure the qualitative behaviour is preserved. The system shows a rapid deactivation within the first eight pulses. The forthcoming oxygen pulses result in a further reduction of the reactivity, however, at a much smaller rate. For the last five pulses a stable residual activity of about 1/6 of the initial one is observed. If comparing the reactivity of the Au surface at the end of the 25 pulses with the background reactivity of the stainless-steel chamber a very small difference remains. This difference does not depend on the scattering conditions (the same reactivity is observed with and without the flow monitor at the position of the sample). This result suggests that even the oxidized Au surface has some remaining activity towards CO

oxidation, which is significantly higher than stainless steel. In contrast to that, the system retains a much higher activity at low oxygen pressure even for a larger number of pulses; however, activity drops steadily within the series of oxygen pulses. The higher activity of the Au surface after the series of oxygen pulses is further substantiated by comparing it to the reactivity of the chamber under these reaction conditions. While the difference between the reactivity of the chamber and the Au surface was 19% for the high oxygen atom flux, it is more than threefold the background activity after the series of pulses using the lower oxygen atom flow.

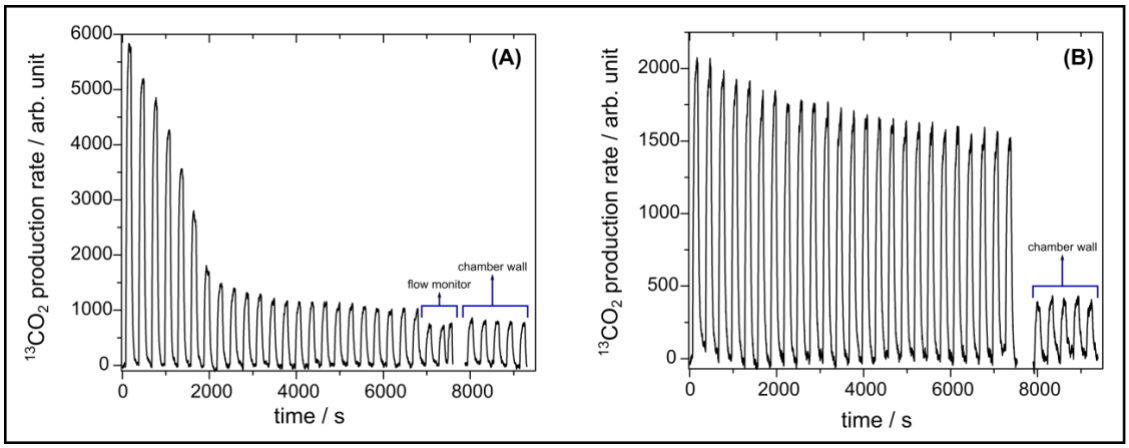

***Figure 7.3**: Long term stability of the surface for CO_2 production rate during 25 oxygen pulses (120 s on, 200 s off) and a constant ^{13}CO beam, T_{sample} = 200 K. The reactivity of the chamber walls and the flow monitor are indicated. The inset shows the background reaction of the chamber. (**A**) P_{O2} = 1.4 x 10^{-7} mbar and (**B**) 3.2 x 10^{-8} mbar. This experiment was performed using an MS pulsing counting mode.*

These results are in line with the formation of a Au-O phase on the Au(332) surface. The formation of the Au-O phases is expected to be slower for lower O-flux, as it requires oxygen atoms to diffuse on the surface to these phases, which competes with CO oxidation. As the flux of CO was kept constant the balance should be shifted towards CO oxidation for decreasing oxygen atom flux. As a result, a higher residual activity is expected for the lower oxygen flux after the same number of pulses. This is partially due to the reduction of the transient CO concentration on the Au surface as shown by IR spectroscopy in **Chapter 6**. However, it is also due to a reduced reactivity of these Au-O phases as suggested by the titration experiments reported in literature[86]. The residual activity of the strongly oxidized Au surface after 25

pulses of higher oxygen flux suggests that this surface is still significantly more active towards CO oxidation than stainless steel.

7.2 Temperature Effect

Temperature is an important factor for reactivity. **Figure 7.4** shows the $^{13}CO_2$ production rate at different temperatures using the pressure conditions of the low oxygen flux discussed above. However, the duration of the oxygen pulses was extended to 360 s interrupted by equally long delay times.

In contrast to the results for T = 200 K (see **Section 7.1**), the surface shows a reproducible behaviour of $^{13}CO_2$ formation along the series of oxygen pulses for all temperatures (**Figure 7.4**). Moreover, a similar pulse shape is observed within this temperature range (T = 220–300K). The shape is characterized by a fast increase of CO_2 production after opening the oxygen shutter. The maximum of CO_2 production is reached after about 70 s. After reaching the maximum, the CO_2 production slowly decreases during the O-atom pulse. After closing the oxygen shutter, the MS signal goes back to baseline; however, the decay is significantly slower than the rise of the signal at the beginning of the pulse.

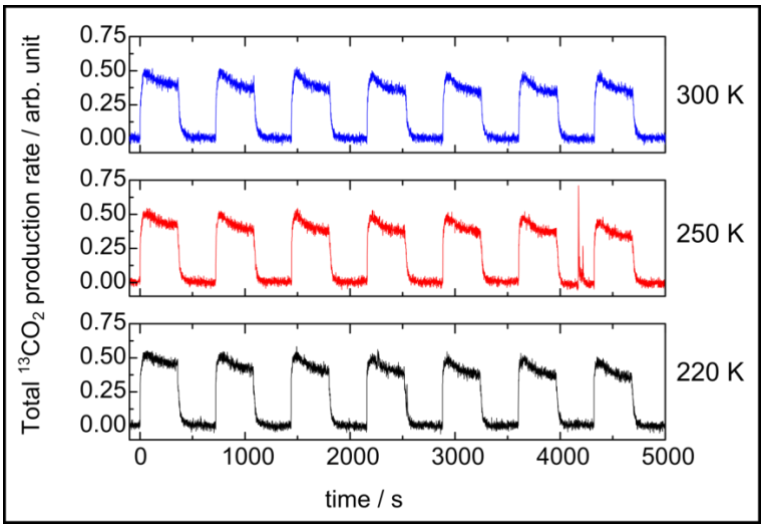

Figure 7.4: *Temperature dependence on the total $^{13}CO_2$ production rate. The oxygen and ^{13}CO pressures are kept constant, $3.2 \cdot 10^{-7}$ mbar $2.4 \cdot 10^{-6}$ mbar, respectively. While the reaction temperature is varied: at 220 K (black trace), 250 K (red trace), and 300 K (blue trace).*

In contrast to the behaviour at 200 K, a clear deactivation of the reaction is observed in the course of each oxygen pulse irrespective of temperature. This observation indicates that the processes resulting in a deactivation of the system are even more important at elevated temperature than at 200 K. In particular, it suggests that the formation of Au-O phases gains importance, which implies that the balance between oxygen atom diffusion and reaction with CO is shifted towards diffusion. This is in line with the results from temperature dependent IR spectroscopy, which revealed a significant decrease of CO coverage in this temperature range while the sticking probability of oxygen atoms is expected to be similar. The shape of the first pulses at 200 K lack indications for a significant deactivation of the system but show a slow by continuous decline of the reactivity with increasing number of pulses. It might hence be surprising that the system shows reproducible reactivity within the series of pulses at temperature above 220 K but deactivates faster within each pulse. The recovery of the reactivity during the delays between the pulses, points to the fact that the reactivity of the Au-O phases, which is considered responsible for the deactivation, is enhanced at elevated temperature such, that oxygen stored in these phases during the oxygen pulse can be removed during the delay times by the continuously impinging CO molecules. The residual activity after closing the oxygen atom supply is in line with this interpretation.

It is surprising that both the pulse shape as well as the CO_2 production rate does not vary with temperature between 220 K and 300 K. Based on Arrhenius theory it is expected that the rate constant of a reaction depends exponentially on temperature. On the other hand, the reaction rate depends not only on the rate constant but also on the concentration of the educts. Above the desorption temperature, the transient concentration on the surface should decrease exponentially with temperature, hence it is possible that both effects simply cancel. The situation is, however, more complex as the collision probability of the reaction between CO and oxygen atoms on the surface depends on the diffusion rate of the partners, which is a function of temperature. Furthermore, it is important to realize that the overall reactivity of the system is determined by more than the reaction of oxygen atoms with CO towards CO_2. CO is expected to react with oxygen present within the Au-O phases, which is a

function of their size but will also be a function of temperature. Due to this complexity of the reaction network, a conclusive explanation for the observed temperature dependence of the reactivity cannot be given at present and additional experiments are needed to draw more solid conclusions.

7.3 Transient Kinetics of CO_2 Production

One key feature that makes molecular beam studies of gas-surface interactions unique is that they are carried out under well-defined flux and single collision conditions, which allows to assume that products will result from the initial encounter of the educts with the surface. In turn, this allows to interpret both steady-state but also the transient kinetics of the system quantitatively[143–145]. In the following, pulse profiles of the $^{13}CO_2$ production at 200 K will be discussed for both low and high oxygen flux conditions. Subsequently, the transient profiles of $^{13}CO_2$observed at higher sample temperature will be discussed. In the following, the $^{13}CO_2$ transients are normalized to the maximum pulse height, for a more convenient comparison of the pulse shapes.

Transients for the two reaction conditions, high and low flux of oxygen, are compared in **Figure 7.5**. In general, a fast onset component in the $^{13}CO_2$ transient pulse is observed upon the admission of the oxygen beam (**Figure 7.5** – solid red line), followed by a slower increase in the reaction rate towards the $^{13}CO_2$ production maxima (**Figure 7.5** – dotted red line). Depending on the condition the $^{13}CO_2$activity remains constant (**Figure 7.5 A** bottom) or decline after reaching the maximal value (all other in **Figure 7.5 A** and **C**). After closing the O-beam, the reaction rate drops towards the background (hatched area), as the remaining active oxygen species is consumed by the continuously impinging CO molecules.

At 200 K, the first $^{13}CO_2$ transient at low oxygen flux conditions shows a constant reactivity after the initial rise mentioned above; while for high oxygen flux condition the reactivity drops slightly towards the end of the pulse (see **Figure 7.5A**). **Figure 7.5B** reveals a significant difference between the two oxygen flux regimes. While the reactivity of the subsequent oxygen pulse reaches the reactivity observed at the end of the preceding pulse, this is not the

case for the high oxygen flux. This observation is remarkable as the deactivation was associated with the formation of Au-O phases on the Au surface. After closing the oxygen beam no additional O atoms are impinging onto the surface. On the contrary, some of the oxygen present on the surface is removed by CO oxidation as seen from the hashed area in **Figure 7.5A**. This suggests that at high oxygen flux conditions the surface restructures during the delay times, which results in a less active surface at the beginning of the subsequent oxygen pulse. For low O-flux conditions (**Figure 7.5B** – black trace) the reaction rate maximum of the subsequent pulse reaches the level of the preceding one. However, a decrease of the reactivity is also observed for the low oxygen flux condition starting after the 3rd pulse. This decrease is accompanied by a change in the pulse shape. While the pulse shape of the first pulse suggests a steady state reactivity, the pulse shapes observed for the later pulses exhibit a clear decrease of the reactivity towards the end of the oxygen pulses, which is illustrated for the 7th pulse in **Figure 7.5C** (bottom). The deactivation during the pulse is even more severe for the high oxygen flux conditions as illustrated in **Figure 7.5C** (top). For this pulse the reactivity drops by about 40% in the course of the pulse.

If the direct reaction CO + O to CO_2 would be the only process, one would expect to see a simple $^{13}CO_2$ transient corresponding to a reaction of pseudo first order as the concentration of CO is kept constant. The transients show a fast initial rise of reactivity, however, the shape of the traces at later times deviate considerably from expectations based on a simple pseudo first order reaction, which points to a more complex reaction mechanism involving different reaction pathways. Qualitatively, this is understood by the formation of Au-O phases which show a decreasing reactivity with increasing oxygen coverage. The growth of the Au-O phase is readily understood by the barrier for CO oxidation (~0.6 eV)[142] as compared to the barrier for diffusion of oxygen atoms (~0.45 eV)[108] on the Au(321) surface and the thermodynamic stability of Au-O phases with respect to individual oxygen atoms[109]. The dependence of CO oxidation activity on oxygen coverage was explained by results of STM and XPS experiments showing the presence of different types of oxygen depending on oxygen coverage[130,133]. Unfortunately, a quantitative evaluation of the data in terms of the oxygen content on the surface is hampered by the fact that one

cannot assume the same surface condition at two points along the pulse sequence due to the progressive deactivation of the surface. In turn, the amount of oxygen atoms remaining on the surface after the pulses cannot be determined.

This is different for the experiments done at higher temperature. For these experiments, a reproducible pulse shape with a fast initial increase followed by a slower increase towards the maximum and subsequent decline represented by solid and dotted red lines in **Figure 7.6** was observed within the series of oxygen pulses. As the flux of impinging oxygen atoms is constant during the pulse, it is readily clear that the surface accumulates oxygen. On the other hand, the system exhibits a reproducible behaviour for a series of pulses, which implies that the surface has to be in the same condition at the beginning of each pulse. In particular, the result is inconsistent with a progressive accumulation of oxygen during the pulses, which is clearly shown by the pulse shape during the oxygen pulses. This apparent contradiction can be resolved by assuming oxygen to react off the surface in the delay periods.

More quantitative one has to assume that the amount of oxygen stored on the surface during the pulse has to match the amount reacted off during the delay pulses. In turn one can integrate the area of CO_2 production after the pulse as well as the area underneath the oxygen pulse to determine the amount of oxygen sticking to the Au surface during the oxygen pulse. This allows to construct the shape of the ideal CO_2 reactivity trace assuming a fast reaction of all impinging oxygen atoms on the surface towards CO_2. The latter curve is shown as a blue rectangle for the reaction at 220 K. These experiments were using oxygen pulses corresponding to approximately $8 \cdot 10^{14}$ atoms$\cdot$cm^{-2} (see **Chapter 4**). Fraction of the hashed area after the oxygen pulse as compared to the area underneath the blue rectangle is then nothing but the amount of oxygen stored during the oxygen pulse. In doing so, one obtains a surface coverage of about $7 \cdot 10^{13}$ O-atoms$\cdot$cm^{-2} (0.05 ML) accumulated on the surface at the end of the oxygen pulse.

The amount of oxygen found on the surface at the end of the pulses is similar for all temperature, which is in line with the transients and the retained intensity of $^{13}CO_2$ signal observed at different temperatures.

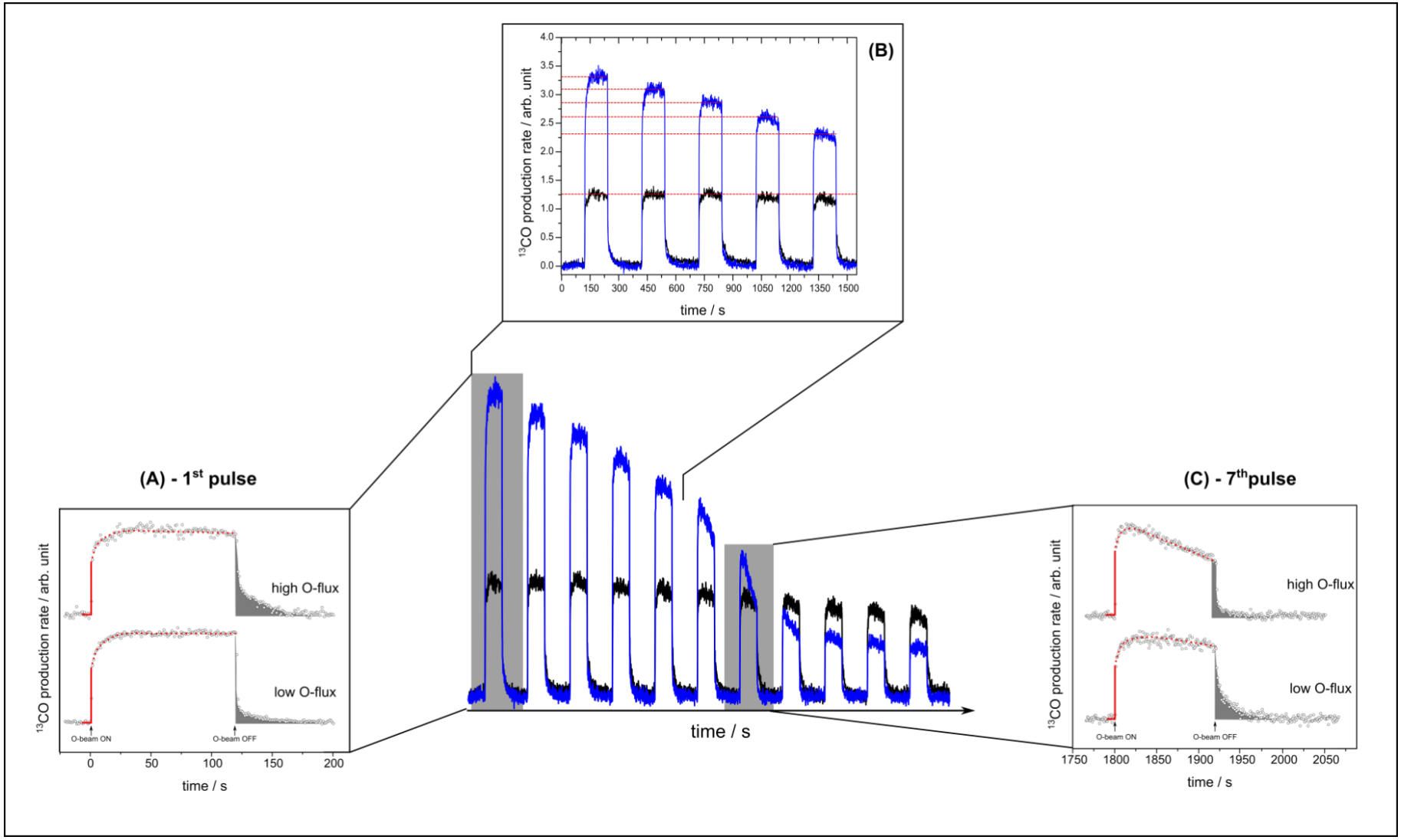

Figure 7.5: *Transient CO_2 production rates at 200 K for high (p_{oxygen} = 1.4 x 10^{-7} mbar – blue trace) and low (p_{oxygen} = 3.2 x 10^{-8} mbar – black trace) oxygen fluxes.(**A**) First transient of $^{13}CO_2$signal, (**B**) decrease in $^{13}CO_2$ formation indicated by a dotted red line and (**C**) 7th transient of $^{13}CO_2$signal for both oxygen fluxes. Fast and slow components are represented by a solid and dotted red line, respectively, constituting a guide for the eye. The hatched area in A and C represents the CO_2 production after closing the O-beam.*

It should be noted that already this very small amount of transient oxygen concentration leads to a measurable decrease of the surface reactivity by about 10%, which proofs the sensitivity of the measurements for slight modifications of the surface. The current experiments clearly show, that even small amount of oxygen accumulating on the surface, reduces the reactivity of the surface as oxygen atoms are more reactive than oxygen stored in Au-O phases. This result is also important for the understanding of the reactivity of np-Au. In case of np-Au, molecular oxygen is activated, which is believed to take place on the Ag moieties present on the surface of the system. The oxidation reaction is believed to take place on the Au surface as well, based on the reactivity and selectivity of np-Au observed for more complex partial oxidation reactions. Hence, the result clearly indicates, that the formation of Au-O phases even at low coverage (here about 5 % of a monolayer) will reduce the reactivity of the system.

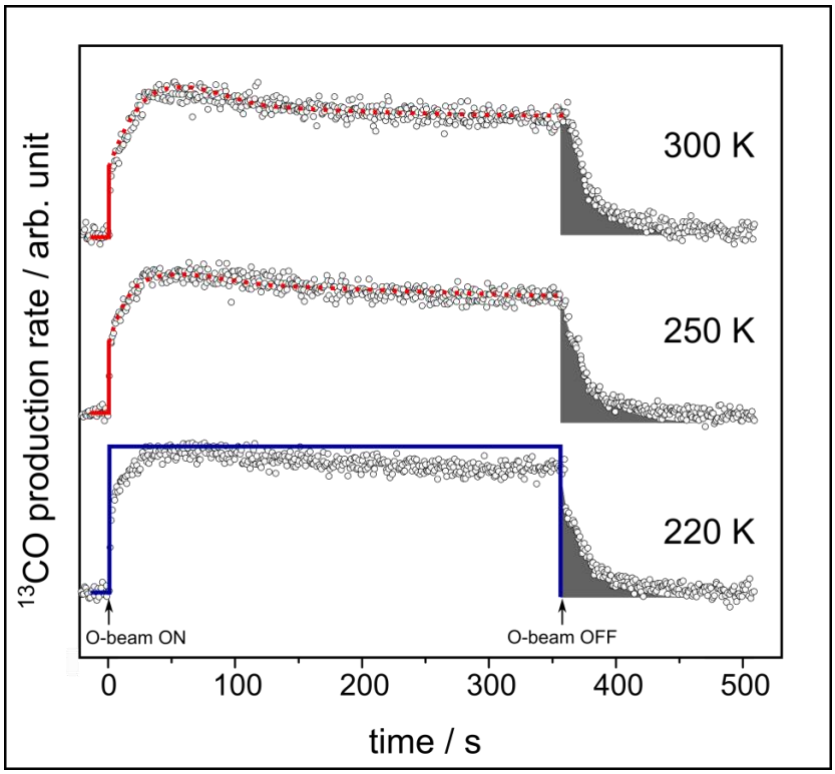

***Figure 7.6**: Signals of transient $^{13}CO_2$ production rate as a function of sample temperature. Oxygen pressure = $3.2 \cdot 10^{-8}$ mbar (360 s beam ON and 360 beam OFF) and $^{13}CO = 2.4 \cdot 10^{-6}$ mbar. Fast and slow components are represented by a solid and dotted red line, respectively, constituting a guide for the eye. The blue line represents an ideal rectangular pulse shape and the hatched areas represent the CO_2 production after closing the O-beam.*

7.4 *In-situ* IRAS

Finally, the reactivity results discussed above will be compared to *in-situ* IRAS spectra taken during the course of a CO oxidation cycle. **Figure 7.7** displays the isothermal infrared spectra, at 200 K, for high (left) and low (right) oxygen flux, corresponding to the reactivity data shown in **Figure 7.1**. The traces shown in black correspond to the oxygen beam off while the blue spectra were taken, while the O-beam was impinging on the surface.

For high oxygen flux, the first spectrum taken after equilibration of the system with the ^{13}CO beam ($p(^{13}CO) = 2.4 \cdot 10^{-6}$ mbar) shows a pronounced peak at 2075 cm^{-1}, which is characteristic for ^{13}CO adsorption on steps of the Au(332) and is in line with observation made for the pristine gold surface discussed in **Chapter 6**. Moreover, an additional high energy shoulder at 2085 cm^{-1} is detected. In light of the signals to be observed after an admission of O-atoms this small signal may be due to some O-atoms already present on the surface.

The IR intensity observed here is very comparable to the one measured on a pristine Au(332) surface at the same temperature, 200 K (see **Chapter 6**). With increasing the number of O-pulses changes of the CO adsorption band is observed. Two new vibrational bands at about (**B**) 2088 cm^{-1} and (**C**) 2103 cm^{-1} appear, which are blue-shifted with respect to ^{13}CO at step of clean Au(332) surface. At low oxygen exposure, the band **B** is more intense, while band **C** grows in at later stages. The intensity of the line corresponding CO adsorbed to the clean Au surface decreases rapidly with increasing oxygen exposure. At the beginning of the experiments, the intensity of the CO signals corresponding to CO bound on oxygen covered areas decreases when the beam is switched off, while line **A** corresponding to CO on the clean Au surface recovers slightly in the delay periods. At the high flux condition lines **A**, **B** and **C** all disappear beyond the 8^{th} pulse. The loss of these CO bands coincides with drastic reduction of the reactivity of the Au(332) surface (see **Figure 7.1**). Additionally, in the reaction course a persistent extra vibrational band is observed at about 2030 cm^{-1} (**D**).

The two bands **B** and **C** observed above correspond well to the doublet of line observed for the oxygen pre-covered Au(332) surface discussed in **Chapter 6.** In line with the interpretation given there the bands **B** and **C** can be assigned to CO bound to different sites of oxidized Au atoms at oxidized step or kink sites of the Au(332) surface. The vibrational band **D** was, however, not observed for the CO adsorption experiments on the oxygen covered Au(332) surface discussed in **Chapter 6.** At the moment, the origin of this band is not clear and further experiments are necessary exclude experimental artefacts.

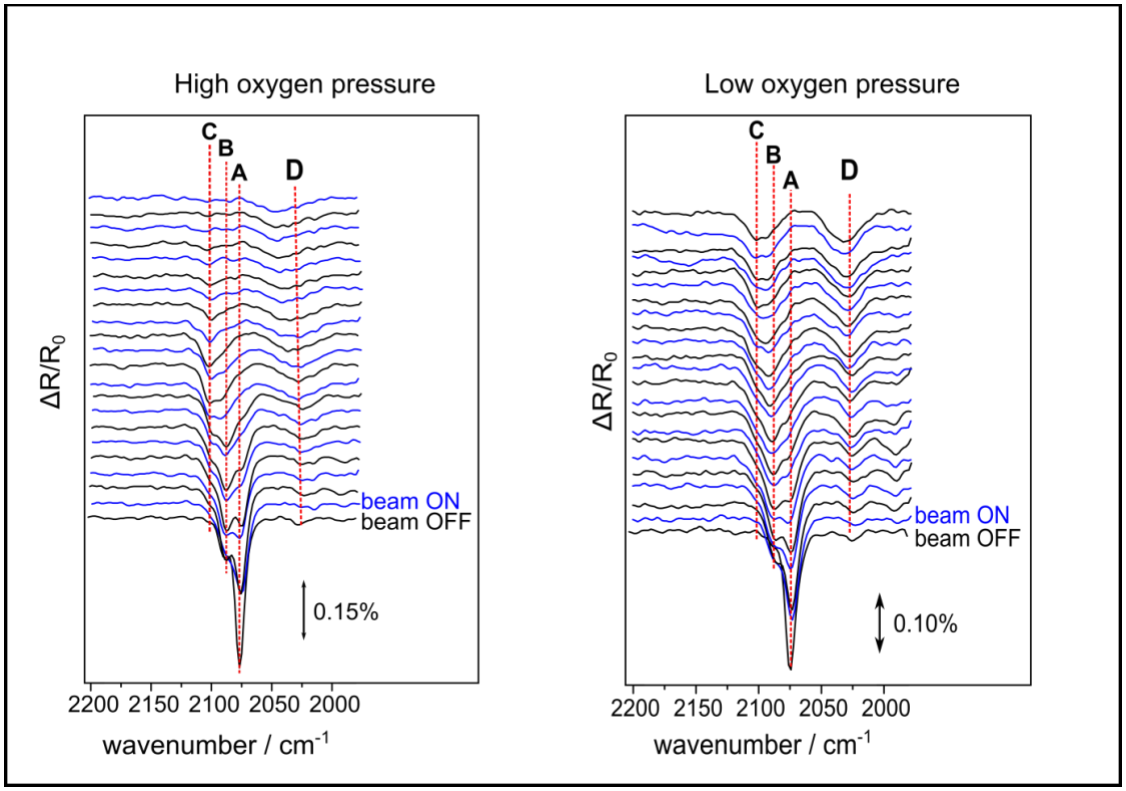

Figure 7.7: *In situ infrared at high oxygen pressure of $1.4 \cdot 10^{-7}$ mbar (left) and at low oxygen pressure of $3.2 \cdot 10^{-8}$ mbar for the reaction performed at 200 K. Beam ON (blue lines) corresponds to a 120 s oxygen pulse directly impinging on the Au(332) surface and Beam OFF (black lines) corresponds to O-beam shutter closed. ^{13}CO beam is constantly impinging on the surface along the reaction course. Different ^{13}CO chemical environment is probed (**A**) 2075 cm^{-1}, (**B**) 2088 cm^{-1}, (**C**) 2103 $cm^{-1}$and (**D**) 2030 cm^{-1}.*

The IR spectra taken under at low oxygen flux condition (**Figure 7.7**right) show a similar behaviour. Prior to the oxygen pulses a band at (**A**) 2075 cm^{-1} with an adjacent high energy shoulder at 2085 cm^{-1} is observed in line with the results discussed above. Upon O exposure, the signal **A** decreases, while at 2088 cm^{-1} (**B**) is seen during the entire pulse sequence. In

line with the observations made for the high O-flux, the signal at 2075 cm^{-1} recovers slightly in the delay times between the first two pulses but disappears completely at the end of the pulse series. The signal at 2088 cm^{-1} exhibits a shift towards higher wavenumbers for elevated oxygen exposure and exhibits a slightly decreasing intensity in the course of the experiment. At later oxygen pulses an additional line at 2103 cm^{-1}(**C**) appears in line with the previous results.

The changes of ^{13}CO chemical environment probed along the reaction course are qualitatively similar to the ones observed at high O-flux but proceed slower. In contrast to the high O-flux experiment, which shows only a band at about 2030 cm^{-1}at the end of the reaction cycle, the bands **B**, **C** associated to CO bound to oxygen covered steps and kinks are still observed at the end of the experiment. In addition, a pronounced line at about 2030 cm^{-1} (**D**) is present, which is comparable to the situation at high O-flux; however, the assignment of this band at the moment is uncertain and additional experiments are needed to draw more solid conclusions.

From both rate measurements and *in-situ* IRAS it is apparent that the accumulation of oxygen atoms on the surface decreases the transient concentration of CO on the surface. It is important to note though that there is no one to one relation between the reductions in transient CO concentration and oxidation rate of carbon monoxide. For the low oxygen flux the IR intensity of CO bound to the Au surface drops to 78% at the end of the pulse sequence, while the reactivity drops by 23%. It is however, important to note that the loss of transient CO concentration on the surface under high oxygen flux conditions correlates with the fast decay of CO oxidation activity of the system observed in the middle of the pulse series presented in **Figure 7.1**. On a molecular level, several contributions may contribute to this inhibition effect, such as site blocking of CO adsorption site due to the formation of Au-O phases or possible variations of the activation barrier for oxidation and desorption induced by the accumulation of oxygen.

8. The Influence of Water on the CO Oxidation

In previous studies water was reported to adsorb and desorb molecularly on clean Au single-crystal surfaces[146–149]. In the presence of atomic oxygen on Au single-crystal surfaces TPD spectra exhibit a water desorption peak about 20 K higher than found on the clean Au surface, which can be understood by a stabilization of molecular water by adsorbed oxygen. Based on these experimental observation it was suggested that water reacts with atomic oxygen to form two surface hydroxyl groups[146,147,150,151]. Theoretical calculations found the formation of the hydroxyl groups to be a slightly endothermic process on both the Au(111)[151] as well as stepped Au(321)[152] surfaces. However, on Au(100) and small gold clusters[153,154] theory predict an exothermic formation of hydroxides suggesting that this reaction may be sensitive to the structure of surface.

For CO oxidation, DFT calculations indicated that the barrier for CO oxidation was reduced to 0.11 eV in the presence of H_2O compared to 0.25 eV for CO oxidation on oxygen precovered Au(111) without water[150]. This reduction was attributed to a concerted hydrogen transfer from one hydroxyl in the water-hydroxyl mixed phase resulting in an OCOH intermediate, which subsequently decomposes to CO_2. Ojifinni *et al*.[155] demonstrated the incorporation of oxygen from water into CO_2 through isotope exchange using ^{18}O labelled water on a ^{16}O precovered Au(111) surface, in an isothermal titration experiment with $C^{16}O$.

A number of studies have been performed to verify the role of water for enhancing CO oxidation activity[151,156–158]. Kim *et al*.[37] have reported a ~70% enhanced CO_2 (both $^{12}C^{16}O_2$ and $^{12}C^{16}O^{18}O$) production at 140 K if comparing the total CO_2 yield of an isothermal titration experiment dosing CO onto an O precovered Au(111) surface with or without pre-adsorbed water. In turn, this implies that CO oxidation in the absence of water is not able to utilize all the oxygen precovered on the surface, which was reported to be the case if water was pre-adsorbed and has led the authors to speculate that a new reaction

mechanism involving surface hydroxyls is responsible for the observed differences.

In contrast to all experiments described so far, in catalysis reactive oxygen species are produced in the presence of CO. Due to the observed dependence of CO oxidation activity on oxygen coverage discussed before and the possible change of the reaction mechanism proposed in literature the effect of water on the steady state as well as the transient kinetics of CO oxidation on well-defined Au model surfaces under isothermal and constant educt flux conditions has not been investigated thus far.

This chapter focuses on a systematic study of the influence of water on CO oxidation over the Au(332) surface using the pulsed molecular beam strategy successfully applied in the previous chapter to investigate the kinetics under isothermal conditions. Educts and products were detected by time-resolved mass spectrometry. First, the dependence of CO oxidation on the water pressure will be discussed. To this end $D_2{}^{18}O$ is added to a mixture of ^{16}O atoms and $^{13}C^{16}O$, the reactivity of water can be directly monitored from isotopic scrambling of the reactive oxygen species yielding a $^{13}C^{16}O^{18}O$ isotopomer. In a second step the transient kinetics will be discussed in more detail.

8.1 Dependence on Water Pressure

Figure 8.1shows a series of molecular beam experiments in which CO_2 production is measured as a function of water partial pressure. The experiments use continuous beams of ^{13}CO ($p(^{13}CO) = 2.4 \cdot 10^{-6}$ mbar, flux = $7.3 \cdot 10^{14}$ molecules$\cdot cm^{-2}s^{-1}$) and $D_2{}^{18}O$ of varying pressure simultaneously impinging on the sample surface, which is held at 250 K for all experiments. CO oxidation is induced by a pulsed beam of atomic oxygen (5 pulses, 120 s beam on, 180 s beam off) with an oxygen flux of $2.2 \cdot 10^{12}$ atoms$\cdot cm^{-2}s^{-1}$ ($p(O_2) = 3.2 \cdot 10^{-8}$ mbar, $T_{cracker}$ = 1973 K).The production of the two isotopomers $^{13}C^{16}O_2$ (m/*z* = 45) and $^{13}C^{16}O^{18}O$ (m/*z* = 47) is followed by time-resolved MS. For comparison, also an

experiment in the absence of water is shown, which is conducted under otherwise identical conditions.

Figure 8.1A shows the amount of $^{13}C^{16}O_2$ formation at 250 K in the absence of $D_2{}^{18}O$. A reproducible behaviour is observed for each pulse within this series in line with the discussion presented in **Chapter 7**. Despite the pulse to pulse reproducibility of the reactivity, no steady state reactivity is reached within the pulses. Instead, the transient kinetics of each pulse shows a rapid increase of CO_2 formation within the first two seconds of the pulse, which correspond to about 50% of the observed maximal CO_2 production. Subsequently, the curvature of the trace decreases to reach a maximal CO_2 production after about 50 s. Soon after reaching the maximum, the CO_2 production rate decreases continuously until the end of the oxygen pulse. As previously discussed, this behaviour can be explained by an increasing concentration of surface oxygen in the course of the oxygen pulse. The growth of the Au-O phases formed during the accumulation of oxygen on the surface results in a decreasing CO_2 production, which is in line with the observations reported in literature[159]. Please note that the surface recovers to its initial state during the periods in between the oxygen pulses, which implies that oxygen stored on the surface during the oxygen pulses is reacted away by CO impinging on the surface in between the oxygen pulses (see **Chapter 7**). It should be noted that no formation of $^{13}C^{18}O^{16}O$ was detected in the absence of $D_2{}^{18}O$, in agreement with expectations.

When $D_2{}^{18}O$ is added to the educt feed, the production of the $^{13}C^{16}O^{18}O$ (m/*z* = 47) isotopomer (**Figure 8.1**–blue traces) is observed in addition to $^{13}C^{16}O_2$ (m/*z* = 45) (**Figure 8.1**–black traces). While the latter originates from the expected reaction of ^{13}CO with reactive ^{16}O species provided by the oxygen cracker, the formation of the $^{13}C^{16}O^{18}O$ isotopomer is a clear evidence for isotopic scrambling of ^{16}O atoms provided by the cracker and the ^{18}O labelled water, in agreement with previous literature results[151]. With increasing water pressure, the amount of the isotope exchanged CO_2 isotopomer increases markedly. While at $1.8 \cdot 10^{-7}$mbar (**Figure 8.1B**) the $^{13}C^{18}O^{16}O$ isotopomer amounts to about 13% of the CO_2 yield at the end of each pulse this fraction increases to more than 60% for the highest water pressure studied here (**Figure**

8.1D). Further information can be gathered from the inspection of the pulse shapes.

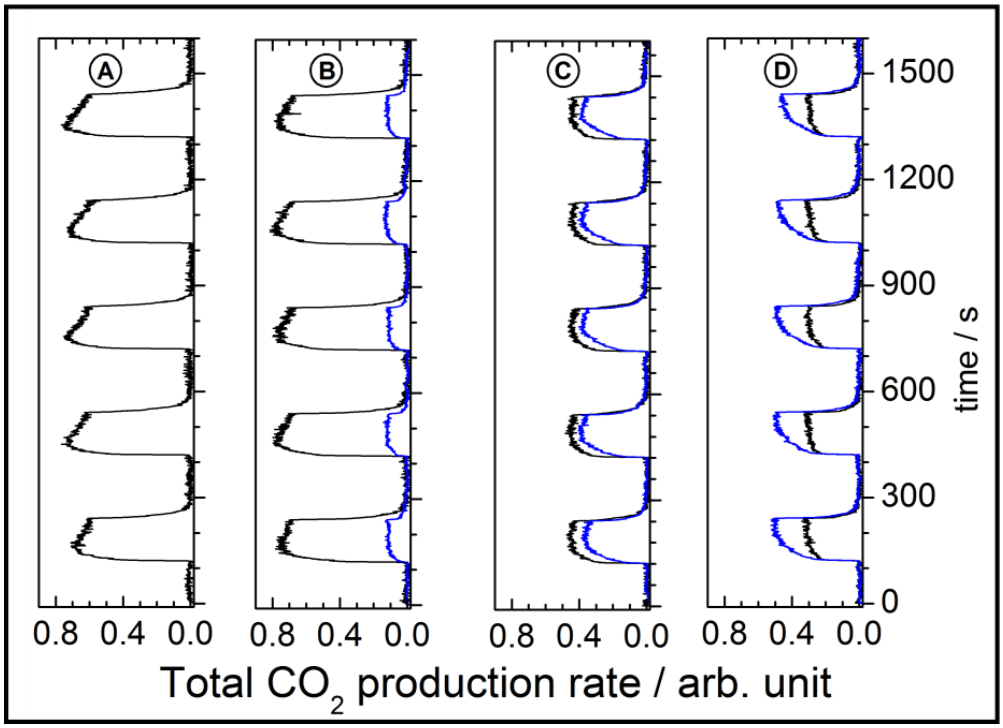

***Figure 8.1**: Formation rates of CO_2 ($^{13}C^{16}O_2$ (m/z = 45 – black trace);$^{13}C^{16}O^{18}O$ (m/z = 47 – blue trace)) in a molecular beam experiment using a pulsed oxygen beam ($p(O_2) = 3.2 \cdot 10^{-8}$ mbar) and continuous dosing of ^{13}CO ($p = 2.4 \cdot 10^{-6}$ mbar) and water ($D_2{}^{18}O$) at different pressures:(**A**) 0 mbar, (**B**) $1.8 \cdot 10^{-7}$ mbar, (**C**) $1.4 \cdot 10^{-6}$mbar and (**D**) $5.1 \cdot 10^{-6}$mbar at 250 K.*

At a low water pressure, the shape of the $^{13}C^{16}O_2$ signal is found to be the same as in absence of $D_2{}^{18}O$. In contrast to that, the pulse shape of the isotope exchanged CO_2 shows no deactivation in the course of the pulse. Instead, the $^{13}C^{16}O^{18}O$ amount increases slowly after a fast initial raise and levels off at about half the pulse length. The decrease in the formation rate of $^{13}C^{16}O_2$ across the O-pulse is almost gone for the second $D_2{}^{18}O$ pressure (**Figure 8.1C**) and is no longer observed for highest water pressure. While the trace of the mixed isotopomer ($^{13}C^{18}O^{16}O$) shows no decrease in formation rate at low water pressure (**Figure 8.1C**), a deactivation is observed for this species at intermediate water pressure (**Figure 8.1C**). Interestingly, at the highest $D_2{}^{18}O$ pressure the reduction of the isotope exchanged product is no longer observed. Moreover, it should be noted that no hydrogen or hydrogen-containing species

such as $D_2{}^{13}CO$ or $D^{13}COOD$ were detected during these experiments and also no oxygen remaining on the surface was detectable by Auger after the experiments.

To confirm steady state reactivity for the highest water pressure, the length of the oxygen pulses was extended to 360 s interrupted by an equally long delay times. In this experiment, the water pressure was about 10% smaller ($4.5 \cdot 10^{-6}$ mbar instead of $5.1 \cdot 10^{-6}$ mbar used above), which was due to experimental limitations. **Figure 8.2** shows a CO_2 transient for this experiment. Steady state reactivity is reached at about 60 s for the $^{13}C^{16}O_2$ product, while it requires a significantly longer time of ~170 s to reach the steady state for the $^{13}C^{16}O^{18}O$ product. The experiment clearly shows that the Au surface exhibits steady state reactivity at water partial pressures above $4.5 \cdot 10^{-6}$ mbar, which opens the possibliity to elucidate the properties of the surface at steady state more quantitatively.

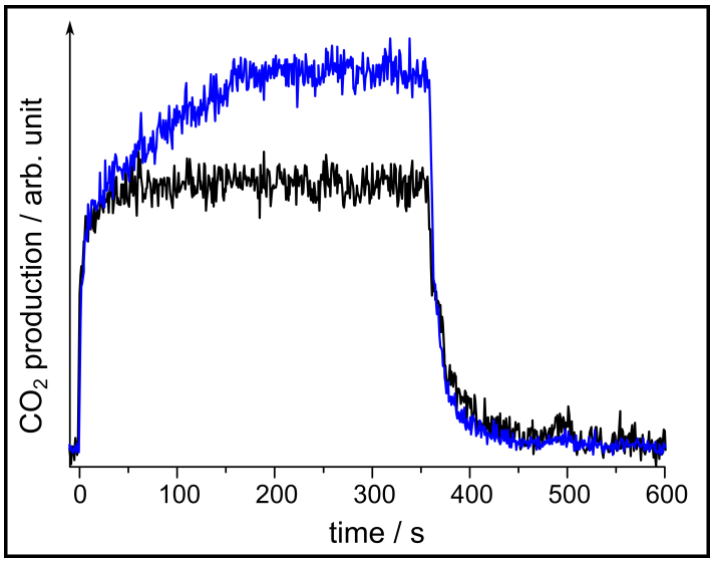

***Figure 8.2**: Formation rates of CO_2 ($^{13}C^{16}O_2$ (m/z = 45 – black trace); $^{13}C^{16}O^{18}O$ (m/z = 47 – blue trace)) in a molecular beam experiment using a pulsed oxygen beam ($p(^{16}O_2) = 3.2 \cdot 10^{-8}$ mbar, 360 s ON and 360 s OFF) and continuous dosing of ^{13}CO ($p = 2.4 \cdot 10^{-6}$ mbar and $D_2{}^{18}O$ ($p = 4.5 \cdot 10^{-6}$mbar)at 250 K.*

It was shown above that water can change the reactivity of the Au surface. In particular, the system exhibits steady state reactivity at elevated water pressure. The transient kinetics is, however, complex rendering an analysis of the underlying processes difficult. To this end it is interesting to concentrate on

the early stages of the pulses. Within the first two seconds a rapid increase of the reaction rate is observed. At the same time the total amount of oxygen atoms impinging on the surface during this time amounts to $4.4 \cdot 10^{12}$ O-atoms•cm^{-2}. At such a low O-atom exposure, it is reasonable to assume that the observed reactivity towards CO_2 is largely determined by the direct reaction of CO with adsorbed O-atoms. **Figure 8.3** shows the initial activity of the surface two seconds after admission of the oxygen beam as a function of water pressure. The black symbols in **Figure 8.3** representing the total reactivity show a slight increase of 13% for the lowest water pressure as compared to the dry feed. However, at the higher water pressures the total rate decreases again and is found to be very close to the value of the dry feed. As expected from the qualitative discussion above, the reactivity towards the $^{12}C^{16}O_2$ isotopomer (red symbols) decays with increasing water pressure while the $^{13}C^{16}O^{18}O$ evolution (blue symbols) shows the opposite trend. The formation of the$^{13}C^{16}O^{18}O$ as a function of $D_2{}^{18}O$ pressure increases quite strongly at low water pressures but levels off at higher water pressure. Attempts to fit the pressure dependence result in a best fit using a square root behaviour.

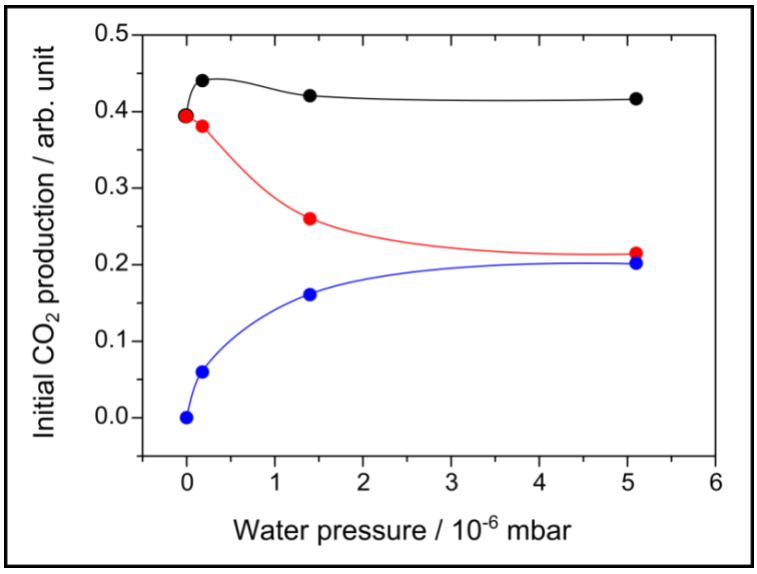

***Figure 8.3**: Initial reactivity (after the first 2 s) towards CO_2 upon admission of the O-beam as a function of water pressure using the data presented in **Figure 8.1**.Total (sum of both isotopomers) CO_2 reactivity (black symbols); $^{13}C^{16}O_2$ channel (red symbols); $^{13}C^{16}O^{18}O$ channel (blue symbols). The lines are a guide to the eye.*

The small changes of the initial CO_2 reactivity with water pressure indicate that water does not affect the reactivity of O-atoms with CO towards CO_2.

However, increasing the water pressure enhances the fraction of isotopically exchanged CO_2. Note that the $^{13}C^{16}O^{18}O$ channel shows the same initial kinetics as the $^{13}C^{16}O_2$ channel (**Figure 8.2**), which suggests that both species share the same rate limiting step. While experiments with a better time resolution would be needed to substantiate this statement, the present results are consistent with this interpretation. If both isotopomers share the same rate limiting step, one can conclude that a fast isotope exchange reaction precedes CO oxidation. For the reaction of oxygen atoms with CO dominating at the beginning of the oxygen pulse, the isotope exchange reaction can be readily understood by the reaction of an oxygen atom with water forming two hydroxyls presented in **Scheme 1.** The equilibrium of oxygen atoms plus water and two hydroxyl groups is a facile channel for the isotope exchange as the formation of ^{18}O atoms is associated with the production of a $D_2{}^{16}O$ molecule, which desorbs under the reaction conditions, hence rendering the back reaction impossible.

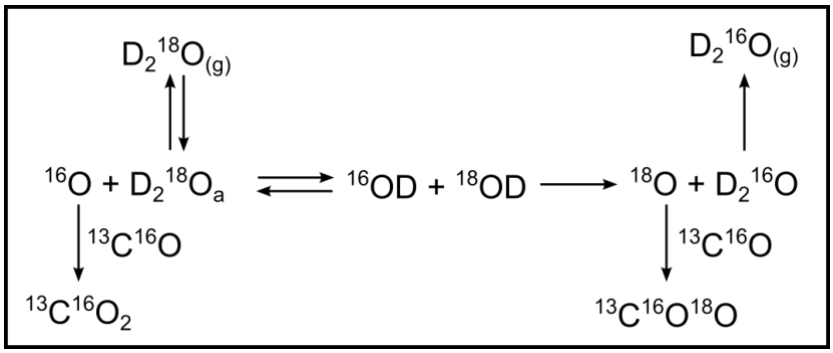

Scheme 1 – Reaction scenario of an oxygen atom with water, leading to the formation of two hydroxyls and the isotope exchange followed by the evolution of both $^{13}C^{16}O_2$ and $^{13}C^{16}O^{18}O$ isotopomers.

The Brönsted-base character of the adsorbed atomic oxygen is sufficient to abstract a hydrogen atom from an adsorbed water molecule to form two hydroxides on the surface with relatively small activation barriers calculated to range from 0.11 eV for the Au(111)[155,160] to 0.23 eV for the Au(321)[152] surfaces using DFT calculations. The reaction towards the two hydroxyls was found to be endothermic by 0.05 eV and 0.11 eV for the Au(111) and the Au(321) surfaces, respectively. The low barrier in both directions allows for a very rapid and reversible reaction as represented in **Scheme 1**. Calculations have also shown

that hydroxyl groups are mobile species with a barrier for diffusion of 0.19 eV on Au(111)[155]. However, this barrier needs to be compared to the barrier of the back reaction, which is calculated to be somewhat smaller but comparable. This results in a complex kinetic scenario, which would need kinetic modelling to deduce the transient concentrations. Such a modelling is, however, difficult as the result depends very critically on the precision of the different energies and the precision of DFT is usually not good enough to achieve “chemical accuracy”. Assuming that the calculated energies equal the free enthalpies of the reaction, this would lead to an equilibrium constant of about $1.0 \cdot 10^{-2}$ – 0.05 eV for Au(111) and $6.1 \cdot 10^{-3}$ – 0.11 eV for Au(321) at 250 K. As the transient concentration of the oxygen atoms as well as water are rather small, the concentration of the hydroxyl groups will be even smaller. However, the exchange reaction is very facile and can kinetically compete with CO oxidation despite the low transient concentrations due to the irreversible nature of the reaction creating the ^{18}O atoms and its low activation energy.

The analysis of the initial reactivity confirms the kinetic competition of an isotope exchange reaction between $D_2{}^{18}O + {}^{16}O_{ads}$ yielding two hydroxyl groups on Au(332) and CO oxidation. While this picture is sufficient to understand the initial reactivity, it is not possible to understand the more complex kinetics at later stages of the pulses using this simple scenario. To further elucidate the role of water for CO oxidation, the transient reaction kinetics will be discussed in more detail in the following section.

8.2 Transient Kinetics

While the differences in the initial CO_2 production rates were found to be basically constant in the presence of water, the transient kinetics of CO oxidation reflected in the pulse shapes depends significantly on water partial pressure and will be discussed in the following.

Single pulse profiles of $^{13}C^{16}O^{16}O$ and $^{13}C^{16}O^{18}O$ observed in the MB experiments shown in **Figure 8.1** are shown in **Figure 8.4**. For a direct

comparison of the changes in transient kinetics the pulses are normalized to maximum pulse height. As alluded to above, for low water pressure ($1.8 \cdot 10^{-7}$ mbar) as well as in the absence of water, a decrease in CO_2 formation rate is detected in the m/z = 45 channel. The m/z = 47 channel exhibits a slight decay at later stages of the pulse, as well. For the intermediate water pressure, a decrease of reactivity is clearly observed in the pulse shape of $^{13}C^{16}O^{18}O$, while the trace for $^{13}C^{16}O_2$ product is almost constant. At the highest water pressure, a stable CO_2 production is observed at the end of the O-pulse in both the $^{13}C^{16}O_2$ (m/z = 45) and $^{13}C^{16}O^{18}O$ (m/z = 47) channel. After closing the oxygen beam, the reaction drops towards the background under all conditions. The decrease is, however, slower than expected based on the characteristic time scale of the machine, which is in line with the consumption of remaining active oxygen species during this time period.

For both $^{13}C^{16}O_2$ and $^{13}C^{16}O^{18}O$ products, the fast onset (see **Figure 8.4** – solid red line) observed of the signal is predominately due to the direct reaction of CO with oxygen atoms present on the Au(332). As already discussed in **Chapter 7** CO oxidation will compete with surface diffusion of the O-atoms. Due to their thermodynamics stability as compared to the single O-atoms the diffusing atoms will tend to nucleate at appropriate sites such as step edges on the surface and from Au-O phases, whose reactivity towards CO oxidation is decreasing with increasing size[159]. However, theoretical investigations suggest that the initial stages of these Au-O phases, namely Au-O chains, show a considerable activity towards CO oxidation[161]. To this end, the slow increase (see **Figure 8.4** – dotted red line) of the CO_2 yield is interpreted to be the sum of the reactivity of the direct channel utilizing atomic oxygen and CO reactivity at the Au-O phases. The slow increase of the CO activity after the rapid rise within the first two seconds reflects the formation kinetics of these phases. With increasing size of the Au-O phases their reactivity drops, which leads to a deactivation of the system at later stages of the oxygen pulses. In turn, this interpretation implies that the flux of oxygen atoms added to the Au-O phases has to be higher than the loss due to CO oxidation; hence, there is also a kinetic competition in this reaction channel.

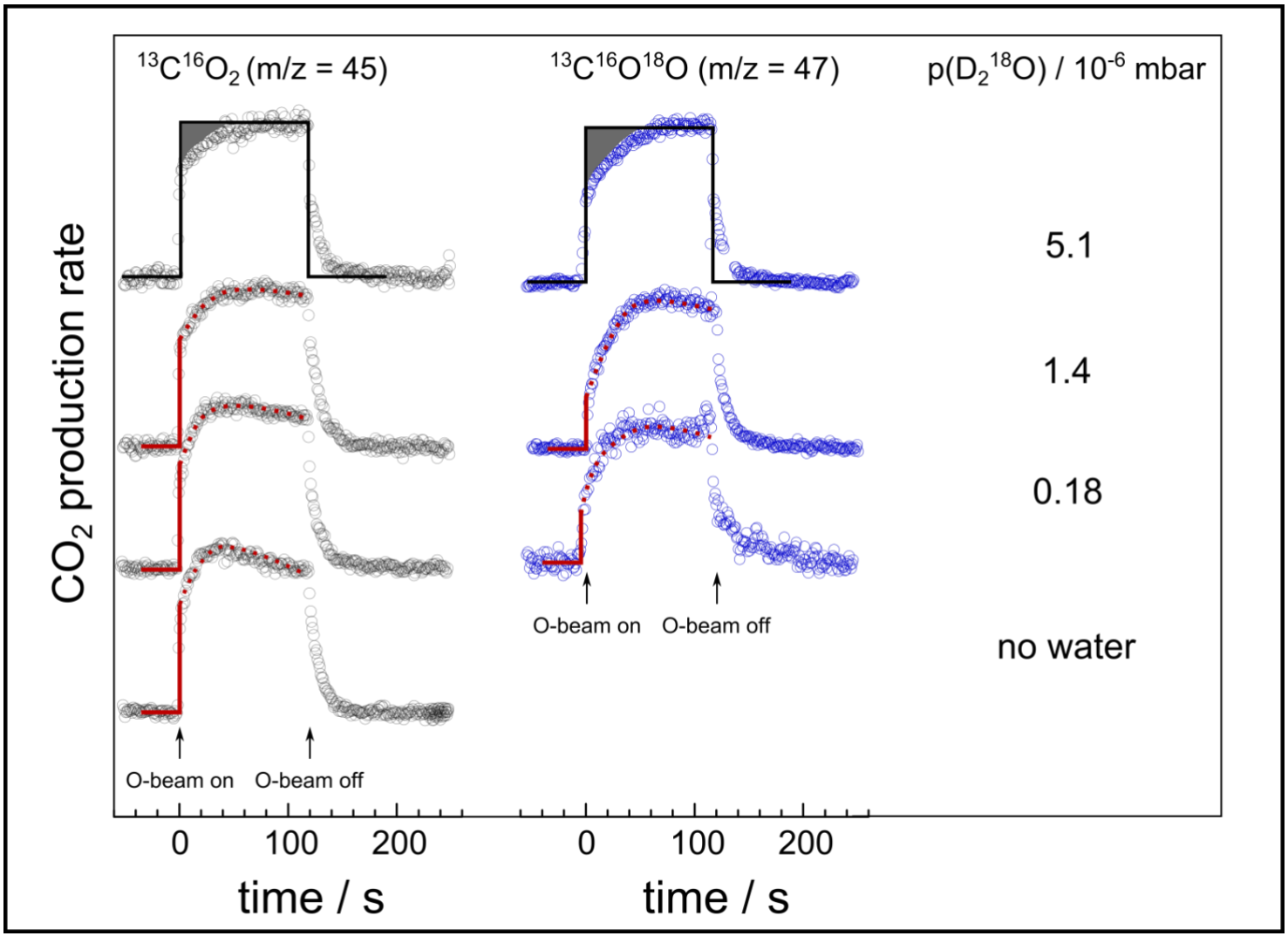

Figure 8.4: *Signals of transient $^{13}CO_2$ production rate at 250 K for different water pressures. The length of oxygen pulse is 120 s ($3.2 \cdot 10^{-8}$ mbar) and p(^{13}CO) = $2.4 \cdot 10^{-6}$ mbar. Fast and slow components are represented by solid and dotted red lines, respectively, constituting a guide for the eye. The black rectangles represent the ideal pulse shape and the hatched areas correspond to the oxygen present on the surface at steady state.*

At a water pressure of $1.4 \cdot 10^{-6}$ mbar (see **Figure 8.4**) the transient signals show an interesting aspect. At this pressure, the reactivity towards $^{13}C^{16}O_2$ becomes basically stable, while the isotope exchanged channel reveals a deactivation of the surface. Hence, the deactivation, which is associated with the formation of Au-O phases, is no longer observed in the direct reaction channel. This observation implies that the isotope exchange has to be complete for the Au-O phases under these conditions. In turn, the ratio of the rates between the isotope exchange reaction and CO oxidation has to increase rendering the isotope exchange more facile for the Au-O phases as compared to CO oxidation by O atoms.

At the highest water pressure, the reactivity towards both $^{13}C^{16}O_2$ and $^{13}C^{16}O^{18}O$ reaches stationary values. It is important to note, that the kinetics towards steady state is different for both reaction channels indicating that different reaction paths contribute to these products. Steady state is reached much later for the isotope exchanged channel, which is in line with the observation discussed above, which was indicating that CO oxidation utilizing the Au-O phases is predominantly yielding $^{13}C^{16}O^{18}O$. Hence, the kinetics of the exchanged channel towards the steady state can be interpreted as the kinetics towards a stationary Au-O phase distribution present at steady state.

The presence of a transient oxygen concentration in the steady state is readily deduced from the observed pulse shape. In steady state the amount of the total rate of CO_2 production has to equal the flux of oxygen atoms sticking to the surface. As the latter is a perfect rectangular shaped pulse (see black rectangles in the top traces of **Figure 8.4**) with the height corresponding to the steady state reactivity of CO_2, the sum of the hashed areas in **Figure 8.4** corresponds to the amount of oxygen present under steady state conditions used here. Integrating the area of the rectangles and the area underneath the experimental pulses and using the total flux of oxygen atoms of $2.6 \cdot 10^{14}$ atoms$\cdot$cm^{-2}, the difference between the two areas corresponds to $2.8 \cdot 10^{13}$ atoms$\cdot$cm^{-2} (0.02 ML) present under steady state conditions. This indicates that, in the presence of water almost 90% of the oxygen atoms were consumed, while for the CO oxidation reaction in the absence of water (see **Chapter 7**) only 75% of oxygen atoms were reacting off. While these numbers depend on

the pulse length and can hence not be interpreted quantitatively further, this result shows an enhanced reactivity of the system in the presence of water in the sense that it helps to prevent a deactivation of the system due to the formation of Au-O phases.

The ability of water to utilize oxygen otherwise stored in Au-O phases and subsequently leading to a deactivation of the surface is in line with the beneficial role of water found for nanoporous gold catalysts. Running CO oxidation on np-Au oftentimes results in a deactivation of the system at prolonged times on stream, which is associated with the accumulation of oxygen in the system. Exposing such deactivated np-Au to a CO oxidation feed containing water was shown to result in a reactivation of the systems[162]. In addition, similar effects with respect to the transient kinetics found on the model systems were also observed for np-Au. While the system deactivates under dry CO/O_2 feed conditions a stable steady state reactivity can be reached if water is added to the feed[162]. To this end, the results on the model surface presented here perfectly match the observations on the real catalyst suggesting that the underlying mechanism also apply for the np-Au.

9. Summary

Within this thesis a new molecular beam apparatus was set up, which has been specifically designed to investigate reaction kinetics of catalytic reaction on single crystal surfaces under well-defined conditions. The corresponding UHV apparatus is divided into two parts: a chamber for sample preparation and a scattering chamber used for the characterization of surface reactivity. The former one is equipped with standard surface characterization and preparation tools namely sputter gun, electron beam evaporator, quartz-microbalance, low-energy electron diffraction and an Auger electron spectrometer. The scattering chamber consists of two crossed effusive molecular beams and allows for *in-situ* infrared-spectroscopy of the sample placed at the crossing point of the molecular beams. While IR spectroscopy allows to monitor the evolution of surface species during reactions, the reactivity itself is monitored by analysing the gas-phase composition using a quadrupole mass spectrometer. The principle concept of the apparatus follows the lines described in literature, however, in this machine an effusive atomic oxygen source, which was operated as a molecular beam, was integrated for the first time into a molecular beam apparatus. The aim of this development was to study the transient as well as steady state reactivity of oxidation reactions which are impossible to study under UHV conditions due to the low probability of oxygen activation at these pressures. To this end CO oxidation on a single crystalline Au-surface was chosen as a test reaction.

A quantitative evaluation of the results requires a proper alignment and characterization of the different components. Using a movable stagnation flow monitor the beam profiles as well as the dependence of the flux on the inlet pressure of the glass capillary array used to form the effusive beam could be determined. After proper alignment, the flux of educts varies by about 20% over the entire crystal surface, which ensures homogeneous reaction conditions over the entire surface. Moreover, the educt flux depends linearly on inlet pressure below about 0.6 mbar, which corresponds to a flux of $1.5 \cdot 10^{15}$ molecules$\cdot cm^{-2}s^{-1}$. For higher inlet pressures, up to 1 mbar slight deviation of

the linear dependence are observed, however, the flux raises to about $2 \cdot 10^{15}$ molecules•$cm^{-2}s^{-1}$

To elucidate the nature of CO IR bands observed *in-situ* during CO oxidation, infrared spectra of ^{13}CO were taken on pristine and O precovered Au(332) surface. If ^{13}CO is adsorbed on Au(332) under UHV conditions at 100 K, two lines can be discerned at low coverage, which were assigned to CO adsorbed at step and kink sites of the Au(332) surface. With increasing coverage both signals merge and the spectrum exhibit only one resonance at about 2065 cm^{-1}, which is due to the different contribution of the dipolar coupling for both species as extracted from isotope dilution experiments. The temperature series of IR spectra of ^{13}CO taken under isobaric conditions showed a single adsorption band found at 2075 cm^{-1} for an IR intensity, hence, a CO coverage, comparable to the saturation coverage at 100 K. The shift of the signal by 10 cm^{-1} under isobaric conditions to higher frequency proves a different environment of the CO molecules at the different temperatures. The latter can be interpreted as a variation of the populated adsorption sites. For the O precovered Au(332) surface IR spectroscopy reveals two CO stretching bands blue-shifted with respect to the one on the pristine Au(332) surface, which can be attributed to two adsorption sites created by the deposition of oxygen on the surface. While the blue-shift of the stretching frequency is well in line with expectations, it these sites, although small in number, were found to exhibit a higher CO binding energy than the clean Au surface, which is not typically observed for late transition metals. However, there are indications from theoretical calculations that sites with higher CO binding energy exist on an oxygen precovered Au surface. Although at present these calculations are at variance with the observed stability of these sites with respect to CO oxidation and can, hence, not explain the observed IR lines.

The CO oxidation was investigated on the Au(332) as a function of oxygen atom flux and temperature. At 200 K a deactivation of the surface towards CO oxidation is found in pulsed molecular beam studies. The deactivation is considerably faster if the oxygen atom flux is increased. The latter is accompanied with a deposition of oxygen on the surface as verified by Auger

spectroscopy. This result implies that under the experimental conditions the oxidation of CO with oxygen atoms impinging on the Au surface competes with diffusion of O-atom to nucleate into thermodynamically more stable Au-O phases. The latter are responsible for a deactivation of the system, which is in line with expectations based on results described in literature. Even though the activity of the Au surface drops significantly after deposition of oxygen atoms, the oxygen covered surface still has CO oxidation activity, which is higher than the stainless-steel chamber.

At higher temperature (220 – 300 K) the surface was found to show a more pronounced deactivation during the oxygen pulses as compared to 200 K. This suggests that the formation of Au-O phases is more facile under these conditions, which implies that the balance between oxygen atom diffusion leading to the formation of Au-O phases and reaction with CO is shifted towards diffusion. The latter is well in line with expectation based on the IR results, which show a significant decrease of the transient CO concentration on the surface, and the high desorption temperature of oxygen atoms (T > 500 K). Despite the deactivation during the pulses the system exhibits a reproducible pulse to pulse behaviour. This reproducibility allows to quantify the amount of oxygen being stored on the surface during the oxygen pulses. From this analysis, it can be concluded that already 0.05 ML of oxygen adsorbed on the surface within Au-O phases results in a decrease of the reactivity by about 10%.

Another notable aspect of low-temperature CO oxidation is that the addition of water in the feed stream is believed to have a beneficial effect on the reaction. From the systematic study preformed within this thesis it could show that the initial reactivity of the system, which is determined by the reaction of CO with oxygen atoms is not altered by the presence of water. The experiments clearly show the reaction of water with the oxygen atoms present at the surface, however, no indication for a change in the reaction mechanism could be found. The observed of isotope exchange reactions between oxygen atoms and water points to a very facile equilibrium reaction between water and oxygen atoms towards two hydroxyls, which can kinetically compete with CO oxidation.

With increasing water pressure the system reaches steady state conditions, which confirms the ability of water to utilize oxygen otherwise stored in Au-O phases subsequently leading to a deactivation of the system. Under

steady state conditions the molecular beam approach allows to quantify the transient oxygen coverage present at steady state, which was found to be about 0.02 ML. This indicates that, in the presence of water almost 90% of the oxygen atoms were reacting off, while for the CO oxidation reaction in the absence of water only 75% of oxygen atoms were consumed under otherwise identical conditions. These results have confirmed that the presence of water during CO oxidation helps to prevent a deactivation of the surface due to the formation of Au-O phases.

The Au(332) surface investigated here was chosen to serve as a model system for np-Au, which was found to be a suitable catalyst for low-temperature CO oxidation using molecular oxygen as the oxidation agent. While the experiments described here are not able to shed light on important questions such as the mechanism of oxygen activation, the results observed here show striking similarities with the behaviour of np-Au. Under dry CO oxidation conditions np-Au catalysts often exhibit a rather similar behaviour of the reactivity found here. Although the corresponding time scales are largely different the system show in increase in activity with time on stream, however, the activity goes through a maximum and the system deactivates at later times. Moreover, by adding water to the CO oxidation feed, the np-Au starts to show steady state reactivity, which exactly parallels the behaviour observed on the model system studied here. Hence, it is suggested that the reason for the deactivation of the np-Au is the unfavourable competition between CO oxidation of the activated oxygen species, which are most likely oxygen atoms and their diffusion towards nucleation sites for Au-O phases. The growth of these phases will lead to a deactivation of the system at prolonged time on stream. Water, however, was shown to allow a utilization of oxygen stored in such Au-O phases, which would otherwise lead to deactivation. To this end, the results of on the model system under UHV conditions obtained in this thesis provide an experiment based explanation for an important process in a real high-performance catalyst underpinning the importance of surface science experiments for the understanding of heterogeneous catalysis.

References

1. Scoles, G. *Atomic and Molecular Beam Methods*. (Oxford University Press Inc, 1988).
2. Schauermann, S. Structure Sensitive Surface Reactions on Model Catalysts: Molecular Beam Studies of Methanol and NO Dissociation on Supported Pd Nanoparticles. (Humboldt-Universität zu Berlin, 2005).
3. Griffiths, P. R., Haseth, J. A. D. & Winefordner, J. D. *Fourier Transform Infrared Spectrometry*. (Wiley John + Sons, 2007).
4. Libuda, J., Meusel, I., Hartmann, J. & Freund, H.-J. A molecular beam/surface spectroscopy apparatus for the study of reactions on complex model catalysts. *Rev. Sci. Instrum.* **71,** 4395–4408 (2000).
5. Wang, J. *et al.* Formation, Migration, and Reactivity of Au–CO Complexes on Gold Surfaces. *J. Am. Chem. Soc.* **138,** 1518–1526 (2016).
6. Ertl, G., Knözinger, H., Schüth, F. & Weitkamp, J. *Handbook of Heterogeneous Catalysis: 8 Volumes*. (Wiley-VCH, 2008).
7. Huang, W., Sun, G. & Cao, T. Surface chemistry of group IB metals and related oxides. *Chem. Soc. Rev.* **46,** 1977–2000 (2017).
8. Haruta, M., Kobayashi, T., Sano, H. & Yamada, N. Novel Gold Catalysts for the Oxidation of Carbon Monoxide at a Temperature far Below 0 °C. *Chem. Lett.* **16,** 405–408 (1987).
9. Stangland, E. E., Stavens, K. B., Andres, R. P. & Delgass, W. N. Characterization of Gold–Titania Catalysts via Oxidation of Propylene to Propylene Oxide. *J. Catal.* **191,** 332–347 (2000).
10. Hayashi, T., Tanaka, K. & Haruta, M. Selective Vapor-Phase Epoxidation of Propylene over Au/TiO_2Catalysts in the Presence of Oxygen and Hydrogen. *J. Catal.* **178,** 566–575 (1998).
11. Wittstock, A., Zielasek, V., Biener, J., Friend, C. M. & Bäumer, M. Nanoporous Gold Catalysts for Selective Gas-Phase Oxidative Coupling of Methanol at Low Temperature. *Science* **327,** 319–322 (2010).
12. Xu, B., Liu, X., Haubrich, J. & Friend, C. M. Vapour-phase gold-surface-mediated coupling of aldehydes with methanol. *Nat. Chem.* **2,** 61–65 (2010).

13. Liu, Z.-P., Jenkins, S. J. & King, D. A. Origin and Activity of Oxidized Gold in Water-Gas-Shift Catalysis. *Phys. Rev. Lett.* **94,** 196102 (2005).
14. Fu, Q., Saltsburg, H. & Flytzani-Stephanopoulos, M. Active Nonmetallic Au and Pt Species on Ceria-Based Water-Gas Shift Catalysts. *Science* **301,** 935–938 (2003).
15. Senanayake, S. D. *et al.* Interaction of CO with OH on Au(111): HCOO, CO_3, and HOCO as Key Intermediates in the Water-Gas Shift Reaction. *J. Phys. Chem. C* **113,** 19536–19544 (2009).
16. Ueda, A. & Haruta, M. Nitric Oxide Reduction with Hydrogen, Carbon Monoxide, and Hydrocarbons over Gold Catalysts. *Gold Bull.* **32,** 3–11 (1999).
17. Xu, C. *et al.* Low Temperature CO Oxidation over Unsupported Nanoporous Gold. *J. Am. Chem. Soc.* **129,** 42–43 (2007).
18. Jia, C. *et al.* Enhanced Photoelectrocatalytic Activity of Methanol Oxidation on TiO_2-Decorated Nanoporous Gold. *J. Phys. Chem. C* **113,** 16138–16143 (2009).
19. Lopez, N. *et al.* On the origin of the catalytic activity of gold nanoparticles for low-temperature CO oxidation. *J. Catal.* **223,** 232–235 (2004).
20. Wang, L. C., Jin, H. J., Widmann, D., Weissmüller, J. & Behm, R. J. Dynamic studies of CO oxidation on nanoporous Au using a TAP reactor. *J. Catal.* **278,** 219–227 (2011).
21. Valden, M., Lai, X. & Goodman, D. W. Onset of Catalytic Activity of Gold Clusters on Titania with the Appearance of Nonmetallic Properties. *Science* **281,** 1647–1650 (1998).
22. Catherine, L. & Olivier, P. *Gold Nanoparticles For Physics, Chemistry And Biology*. (World Scientific, 2012).
23. Lang, X. Y. *et al.* Novel Nanoporous Au−Pd Alloy with High Catalytic Activity and Excellent Electrochemical Stability. *J. Phys. Chem. C* **114,** 2600–2603 (2010).
24. Wittstock, A., Wichmann, A. & Bäumer, M. Nanoporous Gold as a Platform for a Building Block Catalyst. *ACS Catal.* **2,** 2199–2215 (2012).
25. Wittstock, A., Biener, J. & Bäumer, M. Nanoporous gold: a new material for catalytic and sensor applications. *Phys. Chem. Chem. Phys.* **12,** 12919–12930 (2010).

26. Erlebacher, J., Aziz, M. J., Karma, A., Dimitrov, N. & Sieradzki, K. Evolution of nanoporosity in dealloying. *Nature* **410,** 450 (2001).
27. Seker, E., Reed, M. L. & Begley, M. R. Nanoporous Gold: Fabrication, Characterization, and Applications. *Materials* **2,** 2188–2215 (2009).
28. Biener, J. *et al.* Surface-chemistry-driven actuation in nanoporous gold. *Nat. Mater.* **8,** 47–51 (2009).
29. Zielasek, V. *et al.* Gold Catalysts: Nanoporous Gold Foams. *Angew. Chem. Int. Ed.* **45,** 8241–8244 (2006).
30. Fujita, T., Qian, L.-H., Inoke, K., Erlebacher, J. & Chen, M.-W. Three-dimensional morphology of nanoporous gold. *Appl. Phys. Lett.* **92,** 251902 (2008).
31. Rösner, H., Parida, S., Kramer, D., Volkert, C. A. & Weissmüller, J. Reconstructing a Nanoporous Metal in Three Dimensions: An Electron Tomography Study of Dealloyed Gold Leaf. *Adv. Eng. Mater.* **9,** 535–541 (2007).
32. Hvolbæk, B. *et al.* Catalytic activity of Au nanoparticles. *Nano Today* **2,** 14–18 (2007).
33. Lemire, C., Meyer, R., Shaikhutdinov, S. & Freund, H.-J. Do Quantum Size Effects Control CO Adsorption on Gold Nanoparticles? *Angew. Chem. Int. Ed.* **43,** 118–121 (2004).
34. Molina, L. M. & Hammer, B. Theoretical study of CO oxidation on Au nanoparticles supported by MgO(100). *Phys. Rev. B* **69,** 155424 (2004).
35. Boudart, M. Turnover Rates in Heterogeneous Catalysis. *Chem. Rev.* **95,** 661–666 (1995).
36. Daté, M., Okumura, M., Tsubota, S. & Haruta, M. Vital Role of Moisture in the Catalytic Activity of Supported Gold Nanoparticles. *Angew. Chem. Int. Ed.* **43,** 2129–2132 (2004).
37. Kim, T. S., Gong, J., Ojifinni, R. A., White, J. M. & Mullins, C. B. Water Activated by Atomic Oxygen on Au(111) to Oxidize CO at Low Temperatures. *J. Am. Chem. Soc.* **128,** 6282–6283 (2006).
38. Mullen, G. M. & Mullins, C. B. Water's place in Au catalysis. *Science* **345,** 1564–1565 (2014).

39. Xu, B., Liu, X., Haubrich, J., Madix, R. J. & Friend, C. M. Selectivity Control in Gold-Mediated Esterification of Methanol. *Angew. Chem. Int. Ed.* **48,** 4206–4209 (2009).
40. Biener, J., Biener, M. M., Madix, R. J. & Friend, C. M. Nanoporous Gold: Understanding the Origin of the Reactivity of a 21st Century Catalyst Made by Pre-Columbian Technology. *ACS Catal.* **5,** 6263–6270 (2015).
41. Libuda, J. & Freund, H.-J. Molecular beam experiments on model catalysts. *Surf. Sci. Rep.* **57,** 157–298 (2005).
42. Zaera, F. Use of molecular beams for kinetic measurements of chemical reactions on solid surfaces. *Surf. Sci. Rep.* **72,** 59–104 (2017).
43. Kisliuk, P. The sticking probabilities of gases chemisorbed on the surfaces of solids. *J. Phys. Chem. Solids* **3,** 95–101 (1957).
44. Somorjai, G. A. & Li, Y. *Introduction to Surface Chemistry and Catalysis*. (John Wiley & Sons, 2010).
45. Chuikov, B. A., Dvurechenskikh, V. V., Osovskii, V. D., Ptushinskii, Y. G. & Sukretnyi, V. G. Adsorption of H_2 and D_2 on W(111) and W(110) surfaces at low temperatures (down to 5 K). *Surf. Sci.* **285,** 75–80 (1993).
46. Schmidt, K. J. & Christmann, K. The adsorption of xenon on a ruthenium(10$\bar{1}$0) surface. *Surf. Sci.* **492,** 167–184 (2001).
47. Saliba, N., Parker, D. H. & Koel, B. E. Adsorption of oxygen on Au(111) by exposure to ozone. *Surf. Sci.* **410,** 270–282 (1998).
48. Böttcher, S. *et al.* Adsorption of Water and Ammonia on Graphene: Evidence for Chemisorption from X-ray Absorption Spectra. *J. Phys. Chem. Lett.* **8,** 3668–3672 (2017).
49. Barker, J. A. & Auerbach, D. J. Gas—surface interactions and dynamics; Thermal energy atomic and molecular beam studies. *Surf. Sci. Rep.* **4,** 1–99 (1984).
50. Bowker, M. The Role of Precursor States in Adsorption, Surface Reactions and Catalysis. *Top. Catal.* **59,** 663–670 (2016).
51. Rettner, C. T., Auerbach, D. J., Tully, J. C. & Kleyn, A. W. Chemical Dynamics at the Gas−Surface Interface. *J. Phys. Chem.* **100,** 13021–13033 (1996).

52. Chang, H.-C. & Weinberg, W. H. An analysis of modulated molecular beam mass spectrometry applied to coupled diffusion and chemical reaction. *Surf. Sci.* **65,** 153–164 (1977).
53. Cassuto, A. & King, D. A. Rate expressions for adsorption and desorption kinetics with precursor states and lateral interactions. *Surf. Sci.* **102,** 388–404 (1981).
54. D'Evelyn, M. P. & Madix, R. J. Reactive scattering from solid surfaces. *Surf. Sci. Rep.* **3,** 413–495 (1983).
55. Arumainayagam, C. R. & Madix, R. J. Molecular beam studies of gas-surface collision dynamics. *Prog. Surf. Sci.* **38,** 1–102 (1991).
56. Chabal, Y. J. Surface infrared spectroscopy. *Surf. Sci. Rep.* **8,** 211–357 (1988).
57. Eischens, R. P., Francis, S. A. & Pliskin, W. A. The Effect of Surface Coverage on the Spectra of Chemisorbed CO. *J. Phys. Chem.* **60,** 194–201 (1956).
58. Niemantsverdriet, J. W. *Spectroscopy in Catalysis: An Introduction*. (Wiley-VCH Verlag GmbH & Co. KGaA, 2007).
59. Atkins, P. W. & Friedman, R. S. *Molecular Quantum Mechanics*. (Oxford University Press, 2010).
60. Martin, A. E. *Infrared Interferometric Spectrometers: Vol.8: Vibrational Spectra and Structure*. (Elsevier Science Ltd, 1980).
61. Pedrotti, F. L., Pedrotti, L. M. & Pedrotti, L. S. *Introduction to Optics*. (Pearson Education Limited, 2013).
62. Grimley, T. B. The Normal Mode Frequencies of Chemisorbed Atoms and Molecules. *Proc. Phys. Soc.* **79,** 1203 (1962).
63. Blyholder, G. Molecular Orbital View of Chemisorbed Carbon Monoxide. *J. Phys. Chem.* **68,** 2772–2777 (1964).
64. Blyholder, G. CNDO model of carbon monoxide chemisorbed on nickel. *J. Phys. Chem.* **79,** 756–761 (1975).
65. Mahan, G. D. & Lucas, A. A. Collective vibrational modes of adsorbed CO. *J. Chem. Phys.* **68,** 1344–1348 (1978).
66. Scheffler, M. The influence of lateral interactions on the vibrational spectrum of adsorbed CO. *Surf. Sci.* **81,** 562–570 (1979).

67. Hollins, P. & Pritchard, J. Infrared studies of chemisorbed layers on single crystals. *Prog. Surf. Sci.* **19,** 275–349 (1985).
68. Moskovits, M. & Hülse, J. E. Frequency shifts in the spectra of molecules adsorbed on metals, with emphasis on the infrared spectrum of adsorbed CO. *Surf. Sci.* **78,** 397–418 (1978).
69. Woodruff, D. P., Hayden, B. E., Prince, K. & Bradshaw, A. M. Dipole coupling and chemical shifts in IRAS of CO adsorbed on Cu(110). *Surf. Sci.* **123,** 397–412 (1982).
70. Dumas, P., Tobin, R. G. & Richards, P. L. Study of adsorption states and interactions of CO on evaporated noble metal surfaces by infrared absorption spectroscopy. *Surf. Sci.* **171,** 579–599 (1986).
71. Duckworth, H. E., Barber, R. C. & Venkatasubramanian, V. S. *Mass Spectroscopy*. (Cambridge University Press, 1986).
72. Gross, J. H. *Mass Spectrometry: A Textbook*. (Springer, 2017).
73. Hoffmann, E. D. *Mass Spectrometry Third Edition: Principles and Applications*. (Wiley-Interscience, 2007).
74. March, R. & Hughes, R. *Quadrupole Storage Mass Spectrometry*. (John Wiley & Sons Inc, 1989).
75. Tschersich, K. G. & von Bonin, V. Formation of an atomic hydrogen beam by a hot capillary. *J. Appl. Phys.* **84,** 4065–4070 (1998).
76. Tschersich, K. G. Intensity of a source of atomic hydrogen based on a hot capillary. *J. Appl. Phys.* **87,** 2565–2573 (2000).
77. Palmberg, P. W. *Handbook of Auger electron spectroscopy : a reference book of standard data for identification and interpretation of Auger electron spectroscopy data*. (Physical Electronics Industries, 1972).
78. Cathrine, B., Fargues, D., Alnot, M. & Ehrhardt, J. J. A photoemission study of the adsorption of the first and the second layer of xenon on Pt(332). *Surf. Sci.* **259,** 162–172 (1991).
79. Rhead, G. E. Surface defects. *Surf. Sci.* **68,** 20–38 (1977).
80. Perdereau, J. & Rhead, G. E. LEED studies of adsorption on vicinal copper surfaces. *Surf. Sci.* **24,** 555–571 (1971).
81. Prieto, M. J., Carbonio, E. A., Fatayer, S., Landers, R. & Siervo, A. de. Electronic and structural study of Pt-modified Au vicinal surfaces: a model

system for Pt–Au catalysts. *Phys. Chem. Chem. Phys.* **16,** 13329–13339 (2014).

82. Hayden, B. E., Kretzschmar, K., Bradshaw, A. M. & Greenler, R. G. An infrared study of the adsorption of CO on a stepped platinum surface. *Surf. Sci.* **149,** 394–406 (1985).
83. Hollins, P., Davies, K. J. & Pritchard, J. Infrared spectra of CO chemisorbed on a surface vicinal to Cu(110): The influence of defect sites. *Surf. Sci.* **138,** 75–83 (1984).
84. Hollins, P. & Pritchard, J. Infrared studies of chemisorbed layers on single crystals. *Prog. Surf. Sci.* **19,** 275–349 (1985).
85. Rank, D. H., Skorinko, G., Eastman, D. P. & Wiggins, T. A. Highly precise wavelengths in the infrared. *J. Mol. Spectrosc.* **4,** 518–533 (1960).
86. Kim, J., Samano, E. & Koel, B. E. CO Adsorption and Reaction on Clean and Oxygen-Covered Au(211) Surfaces. *J. Phys. Chem. B* **110,** 17512–17517 (2006).
87. Pischel, J. & Pucci, A. Low-Temperature Adsorption of Carbon Monoxide on Gold Surfaces: IR Spectroscopy Uncovers Different Adsorption States on Pristine and Rough Au(111). *J. Phys. Chem. C* **119,** 18340–18351 (2015).
88. Pászti, Z. *et al.* Interaction of Carbon Monoxide with Au(111) Modified by Ion Bombardment: A Surface Spectroscopy Study under Elevated Pressure. *Langmuir* **26,** 16312–16324 (2010).
89. France, J. & Hollins, P. Interactions of CO molecules adsorbed on gold. *J. Electron Spectrosc. Relat. Phenom.* **64,** 251–258 (1993).
90. Nakamura, I., Takahashi, A. & Fujitani, T. Selective Dissociation of O_3 and Adsorption of CO on Various Au Single Crystal Surfaces. *Catal. Lett.* **129,** 400–403 (2009).
91. Ruggiero, C. & Hollins, P. Adsorption of carbon monoxide on the gold(332) surface. *J. Chem. Soc., Faraday Trans.* **92,** 4829–4834 (1996).
92. Gottfried, J. M., Schmidt, K. J., Schroeder, S. L. M. & Christmann, K. Adsorption of carbon monoxide on Au(110)-(1×2). *Surf. Sci.* **536,** 206–224 (2003).
93. Weststrate, C. J. *et al.* CO adsorption on Au(310) and Au(321): 6-Fold coordinated gold atoms. *Surf. Sci.* **603,** 2152–2157 (2009).

94. Mihaylov, M., Knözinger, H., Hadjiivanov, K. & Gates, B. C. Characterization of the Oxidation States of Supported Gold Species by IR Spectroscopy of Adsorbed CO. *Chem. Ing. Tech.* **79,** 795–806 (2007).
95. Lari, G. M., Nowicka, E., Morgan, D. J., Kondrat, S. A. & Hutchings, G. J. The use of carbon monoxide as a probe molecule in spectroscopic studies for determination of exposed gold sites on TiO_2. *Phys. Chem. Chem. Phys.* **17,** 23236–23244 (2015).
96. Villa, A. *et al.* Characterisation of gold catalysts. *Chem. Soc. Rev.* **45,** 4953–4994 (2016).
97. Yim, W.-L. *et al.* Universal Phenomena of CO Adsorption on Gold Surfaces with Low-Coordinated Sites. *J. Phys. Chem. C* **111,** 445–451 (2007).
98. Röhe, S. *et al.* CO oxidation on nanoporous gold: A combined TPD and XPS study of active catalysts. *Surf. Sci.* **609,** 106–112 (2013).
99. Barth, J. V., Brune, H., Ertl, G. & Behm, R. J. Scanning tunneling microscopy observations on the reconstructed Au(111) surface: Atomic structure, long-range superstructure, rotational domains, and surface defects. *Phys. Rev. B* **42,** 9307–9318 (1990).
100. Prieto, M. J., Carbonio, E. A., Landers, R. & de Siervo, A. Structural and electronic characterization of Co nanostructures on Au(332). *Surf. Sci.* **617,** 87–93 (2013).
101. Hollins, P. & Pritchard, J. Interactions of CO molecules adsorbed on Cu(111). *Surf. Sci.* **89,** 486–495 (1979).
102. Ruggiero, C. & Hollins, P. Interaction of CO molecules with the Au(332) surface. *Surf. Sci.* **377,** 583–586 (1997).
103. Meyer, R. *et al.* CO adsorption and thermal stability of Pd deposited on a thin FeO(111) film. *Surf. Sci.* **586,** 174–182 (2005).
104. Ferstl, P. *et al.* Adsorption and Activation of CO on Co_3O_4(111) Thin Films. *J. Phys. Chem. C* **119,** 16688–16699 (2015).
105. Kim, C. M., Yi, C.-W. & Goodman, D. W. CO−NO and CO−O_2 Interactions on Cu(100) between 25 and 200 K Studied with Infrared Reflection Absorption Spectroscopy. *J. Phys. Chem. B* **109,** 1891–1895 (2005).
106. Bauer, T. *et al.* Ligand Effects at Ionic Liquid-Modified Interfaces: Coadsorption of [C2C1Im][OTf] and CO on Pd(111). *J. Phys. Chem. C* **120,** 4453–4465 (2016).

107. Huheey, J., E. & Keiter, R. *Inorganic Chemistry : Principles of Structure and Reactivity*.
108. Moskaleva, L. V., Zielasek, V., Klüner, T., Neyman, K. M. & Bäumer, M. CO oxidation by co-adsorbed atomic O on the Au(321) surface with Ag impurities: A mechanistic study from first-principles calculations. *Chem. Phys. Lett.* **525–526,** 87–91 (2012).
109. Moskaleva, L. V., Weiss, T., Klüner, T. & Bäumer, M. Chemisorbed Oxygen on the Au(321) Surface Alloyed with Silver: A First-Principles Investigation. *J. Phys. Chem. C* **119,** 9215–9226 (2015).
110. Ertl, G. Reactions at well-defined surfaces. *Surf. Sci.* **299-300,** 742–754 (1994).
111. Yeo, Y. Y., Vattuone, L. & King, D. A. Calorimetric heats for CO and oxygen adsorption and for the catalytic CO oxidation reaction on Pt{111}. *J. Chem. Phys.* **106,** 392–401 (1997).
112. Berlowitz, P. J., Peden, C. H. F. & Goodman, D. W. Kinetics of carbon monoxide oxidation on single-crystal palladium, platinum, and iridium. *J. Phys. Chem.* **92,** 5213–5221 (1988).
113. Over, H. *et al.* Atomic-Scale Structure and Catalytic Reactivity of the RuO_2(110) Surface. *Science* **287,** 1474–1476 (2000).
114. Hendriksen, B. L. M. & Frenken, J. W. M. CO Oxidation on Pt(110): Scanning Tunneling Microscopy Inside a High-Pressure Flow Reactor. *Phys. Rev. Lett.* **89,** 046101 (2002).
115. Daniell, W., Weingand, T. & Knözinger, H. Redox properties of Re_2O_7/Al_2O_3 as investigated by FTIR spectroscopy of adsorbed CO. *J. Mol. Catal. Chem.* **204-205,** 519–526 (2003).
116. Duan, Z. & Henkelman, G. CO Oxidation on the Pd(111) Surface. *ACS Catal.* **4,** 3435–3443 (2014).
117. Ivanov, V. P., Boreskov, G. K., Savchenko, V. I., Egelhoff, W. F. & Weinberg, W. H. The CO oxidation reaction on the Ir(111) surface. *J. Catal.* **48,** 269–283 (1977).
118. Böttcher, A., Niehus, H., Schwegmann, S., Over, H. & Ertl, G. CO Oxidation Reaction over Oxygen-Rich Ru(0001) Surfaces. *J. Phys. Chem. B* **101,** 11185–11191 (1997).

119. Eren, B., Heine, C., Bluhm, H., Somorjai, G. A. & Salmeron, M. Catalyst Chemical State during CO Oxidation Reaction on Cu(111) Studied with Ambient-Pressure X-ray Photoelectron Spectroscopy and Near Edge X-ray Adsorption Fine Structure Spectroscopy. *J. Am. Chem. Soc.* **137,** 11186–11190 (2015).
120. Baker, T. A., Xu, B., Liu, X., Kaxiras, E. & Friend, C. M. Nature of Oxidation of the Au(111) Surface: Experimental and Theoretical Investigation. *J. Phys. Chem. C* **113,** 16561–16564 (2009).
121. Ron, H. & Rubinstein, I. Alkanethiol Monolayers on Preoxidized Gold. Encapsulation of Gold Oxide under an Organic Monolayer. *Langmuir* **10,** 4566–4573 (1994).
122. Koslowski, B. *et al.* Oxidation of preferentially (111)-oriented Au films in an oxygen plasma investigated by scanning tunneling microscopy and photoelectron spectroscopy. *Surf. Sci.* **475,** 1–10 (2001).
123. Pireaux, J. J. *et al.* Electron spectroscopic characterization of oxygen adsorption on gold surfaces. *Surf. Sci.* **141,** 211–220 (1984).
124. Wang, J. & Koel, B. E. Reactions of N2O4 with ice at low temperatures on the Au(111) surface. *Surf. Sci.* **436,** 15–28 (1999).
125. Canning, N. D. S., Outka, D. & Madix, R. J. The adsorption of oxygen on gold. *Surf. Sci.* **141,** 240–254 (1984).
126. Sault, A. G., Madix, R. J. & Campbell, C. T. Adsorption of oxygen and hydrogen on Au(110)-(1×2). *Surf. Sci.* **169,** 347–356 (1986).
127. Linsmeier, C. & Wanner, J. Reactions of oxygen atoms and molecules with Au, Be, and W surfaces. *Surf. Sci.* **454-456,** 305–309 (2000).
128. Outka, D. A. & Madix, R. J. The oxidation of carbon monoxide on the Au(110) surface. *Surf. Sci.* **179,** 351–360 (1987).
129. Michael Gottfried, J. & Christmann, K. Oxidation of carbon monoxide over Au(110)-(1×2). *Surf. Sci.* **566–568, Part 2,** 1112–1117 (2004).
130. Min, B. K., Alemozafar, A. R., Pinnaduwage, D., Deng, X. & Friend, C. M. Efficient CO Oxidation at Low Temperature on Au(111). *J. Phys. Chem. B* **110,** 19833–19838 (2006).
131. Ojifinni, R. A., Gong, J., Flaherty, D. W., Kim, T. S. & Mullins, C. B. Annealing Effect on Reactivity of Oxygen-Covered Au(111). *J. Phys. Chem. C* **113,** 9820–9825 (2009).

132. Samano, E., Kim, J. & Koel, B. E. Investigation of CO Oxidation Transient Kinetics on an Oxygen Pre-covered Au(211) Stepped Surface. *Catal. Lett.* **128,** 263–267 (2009).
133. Hiebel, F., Montemore, M. M., Kaxiras, E. & Friend, C. M. Direct visualization of quasi-ordered oxygen chain structures on Au(110)-(1×2). *Surf. Sci.* **650,** 5–10 (2016).
134. Baber, A. E. *et al.* Reactivity and Morphology of Oxygen-Modified Au Surfaces. *J. Phys. Chem. C* **116,** 18292–18299 (2012).
135. Liu, Z.-P., Hu, P. & Alavi, A. Catalytic Role of Gold in Gold-Based Catalysts: A Density Functional Theory Study on the CO Oxidation on Gold. *J. Am. Chem. Soc.* **124,** 14770–14779 (2002).
136. Broqvist, P., Molina, L. M., Grönbeck, H. & Hammer, B. Promoting and poisoning effects of Na and Cl coadsorption on CO oxidation over MgO-supported Au nanoparticles. *J. Catal.* **227,** 217–226 (2004).
137. Chen, Y., Crawford, P. & Hu, P. Recent Advances in Understanding CO Oxidation on Gold Nanoparticles Using Density Functional Theory. *Catal. Lett.* **119,** 21–28 (2007).
138. Fajín, J. L. C., Cordeiro, M. N. D. S. & Gomes, J. R. B. DFT study of the Au(321) surface reconstruction by consecutive deposition of oxygen atoms. *Surf. Sci.* **602,** 424–435 (2008).
139. Prestianni, A., Martorana, A., Ciofini, I., Labat, F. & Adamo, C. CO Oxidation on Cationic Gold Clusters: A Theoretical Study. *J. Phys. Chem. C* **112,** 18061–18066 (2008).
140. Su, H.-Y., Yang, M.-M., Bao, X.-H. & Li, W.-X. The Effect of Water on the CO Oxidation on Ag(111) and Au(111) Surfaces: A First-Principle Study. *J. Phys. Chem. C* **112,** 17303–17310 (2008).
141. Coquet, R., Howard, K. L. & Willock, D. J. Theory and simulation in heterogeneous gold catalysis. *Chem. Soc. Rev.* **37,** 2046–2076 (2008).
142. Fajín, J. L. C., Cordeiro, M. N. D. S. & Gomes, J. R. B. DFT Study of the CO Oxidation on the Au(321) Surface. *J. Phys. Chem. C* **112,** 17291–17302 (2008).
143. Gopinath, C. S. & Zaera, F. Transient Kinetics during the Isothermal Reduction of NO by CO on Rh(111) As Studied with Effusive Collimated Molecular Beams. *J. Phys. Chem. B* **104,** 3194–3203 (2000).

144. Libuda, J., Meusel, I., Hoffmann, J., Hartmann, J. & Freund, H.-J. Reaction kinetics on supported model catalysts: Molecular beam/in situ time-resolved infrared reflection absorption spectroscopy study of the CO oxidation on alumina supported Pd particles. *J. Vac. Sci. Technol. Vac. Surf. Films* **19,** 1516–1523 (2001).
145. Laurin, M. *et al.* Transient and steady state CO oxidation kinetics on nanolithographically prepared supported Pd model catalysts: Experiments and simulations. *J. Chem. Phys.* **123,** 054701 (2005).
146. Outka, D. A. & Madix, R. J. Broensted basicity of atomic oxygen on the gold(110) surface: reactions with methanol, acetylene, water, and ethylene. *J. Am. Chem. Soc.* **109,** 1708–1714 (1987).
147. Kay, B. D., Lykke, K. R., Creighton, J. R. & Ward, S. J. The influence of adsorbate–absorbate hydrogen bonding in molecular chemisorption: NH3, HF, and H2O on Au(111). *J. Chem. Phys.* **91,** 5120–5121 (1989).
148. Wu, Z., Jiang, Z., Jin, Y., Xiong, F. & Huang, W. Identification of Hydroxyl Groups on Au Surfaces Formed by $H_2O(a)+O(a)$ Reaction. *J. Phys. Chem. C* **118,** 26258–26263 (2014).
149. Van Spronsen, M. A. *et al.* Hydrophilic Interaction Between Low-Coordinated Au and Water: H_2O/Au(310) Studied with TPD and XPS. *J. Phys. Chem. C* **120,** 8693–8703 (2016).
150. Quiller, R. G. *et al.* Transient hydroxyl formation from water on oxygen-covered Au(111). *J. Chem. Phys.* **129,** 064702 (2008).
151. Ojifinni, R. A. *et al.* Water-Enhanced Low-Temperature CO Oxidation and Isotope Effects on Atomic Oxygen-Covered Au(111). *J. Am. Chem. Soc.* **130,** 6801–6812 (2008).
152. Moskaleva, L. V. Private Communication.
153. Vassilev, P. & Koper, M. T. M. Electrochemical Reduction of Oxygen on Gold Surfaces: A Density Functional Theory Study of Intermediates and Reaction Paths. *J. Phys. Chem. C* **111,** 2607–2613 (2007).
154. Chang, C.-R., Wang, Y.-G. & Li, J. Theoretical investigations of the catalytic role of water in propene epoxidation on gold nanoclusters: A hydroperoxyl-mediated pathway. *Nano Res.* **4,** 131–142 (2011).

155. Ojifinni, R. A. *et al.* Water-Enhanced Low-Temperature CO Oxidation and Isotope Effects on Atomic Oxygen-Covered Au(111). *J. Am. Chem. Soc.* **130,** 6801–6812 (2008).
156. Gong, J. *et al.* Low temperature CO oxidation on Au(111) and the role of adsorbed water. *Top. Catal.* **44,** 57–63 (2007).
157. Mullen, G. M., Gong, J., Yan, T., Pan, M. & Mullins, C. B. The Effects of Adsorbed Water on Gold Catalysis and Surface Chemistry. *Top. Catal.* **56,** 1499–1511 (2013).
158. Van Spronsen, M. A., Weststrate, K.-J. & Juurlink, L. B. F. A Comparison of CO Oxidation by Hydroxyl and Atomic Oxygen from Water on Low-Coordinated Au Atoms. *ACS Catal.* 7051–7058 (2016). doi:10.1021/acscatal.6b01720
159. Min, B. K., Alemozafar, A. R., Pinnaduwage, D., Deng, X. & Friend, C. M. Efficient CO Oxidation at Low Temperature on Au(111). *J. Phys. Chem. B* **110,** 19833–19838 (2006).
160. Zhang, W., Li, Z., Luo, Y. & Yang, J. Density functional study on mechanism of CO oxidation with activated water on O/Au (111) surface. *Chin. Sci. Bull.* **54,** 1973–1977 (2009).
161. Moskaleva, L. V., Zielasek, V., Klüner, T., Neyman, K. M. & Bäumer, M. CO oxidation by co-adsorbed atomic O on the Au(321) surface with Ag impurities: A mechanistic study from first-principles calculations. *Chem. Phys. Lett.* **525,** 87–91 (2012).
162. Bäumer, M. Private Communication.

Appendix A

I. Calculation of the oxygen flux through the tube based on the background pressure:

As described in **Section 3.2.1**, the scattering chamber has a 500 L turbomolecular pump mounted. Considering a pumping speed of 500 L s^{-1} and noticing that 1 standard cubic centimetre per minute (sscm) is equal to a leaking rate of 0.016 mbar L s^{-1}, one can calculate the gas flow through the oxygen cracker based on the desired background pressure in this setup using the **Equation A1**.

$$gas\ flow = \frac{P_{background}[mbar] \times S_{pumping\ speed}[L\ s^{-1}]}{0.016\ [mbar\ L\ s^{-1}/sccm]} \qquad \mathbf{1}$$

For the oxygen pressures of $3.2 \cdot 10^{-8}$ mbar ($p_{background} = 1 \cdot 10^{-8}$ mbar) and $1.4 \cdot 10^{-7}$ mbar ($p_{background} = 5 \cdot 10^{-8}$ mbar) used in this thesis the corresponding gas flows are 0.0003 sccm and 0.0016 sccm, respectively. According to the data sheet provided by the manufacturer, at low gas flow regime the grade of dissociation demonstrated a linear dependency of the gas flow through the cracking tube for constant operational temperatures[75,76]. To this end, one can estimate the total flux ***f*** of O-atoms for the two oxygen gas flow calculated with 13% of cracking probability. For the low oxygen pressure ($3.2 \cdot 10^{-8}$ mbar), the total oxygen flux is estimated to be about $1.4 \cdot 10^{12}$ atoms$\cdot cm^{-2} s^{-1}$, and for high oxygen pressure ($1.4 \cdot 10^{-7}$ mbar) is estimated to be approximately $7.3 \cdot 10^{12}$ atoms$\cdot cm^{-2} s^{-1}$.

Appendix B

I. Chemicals

All experiments were performed in an ultra-high vacuum molecular beam and IR coupled apparatus. Argon (Air Liquide, 99.999%) was used for sample sputtering. O_2 (Air Liquide, 99.995%) was introduced into the thermal oxygen cracker to produce O-atoms. For CO IRAS and reactive experiments, ^{13}CO (Euriso-top, 99%) beam was used. Water beam ($D_2{}^{18}O$ – Sigma Aldrich, > 95 %) was purified prior to each experiment by repeated freeze-pump-thaw cycles. N_2 (Air Liquide, 99.999%) was used for the gas bearings of the infrared interferometer. In order to avoid contamination, the gas lines were flushed thoroughly prior to each experiment.

II. Pulsed Molecular Beam Experiments

The pulsed molecular beam experiments were performed according to the sketch shown in **Figure B1**. Sequential steps for introducing a gas into the scattering chamber were considered in order to define the background level during the reactive experiments. Initially all the three beams were valve and shutter closed (**1**). Thereafter, the oxygen beam was introduced first by opening the valve and the shutter was remained closed (**2**). Before the admittance of the ^{13}CO and $D_2{}^{18}O$ beams into the scattering chamber, the oxygen pressure was adjusted. In the sequence, ^{13}CO was introduced and shortly thereafter water. The shutter of the ^{13}CO and $D_2{}^{18}O$ beam were opened simultaneously (**3**).

During reactive experiments, the sample was continuously exposed with the CO and water beam at variable flux, while the oxygen beam source was modulated with different pulse width accordingly to the desired experiment. The infrared was measured ON oxygen pulse and OFF oxygen pulse. Moreover, beam modulation, flux intensities, and sample temperature are fully computer controlled in order to ensure the reproducibility between the experiments.

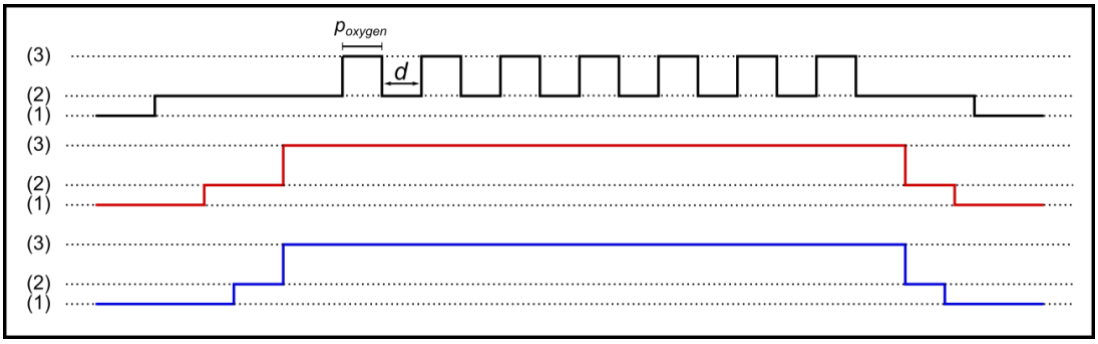

***Figure B1**: Sketch of a molecular beam pulse experiment. Three beams are represented: $D_2{}^{18}O$ beam (blue), ^{13}CO beam (red), and ^{16}O beam (black). Sequential stages valve and shutter closed (1), valve open /shutter closed (2), and valve and shutter open (3). Both pulse width (p_{oxygen}) and the delay time (d) of the oxygen pulses are in second and defined for each experiment.*

Abbreviation List

AES	Auger Electron Spectroscopy
AOB	Atomic Oxygen Beam
CMA	Cylindrical Mirror Analyzer
DFT	Density Functional Theory
EM	Electron Multipliers
ER	Eley-Riedel
GCA	Glass Capillary Array
HeNe	Helium-neon Laser
IRAS	Infrared Reflection Absorption Spectroscopy
L	Langmuir
LH	Langmuir-Hinshelwood
LEED	Low Energy Electron Diffraction
MB	Molecular Beam
MCP	Micro Channel Plate
MCT	Mercury Cadmium Telluride
ML	Monolayer
MS	Mass Spectrometry
NP	Nanoparticle
Np-Au	Nanoporous–Gold
STM	Scanning Tunnelling Microscopy
TEM	Transmission Electron Microscopy
TMP	Turbomolecular Pump
TPD	Temperature Programmed Desorption
UHV	Ultrahigh Vacuum
XPS	X-ray Photoelectron Spectroscopy

CV

For reasons of data protection, the curriculum vitae is not published in the electronic version